Cuentos de las Estrellas: Understanding the Properties and Impacts of Stellar Flares Across Time and Wavelength

Guadalupe Tovar Mendoza

A dissertation
submitted in partial fulfillment of the
requirements for the degree of

Doctor of Philosophy

University of Washington

2024

Reading Committee:
James R. A. Davenport, Chair
Eric Agol
Allison A. Youngblood

Program Authorized to Offer Degree:
Astronomy

University of Washington

Abstract

Cuentos de las Estrellas: Understanding the Properties and Impacts of Stellar Flares Across Time and Wavelength

Guadalupe Tovar Mendoza

Chair of the Supervisory Committee:
Professor James R. A. Davenport
Astronomy

The era of new space and ground based telescopes is providing us with more detailed exoplanet observations and advancing the search for life beyond our own solar system. These observations are providing opportunities to both study the makeup of extrasolar worlds and also search for signs of habitability. However, stellar variability remains a limiting factor for planet detection and characterization. We see stellar contamination present in almost all exoplanet observations, especially around active M-type stars. Although it is seen as a source of contamination for most observations, stellar activity provides us with key insights into the larger star-planet environment. In order to understand and model the detailed properties of exoplanets we must understand the host stellar environment. Specifically, the signals generated by stellar magnetic activity need to be properly characterized and understood in order to gain a clear picture of the astrobiological implications stellar activity has on extrasolar worlds. To address these challenges, I have focused my thesis work on developing tools and leading studies that help us gain a better understanding of the properties and impacts of stellar flares across time and wavelength regimes. By leveraging existing datasets such as *Spitzer*, *Kepler*, TESS, and *Gaia* I have studied how stellar activity impacts our search for life on other worlds beyond our solar system.

In the first part of this thesis, I generate new tools for the community to use to model and

understand photometric stellar activity in detail. Specifically, I use *Kepler* data to study the morphology or shape of stellar flares. I derive a continuous and analytical model to describe the shape of flare events in photometric observations. I test the flare template on datasets of various cadences and wavelengths and find the model is versatile enough to fit flare events in all of the tested cases. Furthermore, this flare template has already been used by other teams to model flares in both Kepler and TESS data (Barclay et al., 2023).

In the second part of this dissertation, I study the energetics of flare events at infrared wavelengths. Even though flare emission peaks at near-ultraviolet and blue optical wavelengths, they emit energy across the entire electromagnetic spectrum. Flares in the infrared are only just beginning to be studied in detail as JWST is revealing they are a source of contamination for exoplanet studies. We use archival Spitzer observations of flares to constrain flare temperatures and understand their implications on exoplanet atmospheres. I turn to the active, planet hosting star, TRAPPIST-1, to study how flare temperatures vary at infrared observations and in turn affect the exoplanets in orbit around the star. I also compare our results to the latest JWST observations of TRAPPIST-1.

The third part of this thesis looks to the future to understand what upcoming flagship missions like the Nancy Grace Roman Space Telescope will provide for flare science. The final part of this thesis work explores how flare energetics change as a function of stellar mass and how the results impact the exoplanets around those stars. The resulting code and models developed for this thesis will be made open source to serve as tools for the greater astronomy and astrobiology communities.

TABLE OF CONTENTS

Page

List of Figures iv

List of Tables xi

Chapter 1: Introduction 1
1.1 Lessons from the Sun 2
1.1.1 Dynamo Theory 4
1.2 Magnetic Activity on Low Mass Stars 5
1.2.1 Flares 7
1.2.2 Other Forms of Activity 7
1.3 Astrobiology and Habitability 11
1.4 Multi-Wavelength Datasets 12
1.4.1 Kepler/K2 12
1.4.2 Transiting Exoplanet Survey Satellite 14
1.4.3 Spitzer Space Telescope 14
1.4.4 Gaia 15
1.4.5 Nancy Grace Roman Space Telescope 15
1.5 Outline of Thesis 16

Chapter 2: Llamaradas Estelares: Modeling the Morphology of White-Light Flares 18
2.1 Summary 18
2.2 Introduction 19
2.3 Defining the Flare Sample 23
2.4 Modeling Starspot Variability 24
2.4.1 Gaussian Process Regression 24
2.5 Continuous Flare Model 26
2.5.1 Comparing Flare Model Parameterizations 28

2.6 Stacking the Flares . . . 29
2.6.1 Improving the Stacking Procedure . . . 31
2.7 Fitting the New Model . . . 33
2.7.1 Model Comparison . . . 36
2.7.2 Updated Flare Properties . . . 38
2.8 Applications . . . 41
2.8.1 GJ 1243 *TESS* Data . . . 41
2.8.2 Flares at Different Cadences . . . 44
2.9 Discussion and Conclusions . . . 45
2.10 Acknowledgements . . . 48
2.11 De Colores: Kepler + TESS . . . 49

Chapter 3: Revisiting the Stellar Flares of TRAPPIST-1 with the Spitzer Space Telescope . . . 52
3.1 Summary . . . 52
3.2 Introduction . . . 52
3.3 Methods . . . 55
3.3.1 Detrending the Spitzer data . . . 55
3.3.2 Identifying Flares . . . 59
3.3.3 Flare Properties . . . 60
3.3.4 Flare Frequency Distributions . . . 61
3.3.5 K2 Data . . . 64
3.3.6 Luminosity Calibrations . . . 64
3.4 Flare Temperature Analysis . . . 67
3.4.1 Chi Squared Analysis . . . 68
3.5 Results & Discussion . . . 70
3.5.1 Infrared Flare Temperatures . . . 70
3.5.2 Comparison to JWST . . . 71
3.5.3 Future Directions . . . 72

Chapter 4: Chispas de Luz: Stellar Flare Yields with the Nancy Grace Roman Space Telescope . . . 73
4.1 Summary . . . 73
4.2 Introduction . . . 74

4.3 Methods 76
4.3.1 Assumed Stellar Population 76
4.3.2 Generating Synthetic Roman Light Curves 78
4.3.3 Flare Detection 85
4.4 Results 88
4.4.1 Flare Yields 88
4.4.2 Optimal Read-Out Schematic 90
4.5 Discussion 90
4.6 Acknowledgments 93

Chapter 5: Conclusions 94
5.1 Summary 94
5.2 Future Work 95
5.2.1 Understanding Flare Energetics with Gaia 95
5.2.2 Probing Infrared Flares with JWST 101
5.2.3 Future Observatories 104
5.2.4 Space-Based Observatories 105

Appendix A: Vita 129

LIST OF FIGURES

Figure Number Page

1.1 Large energy solar flare eruption (X8 class) that occurred on the Sun on Sept 10, 2017, right as I was starting graduate school. The left and right images show the same flare at two different extreme ultraviolet wavelengths (193 and 171 Angstroms, respectively). The loops we see above the surface trace magnetic field lines being reorganized. Credit: Solar Dynamics Observatory, NASA 3

1.2 Illustration of a flare, modified from (Martens, 1989; Bazilevskaya, 2017). In black are the magnetic field lines that create the flare loop. The multi-colored arrows indicate the various emission forms that are detected when a flare occurs. The black arrow at the top indicates the shock front and potential CME that flares can often trigger. 8

1.3 Transiting exoplanets and planet candidates that have been discovered by *Kepler* (black), K2 (blue), and TESS (orange) as of March 2024. Shown on the x-axis is the orbital period in days, as a function of Earth radii. 13

2.1 Two days of GJ 1243 *Kepler* 1-minute observations are shown in blue. The identified classical flares (red), the GP mean (orange) and variance are all overlayed. **Left**: We identified three classical flares during this window. **Right**: We identified two classical flares that were used to derive the flare model. Note there are two complex flares (grey), one in each panel, but these were not used to construct the flare template. To accurately model the underlying starspot modulations we masked out all flares which allowed the GP to model the starspot variability without being skewed by frequent flaring events. Therefore, we expect the GP to have the highest variance in areas where flares are occurring. 22

2.2 Comparison of the piece-wise flare template from D14 (black curve) and the initial version of our continuous flare model (blue curve). For reference, we show the full 885 flares sample stacked using the D14 procedure (grey points), which produces significant scatter in flux from forcing each flare to a peak of exactly 1. We also note the aliasing from improperly estimating the FWHM for short duration events (vertical bands) from the 1-minute cadence *Kepler* data. 30

2.3 **Top:** The updated continuous analytical model (blue) overlaid onto the final vetted sample of 414 classical flares from the DR25 *Kepler* data release. The solid black points are the binned median with the respective standard deviation of the points inside of each bin. The flares are overlaid using a new stacking procedure that is less sensitive to sampling effects and scales each flare to a relative time and amplitude. **Bottom:** The residuals of the model (grey) and the binned residuals of the model in black which are mostly uniform and flat. The structure in the decay phase of the flares is caused by a combination of uncertainties in the stop times of flares and the starspot detrending. The combination of using a GP to model the starspots + continuous model + vetted flare sample + new stacking procedure has produced a more robust flare template. 32

2.4 The results from the MCMC analysis showing the posterior probability distributions of each of the model parameters from Equation 2.4. This figure was made using `corner.py` (Foreman-Mackey, 2016). 34

2.5 Example flare from the vetted set of *Kepler* classical flares with the analytic model overlayed. We show the final flare model can be parameterized using the following three scaling parameters: amplitude, FWHM, also known as $t_{1/2}$ in Kowalski et al. (2013), and center time (which is similar to tpeak in D14). 36

2.6 Comparison of the D14 and updated analytic flare templates overlayed onto the new stacked flares data set (grey points). The scatter in the data is from nearby, low energy flares. In black, is the piece-wise model from Davenport et al. (2014) and in blue one is the new analytic template that uses the convolution of a Gaussian and a double exponential. The updated analytic model is continuous and more accurately describes the peak of the flare events. . . 37

2.7 **Top:** The top two panels follow the correlation we expect. Flares with higher energies occur over longer timescales and also have higher amplitudes. Meanwhile, lower energy flares occur over shorter timescales and have shorter amplitudes. **Bottom:** There is significant scatter among the FWHM plots which shows that there are flares that are both tall and narrow as well as short and wide. The combination of FWHM and flare amplitudes allow us to characterize the flare profile. The orange lines represent the binned medians for each of the datasets. The color gradient shows flares with different durations (yellow = longer flares and purple = shorter flares). 39

2.8 Here we show the product of FWHM and amplitude versus the equivalent duration of flare events, both in units of seconds. The data points are color coded by time durations in units of minutes, where lighter colors correspond to longer flare events and darker colors correspond to shorter flare events. The tight correlation between these parameters indicates taht the combination of flare amplitude and FWHM are sufficient to characterize the flare event profile with our model. 40

2.9 We test the GP modeling, stacking procedure and flare identification on *TESS* data. **Top:** Overlay of the updated flare template (purple) onto 25 classical flares from sectors 14 and 15 of GJ 1243 *TESS* data (grey) that are all scaled to a relative time and amplitude. The black points are the binned median of the data with the respective standard deviation of the points inside of each bin. **Bottom:** The residuals of the model (grey) and the binned median of the residuals (orange). The scatter is fairly uniform and the residuals are low suggesting the data is well fit by the model. The flare template can be used to model flares from different datasets and observations at different cadences. 42

2.10 We use the new analytic flare template to model one of the flare events occurring on the M3.5 star (TIC 197829751) that was observed by *TESS*. We compare how our model works at different time resolutions. On the far **Left:** we have 20 second data, in the **Center:** we have 2 minute data, and on the **Right:** is the 10 minute data for the same target. Note the increased amount of structure that is revealed in the 20-second flare data vs the 10-minute data. The higher resolution highlights some secondary features in the cooling phase of this particular flare that are not as apparent in the 2-min or 10-min data, hence the different model fits. A table of the best fit values for each cadence mode can be found in Table 2.3. 43

2.11 Distribution of flare energy as a function of flare amplitude for the sample of GJ 1243 flares. In orange we show a total of 183 flares identified with TESS Sectors 14 and 15, and in blue are the 6107 flares identified with 11 months of *Kepler* data. 50

2.12 Flux-calibrated spectrum for GJ 1243 (thick black line) from (Reid et al., 1995), with the scaled NUV–NIR M4 template (thin gray line) from (Davenport et al., 2012), which is used to calculate the quiescent luminosity for GJ 1243 in the Kepler (blue line) and TESS (red line) bandpasses. Figure from (Davenport et al., 2020). © AAS. Reproduced with permission. 51

3.1 Raw Spitzer light curve of over 1000 hours ($\approx$ 40 days) of TRAPPIST-1 observations from Feb. 2017 - Oct 2019. Photometric measurements were taken using both the 3.6 μm and 4.5 μm bandpasses. These data were collected as part of the Spitzer Exploration Science program Red Worlds (ID 13067), DDT program 12126, DDT program 13175, and DDT program 14223 (Gillon et al., 2017a; Delrez et al., 2018; Ducrot et al., 2020; Agol et al., 2020). The data is available on the Spitzer Heritage Archive database. 56

3.2 A zoom in of two days of photometric observations of TRAPPIST-1 where we can see both an exoplanet transit and a flare occurring. The raw data is in blue. The detrended data is in orange. In green we show the transit model. By detrending the raw data we are able to improve the point-to-point scatter by a factor of 1.4. 58

3.3 A zoom in of the three largest T-1 flare events that were identified in the Spitzer data. From left to right the flares have durations of 158, 64, and 82 minutes. The first two flares were observed with the 4.5 μm bandpass, and the rightmost flare was observed at 3.6 μm. We note starspot modulations have not been subtracted, we only do spatial detrending. 60

3.4 Filter curves for each of the datasets considered in this work. The Kepler (blue) bandpass covers wavelength ranges from 4000-8650 angstroms, and TESS (orange) covers 6000-10000 Angstroms. Meanwhile, the Spitzer Infrared Array Camera (IRAC) (Fazio et al., 2004) provides simultaneous 5.2' $\times$ 5.2' images at 36000, 45000, 58000, and 80000 Angstroms, for this work we only consider the first two channels. In gray is the Mega-MUSCLES T-1 spectrum from (Wilson et al., 2021). 63

3.5 Flare Frequency Distribution (FFD) of T-1 flares showing the cumulative number of flares observed per day as a function of their log equivalent durations. In orange are the 15 flares observed by Spitzer and in blue are the 35 flares that were observed by K2 (Davenport, 2017). The offset is due to the differences in bandpasses with K2 observing at optical wavelengths and Spitzer observing in the infrared. 65

3.6 A reconstructed distance-calibrated SED of TRAPPIST-1 from (Gonzales et al., 2019). We include photometry from K2 and TESS. The solid lines represent the flux-conserved interpolation over the various bandpass ranges. 66

3.7 Flare Frequency Distributions (FFD) of T-1 flares from K2 and Spitzer, converted to TESS flare energies assuming a fixed blackbody flare temperature. We treat the two Spitzer bandpasses independently. Each panel assumes a different blackbody temperature for the flares. JWST T-1 flares from Howard et al. (2023) are shown for qualitative comparison, but were not used in our analysis (purple points). Straight lines indicate the power law fits assuming a slope of $\alpha = -1$. The middle panel highlights the scenario where the FFDs from K2 and the two Spitzer bands most closely align. In other words, a mean flare temperature of $\approx$ 5480 K produces a consistent flare rate across all bandpasses in our sample. 67

3.8 χ^2 results after performing a grid search in steps of 1°K in temperature. We find the minimum value of $\chi^2 = 3.68$ happens at a temperature of $T_{eff} = 5480$ K $\pm$ 83 K. 69

4.1 Apparent magnitude versus temperature of the simulated G (blue), K (orange), and M (red) stars in our sample. 77

4.2 Rotation amplitude versus rotation period of the stars we simulated. The color bar shows the age distribution of stars. 80

4.3 Simulated Roman light curves of a G, K, and M star with corresponding noise and crowding properties. The flares that are injected into each light curve were drawn from an age based flare frequency distribution (Davenport et al., 2019). 83

4.4 Candidate readout strategies introduced in Casertano (2022). Each individual point represents one read frame, and each color represents one resultant frame (e.g., R1, R2, etc.). Each resultant frame will consist of the average of one or more read frames. 84

4.5 Flare yields for G, K, and M star simulations and corresponding flare properties for a logarithmic read out scenario. The first row shows histograms of the total injected flares by log flare energy [erg] for each stellar type. The second row shows the log amplitude of the flares versus log flare energy. The final row is the FWHM versus log flare energy. Across all panels the darker shaded regions are the false positives that were injected, the black dots are the recovered false positives. In orange are the flares recovered in the full exposure data, and in blue are the flares recovered in the ramp data. 87

4.6 Flare yields for G, K, and M star simulations and corresponding flare properties for a read-out scenario where all read frames are preserved. The first row shows histograms of the total injected flares by log flare energy [erg] for each stellar type. The second row shows the log amplitude of the flares versus log flare energy. The final row is the FWHM versus log flare energy. Across all panels the darker shaded regions are the false positives that were injected, the black dots are the recovered false positives. In orange are the flares recovered in the full exposure data, and in blue are the flares recovered in the ramp data. 89

4.7 Simulated stellar luminosities [L_{Sun}] versus the log flare energies [erg] (black). The orange data are flares that were recovered in the full exposure light curve and in blue are the flares recovered in the ramp data. On the top are the results for the logarithmic read-out schematic and on the bottom are the results for the read-out schematic that preserves all the read frames. 91

5.1 Apparent Gaia G-band magnitudes and effective temperatures for the 228 stars pulled from the Gaia alerts on April 2024 with following cuts: Temperature $\leq$ 3850; Radii $\leq$0.6 ; Magnitude (M_G) $\leq$ 17. 96

5.2 Top: Example Gaia alert of an active M star showing a 2 magnitude flare. Bottom: Simultaneous low resolution bp/rp spectra of the same target at the time of the flare event. 98

5.3 Raw epochal bp/rp spectra for 137 epochs for a flaring M5 dwarf that generated the Gaia alert Gaia22bam (TIC 354134293). Each epoch is colored by the published mean G magnitude. The blue channel is pixels 0–59, while the red channel is pixels 60–119. Note the pixel direction for the blue channel has been flipped relative to the observed Gaia data, so that it is in wavelength order. During the flare event (purple curve) we see an increase of two orders of magnitude in the blue channel, and a slight increase in the red channel, consistent with our expected behavior for a hot flare on this cool star. 99

5.4 Example of a response function derived for the blue and red gaia filters for the flaring M5 star (gaia22bam). We note the response functions will be significantly improved when the higher-resolution mean *Gaia* spectra becomes available in a couple of years. 102

5.5 Top: G band light curve of a *Gaia* alert of an active M star. The long base line combined with the steady brightening is a sign of spot modulations. Bottom: Corresponding TESS 30 min data (sector 11) of the same target, confirming the rotational spot modulations. 103

LIST OF TABLES

Table Number Page

2.1 Best fit coefficients for Equation 2.4, and their respective uncertainties from the Markov Chain Monte-Carlo analysis, which define the flare shape as shown in Figure 2.3. 33

2.2 Classical Flare Properties 38

2.3 TIC 197829751 Flare Properties 46

3.1 TRAPPIST-1 Spitzer Flare Properties 62

4.1 Flare Injection & Recovery Results 81

4.2 Readout Schematics Considered. 86

ACKNOWLEDGMENTS

"Most success stories are gratitude stories" - Dr. Brandon Ogbunu (SACNAS 2020)

The work presented in this dissertation represents the culmination of seven years of graduate study at the University of Washington that would not have been possible without the support and guidance of SO many people. I am incredibly grateful for all the people that helped guide, support, and encourage me throughout my academic journey. While a few sentences do not begin to fully embody my gratitude I will do my best to give flowers to the people who helped me along my academic journey.

To my advisor James R. A. Davenport, the words thank you don't quite express the extent of my gratitude for all that you have done to support me over the years but we will start there. Thank you for taking a chance on working together. Your empathy, sincerity, and guidance made all of the difference at a point in my grad school journey where I was heavily considering leaving the program. Thank you for believing in me, for challenging me to do the hard things, and helping shape the scientist I am today. I am a better writer, coder, and researcher thanks to your feedback and many lessons. Most of all thank you for seeing my full humanity. Life doesn't just stop when we pursue PhDs, and you have been nothing but supportive and empathetic during all the rocky points in my grad school career. Thank you also for your humility and active listening. In a field so eager to train the next generation of science professors it was refreshing to have someone ask and support my career dreams even if they were different from yours. Furthermore, thank you for encouraging me to form new collaborations outside of our team and to look for mentors beyond UW. Thank you for all the conferences you supported me attending, these were important places where I was able to network and find mentors. I am forever grateful that we got to work together,

and I will take with me all the good science and life lessons with hope of sharing them with my future students. Mil gracias, Jim. I could not have finished this PhD without you.

Thank you to all of my thesis committee members. Eric Agol, thank you for believing in me and being a mentor on my team from my undergrad years and all through my grad school career. Your writing feedback, tough science questions, guidance, and support have been instrumental to my success in graduate school. Allison Youngblood, thank you for being a great collaborator and mentor. I have learned a lot both scientifically and in terms of what a mentor role looks like from you. I appreciate you taking me under your wing the last couple of years of graduate school. Thank you for all of your feedback and guidance during my research rotation, on the Roman project, and most recently with applying to jobs. William (Bill) Mahoney, thank you for being the GSR on my committee and for checking in throughout my grad school journey to see how I was doing. Jodi Young, thank you for being such a kind and welcoming face within UW astrobiology. I have really appreciated your support over the years and I am so happy to have you as my AB rep on my committee. Thank you all for the time and energy you have invested in me and for pushing me to be a better scientist and scholar.

Thank you to my graduate mentoring committee: Emily Levesque and Benjamin Montet. Your support and guidance over the years is greatly appreciated. Thank you for believing in me and helping shape the scientist I am today. Thank you also to Suzanne Hawley. I'm not sure you know the impact you have had on my career but thank you for being the person you are. Thank you for having my back and standing in my corner during a critical time in my graduate career, I am so grateful for your support and mentorship.

To my collaborators: Laura Vega, Robby Wilson, Teresa Monsue, Tom Barclay, Elisa Quintana, Lynnae Quick, thank you for highlighting the joys of working together on a team. I have learned so much from all of you and have greatly enjoyed working with each and everyone of you. Together we are greater than the sum of our own individual parts.

To the graduate students at UW I've gotten the pleasure to meet over the years, especially my GCAP peers, thank you for your friendship, allyship, support, and encouragement. It has been a joy to be in community with you all. I am especially grateful for our dissertation writing accountability group: Brianna, Myles, Debby, Miles, and Dino thank you for your company. You all made writing this dissertation more bearable. Thank you also to all of the volunteers that make up e-STEAM. You all remind me of what it looks like to pay it forward, to leverage our privileges, and to work together as a team for a greater cause. It has been a joy and honor to volunteer and make a difference alongside you all.

To the mentors who have had my back and have been there during some of my lowest and highest points in graduate school: Dr. Carolyn Jackson, Dr. Chanda Prescod-Weinstein, Jaye Sablan, and Dr. Lia Medeiros, thank you for seeing greatness in me and reminding me of my potential especially in times when I did not see or believe it.

Thank you to the amazing people within the Office of Minorities Affairs and Diversity and GSEE for all that you have done to support my journey at UW. A special shout out to Dr. Todd Sperry, Norma Ramirez, and Luz Iñiguez, thank you for having my back ever since stepping foot on this campus as an undergrad. You truly make UW a better place, I am eternally grateful to you all.

To the students I have had the privilege of mentoring and advising over the course of my graduate career, thank you for the positive impact you have had on me. I am so proud of each and every one of you. It has been an honor to learn alongside you and share in community. I know you all will go off to do amazing things, and I am so grateful that we got to cross paths.

To all of my friends (you know who you are), thank you for supporting me and being a part of my journey. You've kept me grounded and have motivated me to continue pursuing my dreams.

Gracias infinitamente a mi familia: mami, papi, Luz, mamá Tere, mamá Icha, tías, y

tíos, por todo su apoyo y todas sus oraciones. Sin ustedes esto no hubiera sido posible. Por ustedes, para ustedes, y gracias a ustedes. En especial gracias mami y papi que sacrificaron todo para darme un mundo mejor, sin ustedes yo no estaría aquí. Gracias por quererme incondicionalmente, por enseñarme a luchar por mis sueños, por levantarme las veces que caí, y por celebrar todos mis logros. Ustedes son mi motivación e inspiración más grande, ya es hora de cosechar nuestros logros.

To my fiance, Andrell, thank you for being the wonderful human being that you are. You have been a constant source of joy, inspiration, comfort, encouragement, and support. I am eternally grateful for your partnership and support through graduate school. I am so blessed to have you in my life and I look forward to our future together.

La vida sigue. Gracias José A. Flores Velázquez, Dr. Gabriel E. Gallardo, Papá Chuy, Angel Mendoza Alcocer, Amalia Del Pozo, y Papá Ciro. The ones who transitioned to the ancestral realm during my time as a graduate student and are not here to physically see this final body of work but had a tremendous impact on both my academic and personal journey. Gracias por todo su apoyo desde arriba.

Little Lupita never knew or imagined earning a PhD is astronomy and astrobiology would be a possibility. Thank you all for believing in this first generation Mexicana who dared to reach for the stars.

DEDICATION

para mis padres,

Blanca Tovar Mendoza y Jaime Tovar Díaz.

¡sí se pudo!

Chapter 1

INTRODUCTION

The year I was born, the first planet orbiting a Sun-like star was discovered, 51 Pegasi b (Mayor, 1995). Since then, five thousand more exoplanets — planets orbiting stars other than our Sun — have been discovered. The last three decades of both space-based and ground observations have transformed our understanding of exoplanets and their host stars. Current and future observations are taking the next steps to characterize the environments of these worlds, and assessing whether the conditions are suitable for life. As we progress through the era of exoplanet characterization we get closer and closer to answering the age old question of: "Are we alone in the universe?".

This thesis work lays a path into the era of stellar and planetary characterization by deepening our understanding of the relationship between stars and their planets. Mainly, I will focus on the impacts and properties of the eruptive events that happen on the surfaces of stars — flares — and how they vary across time and wavelength. In particular, this work will focus on flare properties and how these energetic events influence star-planet environments. My thesis work will (1) generate new tools for the community to use to model and understand photometric stellar activity in detail, (2) explore the prospects of using multi-wavelength observations of flares to constrain flare temperatures and understand their implications on exoplanet atmospheres, and (3) explore how future observatories will enable flare demographic studies. The resulting code and models developed for this thesis have been made open source to serve as tools for the greater astronomy and astrobiology communities.

In this first chapter, I provide a broad introduction of the the concepts and observations that will be discussed throughout the entirety of this thesis. I begin with an overview of lessons learned from our own Sun about stellar magnetic activity. I then transition to

explain stellar magnetic activity on low mass stars and its manifestations. Then I consider the star-planet relationship and describe the implications stellar activity has on the exoplanet habitability. Finally, I give a brief overview of the datasets I use throughout my dissertation work, and give an outline for the remainder of the thesis.

1.1 Lessons from the Sun

For centuries, astronomers have been studying our own host star, the Sun, in efforts to understand our place in the universe and the relationship between Earth and the Sun. In 1613, Galileo noted the Sun had dark spots (Galilei et al., 1613), which became a modern indication that our Sun was a complex and changing body due to the presence of magnetic fields. Since then, astrophysicists have learned numerous valuable lessons from our Sun, which have shaped our understanding of stars, planetary systems, and our chemical makeup. For this thesis work, I will highlight the key lessons in solar activity that we have learned over time.

On the Sun, we see a wide range of magnetic activity phenomena occurring on the surface. Stellar magnetic activity includes coronal mass ejections (CMEs), starspots, and stellar flares. We also observe a 22 year activity cycle, that is characterized by the size and number of sunspots and flares (Hathaway, 2015). During cycle maximums is when we observe the most magnetic activity occurring on the surface of the star (e.g. more spots and flares). Each of these phenomena produce unique photometric and spectroscopic signatures (Kowalski et al., 2013). For instance, in Figure 1.1 we see an example of a flare occurring on the limb of our Sun that was observed with the Solar Dynamics Observatory. Stellar flares are explosive events that occur in the Sun's atmosphere, which are caused by the reorganization of magnetic field lines, magnetic reconnection (Benz, 2008). Solar flares can have durations lasting from minutes to hours. Studies have shown the energy release of these solar flare events can vary up to 10 orders of magnitude from the smallest "nano-flares" (10^{24}erg) all the way up to the most energetic "super-flares" ($> 10^{32}$erg) (Aschwanden, 2002; Shibata, 2002). Flares can also trigger larger particle events (coronal mass ejections), which if directed

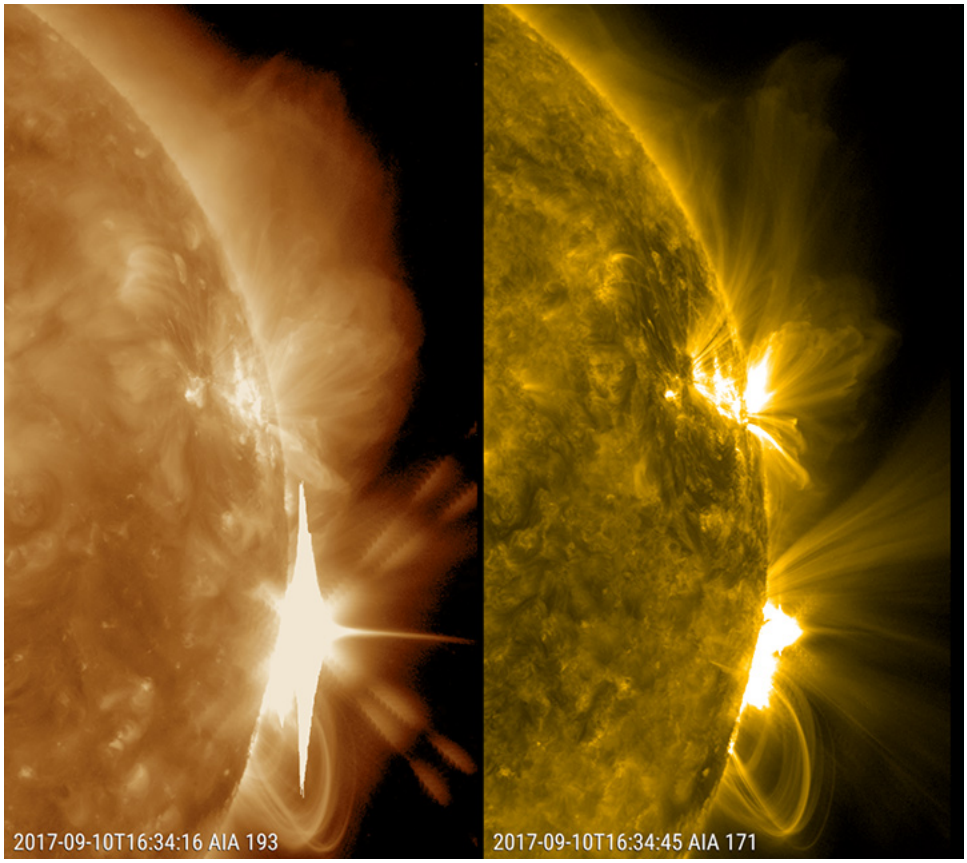

Figure 1.1 Large energy solar flare eruption (X8 class) that occurred on the Sun on Sept 10, 2017, right as I was starting graduate school. The left and right images show the same flare at two different extreme ultraviolet wavelengths (193 and 171 Angstroms, respectively). The loops we see above the surface trace magnetic field lines being reorganized. Credit: Solar Dynamics Observatory, NASA

at Earth can interact with our atmosphere and produce aurora (Webb & Howard, 2012; Luger et al., 2017a; Alvarado-Gómez et al., 2022). By understanding the Sun, we have a benchmark to reference when we study other stars.

1.1.1 Dynamo Theory

Stellar magnetic activity on the surface is driven by the interior magnetic dynamo of a star (Brun & Browning, 2017). Solar dynamo theory explains the generation and maintenance of the Sun's magnetic field and it was first pioneered by (Parker, 1955). According to this theory, the solar magnetic field is produced by the motion of electrically conducting fluids within the Sun's interior, primarily the convective motion of plasma in the convection zone (Durney B, 1993). Furthermore, the differential rotation of the Sun — where different latitudes rotate at different speeds — plays a crucial role in amplifying and organizing the magnetic field through a process called the $\alpha\Omega$ dynamo mechanism. In this mechanism, the twisting and shearing of magnetic field lines by the differential rotation generate electric currents, which in turn generate additional magnetic fields (Charbonneau, 2014). The α effect arises from the interaction between turbulent motions (convection) and the rotation of the fluid (differential rotation) in a conducting medium like plasma. Within the convective cells, turbulent motions generate small-scale vortices and eddies. Due to the rotation of the Sun, these turbulent motions exhibit a preferred direction (often helical or spiral) imposed by the Coriolis force (resulting from the rotation of the Sun). Thus, the α effect describes how these helical turbulent motions can create a small-scale magnetic field. Meanwhile, the Ω effect describes how differential rotation in the Sun acts to stretch, amplify, and organize the magnetic field generated by turbulent motions (α effect) within the Sun's interior. Differential rotation occurs radially throughout the convective zone to the surface and also at the tachocline (boundary layer between the radiative core and convective outer envelope). The complex interplay between fluid motion, magnetic fields, and turbulence within the Sun's interior gives rise to the cyclical behavior of the solar magnetic field, including the 22-year solar activity cycle characterized by the emergence of sunspots (Babcock, 1961), solar flares, and coronal

mass ejections (Hathaway, 2015). Solar dynamo theory provides a comprehensive framework for understanding the Sun's magnetic activity and its influence on solar phenomena and space weather. It also sets the stage for our understanding of dynamos on stars beyond our Sun.

1.2 Magnetic Activity on Low Mass Stars

Magnetic fields are prevalent on low-mass stars. Here I provide an overview of stellar magnetic activity on low mass stars. I define "low-mass" as stars that are less than or equal to the mass of our Sun (spectral types GKM). As described in Section 1.1.1, surface magnetic activity is fueled by the stellar dynamo. G, K, and early M stars all display a similar internal structure to that of our Sun, with a core, radiative zone, tachocline, and outer convective envelope. However, as we get to later spectral types (M3-M4), the radial extent of the convective envelope begins to extend fully from the surface to the stellar core (Reiners & Basri, 2007). Observationally, the "fully convenctive" limit is not well defined and future work is needed to study the detailed internal structure of these fully convective stars.

Stellar magnetic activity is also a function of age and rotation. Specifically, rotation plays a key role in dynamo models, where faster rotation is linked to greater magnetic field strengths as described in Section 1.1.1. Furthermore, as stars age, they lose angular momentum (Soderblom, 2010). The Rossby number (Ro) is a dimensionless number that has been used to describe the ratio of a star's rotation period to its convective turnover time (the characteristic time for convective cells to overturn in the star's interior) (Wright et al., 2011). Mathematically,

$$Ro = \frac{P_{rot}}{\tau_{conv}}, \tag{1.1}$$

where P_{rot} is the rotation period and τ_{conv} is the convective turnover time. A low Rossby number indicates the rotation period is shorter than the convection turnover time. This leads to higher chromospheric activity, which is often detected in young, rapidly rotating stars (Feinstein et al., 2024). Meanwhile, a high Rossby number tells us the rotation period is greater than or equal to τ_{conv}, indicating less chromospheric activity. This regime is typical

for older, slowly rotating stars like the Sun (Brun & Browning, 2017). Additionally, it has been shown that activity levels, specifically flare rates, decrease with the increasing rotation period of the star (Notsu et al., 2013; Davenport, 2016), thus older stars will display lower levels of activity in comparison to young active stars.

Most of our lessons regarding stellar activity on G stars have been informed by our own host star, the Sun, a G2 star (Morgan, 1973). However, within the last two decades new photometric observations have revealed the levels of surface activity on other G type stars (0.8-1.1 M_{sun}). For instance, we now know our Sun is less active in comparison to other G type stars (Reinhold et al., 2019b). Furthermore, G stars can exhibit high occurrence rates of super flares (e.g. Shibayama et al., 2013; Notsu et al., 2013; Maehara et al., 2015; Okamoto et al., 2021) and also have large starspots on their surfaces (Namekata et al., 2019).

Sitting right in between G and M stars are the K stars (0.5-0.8 M_{sun}), which make up about 8% of the stars on the main sequence. Flares have also been detected on their surfaces with a higher occurrence rates than on G stars but overall less energetic of events (Walkowicz et al., 2011a; Howard et al., 2020). K stars with exoplanets have also been described as advantageous targets to consider for direct imaging. Their star-planet contrast ratio and shorter pre-main sequence phases may allow for the preservation and detection of biosignatures (Arney, 2020).

For this thesis, we primarily focus on the smallest ($\leq$ 0.5 M_{sun}) types of stars in our universe, M stars. We see elevated levels of magnetic activity on M stars due to their strong magnetic fields (Kochukhov, 2021). M stars are some of the most abundant stars in our universe, comprising over 70% of the stellar population (Henry et al., 2006). M dwarfs are also good targets for searching for exoplanets (e.g. Dressing & Charbonneau, 2013; Ballard & Johnson, 2016) via the transit and radial velocity methods. Their small radii and low temperatures allow for the detection and characterization of planets that are on shorter orbits (Kaltenegger & Traub, 2009).

In the subsections below, I detail some of the observable manifestations of stellar magnetic activity that have been studied on stars beyond our Sun.

1.2.1 Flares

Stellar flares are energetic events that occur on the surface of stars and are a result of the reconnection of magnetic field lines (Benz, 2008). The first observation of a solar flare dates back to 1859 (Carrington, 1859). The radiation released during these explosive events can be detected across the entire electromagnetic spectrum. Figure 1.2 shows a schematic of a solar flare and the radiation mechanisms at play. For instance, if we consider the radiation mechanisms of a white-light flare we would first detect synchrotron emission caused by a beam of energetic electrons spinning down to impact and heat the photosphere. The "white-light" detected is the thermal response of the atmosphere and we primarily detect blackbody emission from optical flares. Once the electron beam turns off, we start to see the non-thermal effects of flares (an increase in energy) followed by the thermal effects (cooling phase) once the flare event ends. We also detect flare emission at X-ray all the way to radio wavelengths (Osten et al., 2005). The emission detected at each wavelength regime tells us information about both the emission mechanisms at play and the different stellar atmospheric lines that are enhanced during a flare.

Flares are believed to share a common underlying physical formation mechanism and have been observed on our Sun as well as on all types of main sequence stars that have outer convection envelopes (Pettersen, 1989). For instance, we see flares occurring on the Sun (e.g. Pearce & Harrison, 1990), on low mass stars (e.g. Lacy et al., 1976; Pazzani & Rodono, 1981; Doyle et al., 1990; Panagi & Andrews, 1995), and on RS CVn binaries (e.g. Osten & Brown, 1999). Flares typically occur over short timescales ranging from minutes to hours (Hawley et al., 2014) and they emit energy ranging from 10^{23} erg (nanoflares; e.g. Parnell & Jupp (2000) up to energies as high as 10^{38} erg (super flares; e.g., Shibayama et al. (2013).

1.2.2 Other Forms of Activity

Stars also display various other forms of magnetic activity on their surfaces. Below I give a brief description of the activity features that are most prevalent in our current photometric

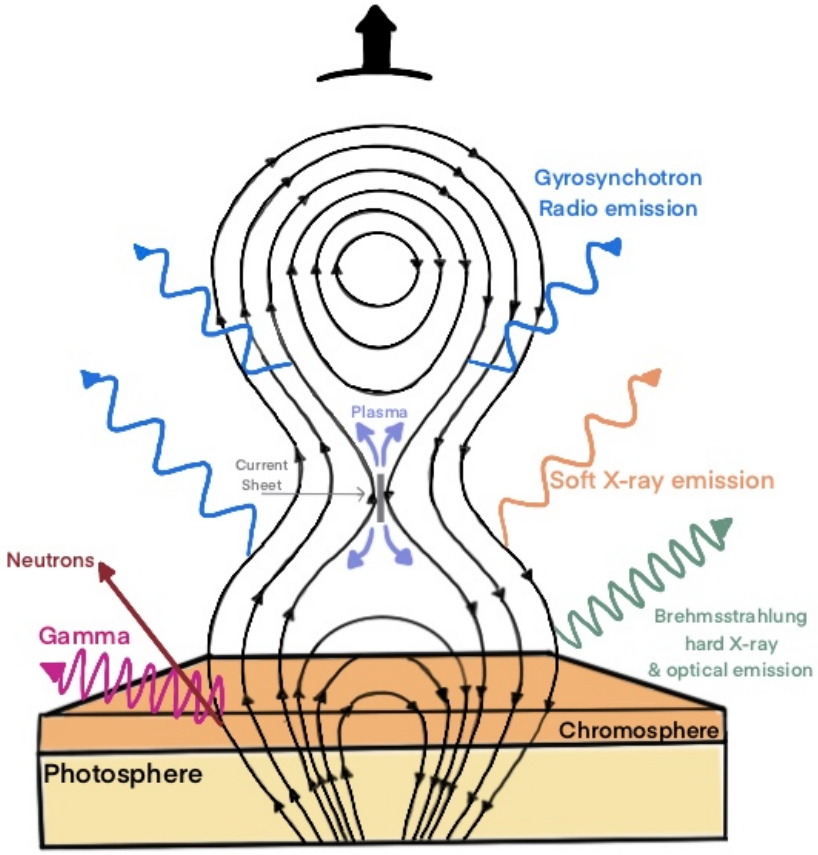

Figure 1.2 Illustration of a flare, modified from (Martens, 1989; Bazilevskaya, 2017). In black are the magnetic field lines that create the flare loop. The multi-colored arrows indicate the various emission forms that are detected when a flare occurs. The black arrow at the top indicates the shock front and potential CME that flares can often trigger.

observations of active stars.

Starspots

Starspots are dark, relatively cooler regions that appear on the photosphere of a star. They are caused by intense magnetic activity, where strong magnetic fields inhibit the convective flow of hot gases from the star's interior, leading to localized cooling (Berdyugina, 2005). On the Sun, these spots occur in pairs or groups and can vary in size from a few thousand kilometers to tens of thousands of kilometers across. They are typically cooler than the surrounding solar surface due to the inhibition of convective energy by the magnetic field, with temperatures 1000-1900 K cooler than the quiet Sun (Solanki, 2003). The number and distribution of sunspots on the Sun's surface is correlated with the 22 year solar cycle (Berdyugina, 2005). Starspots have also been studied on active main sequence stars (Hawley et al., 2014; Montet et al., 2017a; Morris et al., 2018; Namekata et al., 2019). More recently, they have been a source of noise in exoplanet transit transmission data, hindering our ability to disentangle stellar signals from planetary ones (Haywood et al., 2014; Rackham & de Wit, 2023; Lim et al., 2023). Continued photometric and spectroscopic observations of active stars will provide valuable insights into the physics of starspots and their influence on exoplanet space weather.

Faculae

Faculae are bright features that also appear on the photosphere of stars. Faculae are hot areas primarily composed of magnetic fields that emerge from the solar interior, causing localized heating and increasing the brightness of the surrounding photosphere (Berger et al., 2007). Faculae are often found in regions of intense magnetic activity, such as near sunspots or active regions, and they can persist for days to weeks. Similar to starspots, faculae have also been a source of contamination in exoplanet atmosphere observations (Rackham et al., 2018; Moran et al., 2023; Lim et al., 2023). Many efforts have tried to model the signal of these features to both better understand their properties and remove them from exoplanet

observations (Reinhold et al., 2019a; Johnson et al., 2021). Upcoming missions such as the Pandora satellite seek to place constraints on the covering fraction of faculae on active stars that also host exoplanets (Quintana et al., 2021).

Coronal Mass Ejections

Coronal mass ejections (CMEs) are explosive events that occur on our Sun as well as on other stars, where vast amounts of plasma and magnetic flux from the outer atmosphere (corona) are ejected into space. The earliest detection of CMEs on our Sun date back to observations from the total solar eclipse in 1860 (Eddy, 1974). CMEs tend to form near areas with localized fields of strong and stressed magnetic flux, such as active regions associated with starspot groups. CMEs can also occur near locations where relatively cool and denser plasma is trapped and suspended by magnetic flux extending up to the inner corona - near filaments/prominences (Low, 1990). During a CME, as much as 10^{12}kg of mass is hurled away from the Sun at speeds ranging from a few hundred to over 3,000 kilometers per second (Gopalswamy, 2016). The rate of occurrence varies with the magnetic activity levels of the star. For instance on our Sun, the occurrence rate of CMEs correlates with the solar cycle, from one every few days at minimum to a few per day at maximum (Webb & Howard, 2012).

Observations of CMEs on other stars remain a challenge because the close stellar environment cannot be spatially resolved like it is on the Sun (Odert et al., 2017). Furthermore, both CMEs and the stellar corona are low density environments preventing us from easily observing the CME outburst and associated stellar winds. However, Zeeman-Doppler Imaging (ZDI) has provided information about the varying magnetic field strengths of other active stars (Donati & Landstreet, 2009), which has provided insight to what magnetic field strengths are necessary to generate CMEs. Recent work by (Veronig et al., 2021), has reported coronal dimmings (at X-ray and extreme UV wavelengths) as indirect evidence of stellar CMEs on low mass K and M stars. In addition, recent work by (Namekata et al., 2022) revealed evidence for a stellar filament eruption associated with a super flare on a solar-like star using spectroscopic observations of a blue shifted hydrogen absorption com-

ponent. The study of CMEs on other stars is particularly important when we consider the astrobiological implications. CME particle events can completely erode the atmosphere of a planet(Vida et al., 2017), and thus having constraints on the occurrence rate for these events would allow us to more holistically understand star-planet environments.

1.3 Astrobiology and Habitability

We are in the era of exoplanet characterization. Over the last few decades we have learned that planets are ubiquitous and some may be able to harbor the conditions necessary for life to emerge, getting us one step closer to answering the age old question of "are we alone in the universe?". Simultaneously, we have begun to more closely analyze the relationship between stars and their planets. Understanding the relationship between stars and their planets is a key scientific goal for the next decade as defined in the Astro2020 Decadal Survey's 'Worlds and Suns in Context'key theme area. For one must place these exoplanets in the context of their environment to be able to holistically assess the probability of habitability.

Stellar magnetic activity has long influenced our ability to detect and characterize extra-solar planetary systems. In particular, high rates of stellar flares and high-energy radiation of main sequence stars can have strong impacts on the environment and atmosphere of a planet, raising questions about the potential habitability of these worlds. There are many examples of the impacts stellar activity has on exoplanets. For instance, in the case of the flare star AU Mic, a flare event occurred at the same time the planet AU Mic b was transiting (Plavchan et al., 2020), which caused errors in the measured transit depths and durations. In addition to detectability, many teams have shown that strong magnetic activity (i.e flares and CMEs) can affect planetary atmospheres (e.g. Segura et al., 2010; Vida et al., 2016; Tilley et al., 2019) and thus influence potential habitability by causing runaway greenhouse effects (Shields et al., 2016), atmospheric erosion (Lammer et al., 2007) and hydrodynamic escape of atmospheres (Luger et al., 2015).

It is known that flares can alter the chemistry of planetary atmospheres (e.g. Venot et al., 2016; Chen et al., 2021). In the more optimistic cases, stellar magnetic activity (in

particular flares) may power prebiotic chemistry (Airapetian et al., 2016). Other studies have also suggested that flare events might be the only way to deliver the UV photons necessary to initiate life around M-type stars (e.g. Ranjan et al., 2017; Rimmer et al., 2018). Therefore, it is important to constrain the flare properties of exoplanet host stars in order to gain a clear picture of the evolution and habitability of their planets.

1.4 Multi-Wavelength Datasets

During the course of my PhD studies I have had the opportunity to work with a number of datasets. Below, I give a brief description of each of the telescopes and provide a few examples of the impact they have had on stellar flare science.

1.4.1 Kepler/K2

The era of all-sky, high-precision, time-series, photometric missions has allowed for many detailed studies of stellar activity. Since its launch in 2009, the *Kepler* Space Telescope has revolutionized our understanding of stars and their exoplanets. *Kepler* was designed to stare at a patch of the night sky near the constellation Cygnus and monitor main sequence stars in search of Earth-sized planets (Borucki et al., 2010). *Kepler* performed observations at optical wavelengths (420-900nm). Within the first few months of operations *Kepler* detected its first planets(Batalha et al., 2013), and by the end of the primary mission we had constraints on planet occurrences (Dressing & Charbonneau, 2013). Four years after launch, the telescope lost one of its reaction wheels which affected its precise pointing abilities. However, engineers were able to use the pressure of sunlight to maintain its pointing. These corrections meant K2 was only able to observe along the ecliptic plane for shorter periods of time ($\sim$80 days). Under this new schematic, K2 (Howell et al., 2014), still continued to find exoplanets.

Since its retirement in 2018, *Kepler*/K2 confirmed the discovery of over 3,000 exoplanets and over 2,000 candidates are yet to be confirmed other observatories (see Figure 1.3). The multi-year photometric observations have provided a rich dataset for flare studies. For instance, we now have many catalogs of flare events across a range of active stars, which have

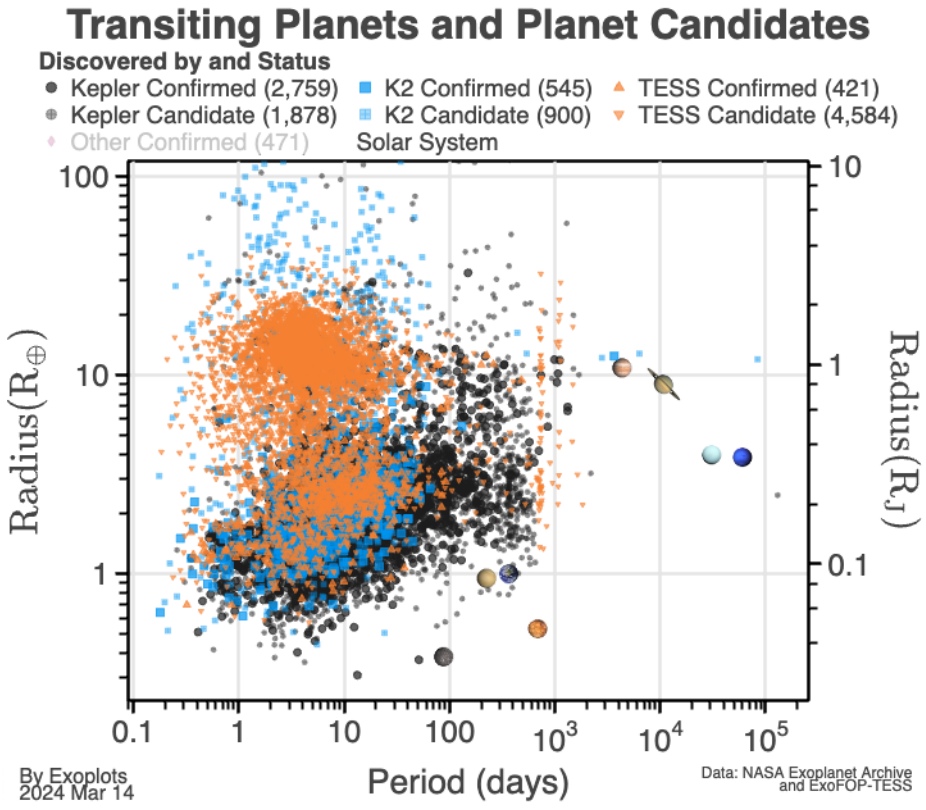

Figure 1.3 Transiting exoplanets and planet candidates that have been discovered by *Kepler* (black), K2 (blue), and TESS (orange) as of March 2024. Shown on the x-axis is the orbital period in days, as a function of Earth radii.

become key tools for modeling the energetic flare events (e.g. Hawley et al., 2014; Walkowicz et al., 2011b; Davenport, 2016; Tovar Mendoza et al., 2022). In addition, we have been able to study flare rates and activity cycles over time (Montet et al., 2017a; Davenport et al., 2020).

1.4.2 Transiting Exoplanet Survey Satellite

In 2018, the Transiting Exoplanet Survey Satellite (TESS) launched with a primary mission of detecting transiting exoplanets around some of the closest and brightest stars in our galaxy (Ricker et al., 2014). TESS's bandpass covers optical to near-infrared wavelengths (600-1000nm). To date, TESS has confirmed over 400 planets and identified over 7,000 exoplanet candidates (see Figure 1.3). Many of the worlds TESS has discovered are amenable for follow up with large ground based observatories as well as JWST.

The precise, high cadence data has also been instrumental for flare studies. For instance, TESS data has been used to create flare catalogs of some of the most active stars (Feinstein et al., 2020; Günther et al., 2020) and study flare characteristics such as temperatures (Howard et al., 2020) and morphologies (Howard & MacGregor, 2021). Furthermore, TESS has been critical for simultaneous and multi-wavelength flare studies (Barclay & Barentsen, 2018; Paudel et al., 2021; Jackman, 2022; Paudel et al., 2024).

1.4.3 Spitzer Space Telescope

The Spitzer Space Telescope, operated by NASA from 2003 to 2020, revolutionized our understanding of the universe at infrared wavelengths (3-180 microns) (Werner, 2005). Among its top discoveries was the detection and characterization of exoplanets, including the first detection of an exoplanet atmosphere (Deming, 2005; Agol et al., 2010). More recently, Spitzer has been essential to the detection and characterization of the famous TRAPPIST-1 exoplanet system (Delrez et al., 2018; Davenport, 2017). Since concluding operations, the Spitzer data archive remains a rich data set for studying stellar flares in the infrared. In particular, the data allows us to detect and characterize infrared excess emission associated

with flaring events (Kowalski et al., 2013), providing clues about the energy release, heating mechanisms, and properties of the flaring regions on stars.

1.4.4 Gaia

Gaia is a European Space Agency (ESA) mission that launched in 2013 with a primary mission to chart the positions, parallaxes, proper motions, and properties of more than a billion stars in the Milky Way (Prusti et al., 2016). Gaia's observations have far-reaching implications beyond stellar cartography. The mission also delves into the study of exoplanets (Berger et al., 2023) and stellar evolution (Hodgkin et al., 2021). Furthermore, Gaia also maintains an alert system that flags transient events that have rapid changes in brightness (e.g. supernovae, flares). Within the alerts, there is simultaneous photometry and low-resolution spectra available (Montegriffo et al., 2022) for each target. Future Gaia data releases will provide the mean spectra for these objects which will enable flare temperature studies.

1.4.5 Nancy Grace Roman Space Telescope

The Nancy Grace Roman Space Telescope (Roman), is NASA's next flagship mission set to launch in late 2026 (Spergel et al., 2015). Roman is a wide field survey that will explore the universe using 8 science filters with overlapping bandpasses spanning 0.48 – 2.3 microns. Roman seeks to answer fundamental questions about cosmology and exoplanets by conducting three core community surveys. Roman's Galactic Bulge Time Domain Survey (GBTDS) seeks to detect gravitational microlensing events caused by exoplanets in the Galactic bulge (Wilson et al., 2023). However, this survey will also be leveraged to study stellar flares. Large area surveys have never been performed before in the Roman spectral range, and Roman will reveal new information on how flare rates change with stellar age and metallicity. For instance, the Galactic Bulge stars will be much older than the typical studied flare stars, and Roman's wide field and exquisite imaging may provide sufficient statistics to probe the flare behavior and properties of such an old stellar population. In addition, flares may be

confused with rare, short-timescale, microlensing events caused by free-floating planets and disentangling the two signals will be important.

1.5 Outline of Thesis

The outline of this thesis is as follows. In Chapter 2, I detail the development of an analytic, continuous and open source flare template that models the morphology of stellar flares in photometric data. Specifically, I revisit one of the most active stars from the Kepler mission, the M4 star GJ 1243. I use 11 months of 1-minute cadence light curves to study the empirical shape of white-light stellar flares. The flare template can be used to model flares from different datasets (e.g. TESS & Gaia) and at different cadence modes. To date, the flare model has also been used to model and subtract out flares from photometric datasets. Furthermore, we compare the resulting flare properties from the Kepler and TESS datasets to study the multi-wavelength properties of flares.

In Chapter 3, I use archival Spitzer data to understand the infrared flares of TRAPPIST-1. Using the largest sample of infrared flares gathered to date for this star, I explore how infrared flare temperatures compare to optical estimates, and the implications this has for the exoplanets in orbit around TRAPPIST-1. I conclude by comparing our results to the latest JWST flare observations of TRAPPIST-1.

In Chapter 4, I extend my work to consider the capabilities that future missions such as the Nancy Grace Roman Space Telescope (Roman) will have on stellar flare science. Roman will survey millions of stars in the galactic bulge in search for planets, many of which will be in orbit around active flare stars. I simulate Roman light curves with realistic noise properties and use a flare frequency distribution model to inject flares into the light curves. Then, we run performance recovery tests, which allow us to assess the total expected flare yield across spectral type. We find that Roman will need to consider cadence, filters, and read-out strategies in order to maximize and expand our knowledge of stellar magnetic activity.

Chapter 5 provides conclusions and future directions of my thesis work. I explain how we can leverage the use of multi-wavelength observations of flares to constrain flare temperatures

and understand their impact on exoplanet atmospheres. In addition, I highlight future observatories that will be coming online and will provide insights to stellar flare science in the next decade.

Chapter 2

LLAMARADAS ESTELARES: MODELING THE MORPHOLOGY OF WHITE-LIGHT FLARES

Portions of this chapter were originally published in collaboration with James R. A. Davenport, Eric Agol, James A. G. Jackman, and Suzanne L. Hawley (June 2022) edition of the Astronomical Journal (Tovar Mendoza et al., 2022, AJ, 164, 17; 2022c American Astronomical Society, DOI: 10.3847/1538-3881/ac6fe6), and are reproduced below with the permission of the American Astronomical Society.

2.1 Summary

Stellar variability is a limiting factor for planet detection and characterization, particularly around active M-type stars. Here we revisit one of the most active stars from the *Kepler* mission, the M4 star GJ 1243, and use a sample of 414 flare events from 11 months of 1-minute cadence light curves to study the empirical morphology of white-light stellar flares. We use a Gaussian process detrending technique to account for the underlying starspots. We present an improved analytic, continuous flare template that is generated by stacking the flares onto a scaled time and amplitude and uses a Markov Chain Monte Carlo analysis to fit the model. Our model is defined using classical flare events, but can also be used to model complex, multi-peaked flare events. We demonstrate the utility of our model using *TESS* data at the 10-minute, 2-minute and 20-second cadence modes. Our new flare model code is made publicly available on GitHub .

2.2 Introduction

Stellar flares are energetic events that occur on the surface of stars and are a result of the reconnection of magnetic field lines (Benz, 2008). They are believed to share a common underlying physical formation mechanism and have been observed on all types of main sequence stars that have outer convection envelopes (Pettersen, 1989). For instance, there is evidence of flaring on low mass stars (e.g. Lacy et al., 1976; Pazzani & Rodono, 1981; Doyle et al., 1990; Panagi & Andrews, 1995), RS CVn stars (e.g. Osten & Brown, 1999), and on the Sun (e.g. Pearce & Harrison, 1990). On the Sun, we see how the variety of magnetic activity ranging from large scale surface events such as spots, coronal mass ejections (CMEs), and flares gives rise to significant photometric variations (Carrington, 1859). From the Sun, we expect flares to occur near active regions on a star (Benz & Güdel, 2010). However not all stars follow this behavior; the M-type star GJ 1243 is an example of a star that has flare events happening all over the surface of the star with no significant correlation to the starspot phase (Hawley et al., 2014). Several studies have argued this is because the spot coverage on young active stars is 80% or greater (Gully-Santiago et al., 2017; Feinstein et al., 2020). Meanwhile, for fully convective stars it has been shown that flares may occur at very high latitudes because magnetic fields are emerging close to the stellar rotational poles (Ilin et al., 2021b). Since the polar regions are always visible, unless the inclination is 90 degrees, we can observe the flare events. The ubiquity of flares present among low mass stars motivates further study of their flare frequencies and morphologies.

Stellar magnetic activity has long influenced our ability to detect and characterize extrasolar planetary systems. For instance, in the case of the flare star AU Mic, a flare event occurred at the same time the planet AU Mic b was transiting (Plavchan et al., 2020). The flare was masked out, which caused greater uncertainty in the transit ingress/egress profile. In addition to detectability, many teams have shown that strong magnetic activity (i.e flares and CMEs) can affect planetary atmospheres (e.g. Segura et al., 2010; Vida et al., 2016; Tilley et al., 2019) and thus influence potential habitability by causing runaway greenhouse

effects (Shields et al., 2016), atmospheric erosion (Lammer et al., 2007) and hydrodynamic escape of atmospheres (Luger et al., 2015). By better understanding the temporal evolution or light curve morphology of flares on active M-type stars we can help improve exoplanet detection and characterization (Gilbert et al., 2021).

The *Kepler* space telescope has provided long duration, high-precision, optical light curves that are advantageous for studying stellar variability phenomena (Borucki et al., 2010). Many catalogs of flares have been created from the *Kepler* data (e.g. Hawley et al., 2014; Davenport, 2016; Martínez et al., 2019). The catalogs have been useful tools to aid in our ability to understand and model these stellar energetic events.

While it is generally understood that flares share a common physical origin (e.g. Benz, 2008), there are many different parameterizations that have been used to describe what we see during flare events. Previous studies modeled flares using single exponential profiles, fast rise exponential decay (FRED) profiles, or combinations of a Gaussian plus an exponential (e.g. Walkowicz et al., 2011b; Loyd & France, 2014). However, these models ignore the two-phase cooling decay that is typically observed during flare events (e.g. Andrews, 1965; Hilton, 2011; Davenport et al., 2014). More recently, many have studied the morphology of flares from white-light flare profiles that have impulsive and gradual phases (Kowalski et al., 2013), as well as possible quasi-periodic oscillations during flare events (e.g. Pugh et al., 2015). In addition, higher cadence observations have resolved the flare peaks and found they roll over, emphasizing the need for a continuous model that does not have break points between the rise and decay phases (e.g. Kowalski et al., 2016a; Jackman et al., 2018, 2019; Howard & MacGregor, 2021).

Davenport et al. (2014, hereafter D14) used *Kepler* short cadence data from data release 23 (DR23) of GJ 1243 to understand the characteristics of flare light curves and found that when many flares are averaged together, a median flare template can be generated. This has proved to be very useful for modeling flare light curves from a variety of surveys (e.g. Schmidt et al., 2019) and has helped with modeling transits in the presence of flares (e.g. Luger et al., 2017b). However, this flare template has some major limitations. The D14 model

used a piece-wise function to parameterize the flare shape, which causes a discontinuity at the peak of a given flare event. The model used the peak time and amplitude as two of the parameters, which are very sensitive to scaling effects. Finally, this model used a local smoothing function to detrend the underlying starspots around the flares. This approach is not as robust as new statistical methods, such as Gaussian process regression (Rasmussen & Williams, 2006), which also provides the uncertainties of the starspot profile.

In this paper, we derive an updated analytic and continuous flare model to parameterize white-light flare events that addresses the limitations of previous models. We start by considering the model introduced in Jackman et al. (2018), which uses the parameterization from Gryciuk et al. (2017) and provides a template for modeling flares. This model is continuous but it is only derived from a small number of individual flares. To address the small number of flares, we use a vetted version of the D14 flare catalog to derive an updated template. Thanks to improvements in *Kepler* light curve processing, updates to statistical techniques that allow us to detrend starspots, new parameterizations, and a newly vetted dataset, we are now able to address the limitations of the D14 flare template. We present the details of the updated flare model below and also make the code readily available on GitHub .

The outline of the paper is as follows: In §2.3, we revisit the GJ 1243 flare sample from *Kepler* data. In §2.4 we describe starspot detrending using Gaussian process regression. Using the flare sample and starspot detrending, we reproduce the original flare template in D14. In §2.5, we introduce a new analytic flare model adapted from Jackman et al. (2018) and compare to other analytical models. Then in §2.6 we present a new method for constructing the flare template that further addresses some of the limitations present in D14. In §2.7, we explain the model fitting procedure and analysis. Next, §2.8 explores various applications of this new model. We conclude with a discussion of the implications of our study, and the promising future for stellar activity studies that combine *Kepler* and *TESS* data in §2.9.

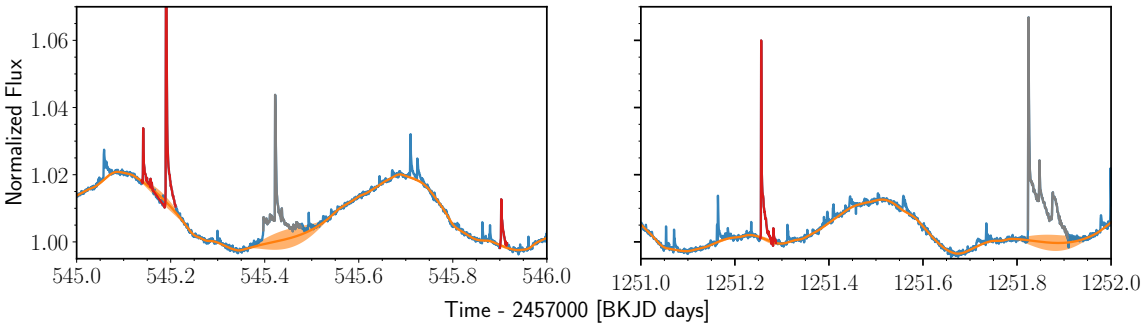

Figure 2.1 Two days of GJ 1243 *Kepler* 1-minute observations are shown in blue. The identified classical flares (red), the GP mean (orange) and variance are all overlayed. **Left**: We identified three classical flares during this window. **Right**: We identified two classical flares that were used to derive the flare model. Note there are two complex flares (grey), one in each panel, but these were not used to construct the flare template. To accurately model the underlying starspot modulations we masked out all flares which allowed the GP to model the starspot variability without being skewed by frequent flaring events. Therefore, we expect the GP to have the highest variance in areas where flares are occurring.

2.3 Defining the Flare Sample

For this study, we revisit GJ 1243 (KIC 9726699), one of the benchmark stars for space-based flare studies (Hawley et al., 2014). This dM4e star is the most active flare star in the *Kepler* field. The high level of activity observed on the star is directly correlated to its young age of 30-50 Myr (Silverberg et al., 2016). GJ 1243 has a luminosity of $\log L_{Kep} = 30.68 \pm 0.04$ erg s^{-1} in the *Kepler* bandpass (Davenport et al., 2020), an estimated effective temperature of 2,661 K and an estimated mass of 0.094 $M_{\odot}$ (NASA Exoplanet Archive, 2016). We used 11 months of the `PDCSAP_FLUX` (Smith et al., 2012), 1-minute short cadence light curves from *Kepler* Data Release 25[1], and required the `Quality` flag be set to 0 to minimize the number of errors from spacecraft events. The *Kepler* short cadence data was released in months, as opposed to the long cadence data that was released in quarters (1 quarter = 3 months). Therefore, we stitched 11 months of data together in order to create one light curve. We accounted for the quarterly discontinuities by taking the median of the fluxes across each of the months of data and then normalized the light curve by dividing by the total median.

We use the GJ 1243 flare sample from D14 to study the morphology of white-light flares. To create the sample, D14 developed an IDL tool, Flares By EYE (FBEYE), that ran a smoothing and auto-finding algorithm to identify candidate flares. Users would then manually analyze the light curve to verify and classify flares. The final sample contained 6107 flare events, which is the largest flare sample for a single star to date.

Since the D14 study, there has been a new *Kepler* data release (DR25). DR25 included improvements in light curve processing, which altered the classifications of previously identified flare events. For instance, some flare events in DR23 that were used in D14 now appear to be within the 3σ noise limit and/or now appear to be complex events in DR25. We manually inspected all 885 classical flares defined in D14 with the new DR25 light curves. The new DR25 data had 379 flares that were re-classified as complex flare events, as well

[1] `https://archive.stsci.edu/kepler/release_notes/release_notes25/KSCI-19065-002DRN25.pdf`

as smaller flare events that were within the noise limit. These flares were removed from our sample since, as in D14, we are only using classical (single-peak) flare events to derive the flare template. Furthermore, we only used classical flares that had a total duration of at least 20 minutes and omitted any flares whose duration was longer than 75 minutes, since these flares have a higher likelihood of being complex events as found in D14. This yielded a total of 414 classical flare events that were used to construct the flare template compared to 885 flares used in D14. The main reason for the discrepancy has to do with the different data releases used for each study. The new vetted flare list provides a cleaner sample of classical flares that is then used to derive our updated flare template.

2.4 Modeling Starspot Variability

In the GJ 1243 light curve, we observe modulations that indicate the presence of two primary groups of long-lived starspots (Davenport et al., 2020). It has been shown that complex spot patterns can create non-sinusoidal variations as they rotate in and out of view (Angus et al., 2018). The evolution of such active regions, combined with differential rotation on the star's surface, can create quasi-periodic signals (Dumusque et al., 2011). Therefore, a strictly periodic model is not a robust or realistic model to use to account for the time series variations. Instead, we need a model that is flexible enough to capture the evolving quasi-periodic behavior that is present.

2.4.1 Gaussian Process Regression

Gaussian processes (GPs) are powerful models that allow us to make predictions about our data even when we do not know the functional form of the model. GPs fit the correlation between points and are defined by a mean function and a covariance matrix (Rasmussen & Williams, 2006). In astrophysics, GPs have been used as a model for stochastic variability in light curves of stars and to model instrumental systematics (e.g. Kipping, 2012; Haywood et al., 2014; Barclay et al., 2015; Angus et al., 2018; Barros et al., 2020). In the case of stellar variability, GP kernels can be defined to accurately model the photometric variability and

temporal evolution of starspot groups. Here we use a GP to improve the detrending of GJ 1243's starspots. In addition, GPs provide the variance of the modulation, which allows us to include the uncertainty resulting from this starspot detrending into our flare model. We can also use the linear component of the GP to account for the monthly variations in the data.

D14 used a local spot detrending technique to subtract the starspot features around each flare event. Their approach used a custom smoothing function to smooth the light curve and any data that was more than 1σ away from the defined boxcar kernel was removed. The resulting light curve was then fit using a cubic spline and the starspot curve was subtracted from the original light curve. While this approach allows for a quick way of identifying flares in the presence of spots, the resulting starspot model can still have contaminant flares present causing us to miss the curvature of the starspot modulation happening under the flare. This is important to highlight because the starspot model is what gets subtracted from the original light curve, that then is used to identify the flares that are used to construct the flare template. Therefore, if the underlying starspot variability is not accurately modeled there is no quantitative uncertainty that can be included into the flare model.

Here we use a GP for the starspot detrending. The GP was applied to each of the individual 11 months of data to model the underlying variability caused by starspots. Specifically, we use the stochastically-driven, damped simple harmonic oscillator described in Foreman-Mackey (2018) as the kernel to model the variability. In general terms, the kernel is the equation that defines the correlation between the given points and is chosen by the user to then define the covariance matrix. We note that newer kernels such as those described in Gordon et al. (2020) include additional terms that account for various noise components which are particularly useful for improving measurements of stellar rotation or transit parameters. However for our case, the simple harmonic oscillator kernel is suitable for describing the correlated noise since the shape of the starspot evolves over timescales much longer than flares and thus the choice of kernel should not have a significant impact on our results. The initial parameters used for the GP follow those described in Foreman-Mackey (2018) where,

Q= 0.01 and $\omega = \frac{2\pi}{P_{rot}}$. We use a rotation period of 0.59 days, which was measured from light curve modulations of the star spots (Savanov & Dmitrienko, 2011) and again with ground based data by Irwin et al. (2011). The kernel parameters were optimized by maximizing the likelihood over each month of *Kepler* data.

To ensure the GP was not skewed by the frequent flaring events we masked out all of the flares (classical and complex) present in the data. To account for any flare events that might have been cut off (i.e flares with long decay phases), we added a buffer of 0.25 x t_{flare} to the start time and 0.5 x t_{flare} to the stop times of each flare defined in D14, where t_{flare} refers to the duration of the flare event. The result was a mean GP model describing the starspot variability for GJ 1243 with the corresponding variance of the model as highlighted in Figure 2.1. The variance envelopes (i.e areas where the model has the highest uncertainty) correspond to places where flare events have been masked out, which is what we expect. The larger flares give rise to a higher GP error and are also more evident because they have a longer duration. However, even in the presence of large complex flares, we can still see the substantial curvature of the starspot modulation traced by the GP. In areas where small flares occur, the GP variance is significantly smaller.

2.5 Continuous Flare Model

Flares share a common underlying formation mechanism, therefore a time dependent profile can be derived to model the observed flare morphology, as shown in D14. The median flare template can be described by an analytic function. To improve on the flare profile from D14, we use the convolution of a Gaussian and a double exponential to model the morphology of the flares as shown in Jackman (2020). This improves on the work of Gryciuk et al. (2017) who fit data of X-ray solar flares using the convolution of a Gaussian and a single exponential. Both approaches avoid the sharp flare peak (discontinuity) that is present in the D14 model.

Mathematically, the flare profile, $f(t)$, is defined as:

$$f(t) = \int_{-\infty}^{t} g(x)h(t-x)dx. \tag{2.1}$$

The Gaussian term, $g(x)$, accounts for the impulsive heating that occurs during the rise phase of the flare, which has been used to model solar flares (Aschwanden et al., 1998), and takes the form:

$$g(x) = Ae^{(\frac{-(x-B)^2}{C^2})}. \tag{2.2}$$

Meanwhile, the double exponential, $h(x)$, accounts for the rapid and gradual cooling phases of the flare event that are described in D14:

$$h(x) = F_1 e^{(-D_1 x)} + F_2 e^{(-D_2 x)}. \tag{2.3}$$

By taking the convolution of these two functions we can account for the heating and cooling processes happening during each flare. Therefore, the updated flare template is based on a continuous function,

$$f(t) = \frac{\sqrt{\pi}AC}{2} \times \Big(F_1 h(t, B, C, D_1) + F_2 h(t, B, C, D_2)\Big), \tag{2.4}$$

where

$$h(t, B, C, D) = e^{-Dt+(\frac{B}{C}+\frac{DC}{2})^2} \times erfc(\frac{B-t}{C} + \frac{DC}{2}), \tag{2.5}$$

where erfc(t) is the complementary error function defined as 1-erf(t). The error function is commonly used in statistics and is defined as erf(t) = $\frac{2}{\sqrt{\pi}} \int exp(-s^2)ds$. It is available in the SciPy package (`scipy.special.erf`) for numerical evaluation.

The complete formula, $f(t)$, depends on the values of 8 parameters that help define the overall flare shape. These are:

t = relative time,

A = amplitude,

B = position of the peak of the flare,

C = Gaussian heating timescale,

D_1 = rapid cooling phase timescale,

D_2 = slow cooling phase timescale, and

F_2 = 1 - F_1, which describe the relative importance of the exponential cooling terms.

We note the limits of integration in Equation 2.1 are different than those in Gryciuk et al. (2017). Here we evaluate the model from $-\infty < x < t$ to correct for the fact that Gaussian functions are defined from $-\infty < x < \infty$. This mathematical correction also helped account for the divergent behaviour that was present with the previous parameterization implemented in Jackman (2020).

2.5.1 Comparing Flare Model Parameterizations

Fitting a continuous flare model to photometric observations gives us the ability to parameterize flare events. The convolution of a Gaussian and a single exponential template has been used to model flares and other explosive events such as supernovae (Papadogiannakis et al., 2019). Many of these events have a characteristic FRED profile. A single exponential decay model has been used frequently, especially while searching for flares among large catalogs (e.g. Walkowicz et al., 2011b; Loyd & France, 2014). While this model accounts for the heating phase, it does not accurately model the decay phase of flare events. A two-phase cooling profile for flares on M-type stars was proposed by Andrews (1965), which consisted of a sharp linear decline followed by an inverse square shape. The decay phase was later

parameterized observationally by Hilton (2011) with an initial linear decline and exponential profile. Spectroscopic analyses by Kowalski et al. (2013) also found emission components that suggest there are two distinct regions during the flare decay: one that cools more rapidly and another which cools slower. More recently, D14 used a double exponential to model the thermal and non-thermal cooling processes happening during the decay of stellar flares.

The convolution of a Gaussian and a double exponential has been shown to more accurately represent the heating and two-phase cooling processes that occur during flare events (e.g. Jackman et al., 2018, 2019). Physically, we get a continuous and analytic model that allows us to parameterize classical, single-peaked flare events and later decompose complex events into a series of classical events as seen in D14. Figure 2.2 shows the comparison between the D14 flare template and our new template. In comparison to the D14 piece-wise model, the updated analytic model does a better job at modeling the peak of the flare events and does not pin each flare to a relative peak flux of one. By using the new parameterization, updated detrending, and new starspot modeling techniques the updated flare model greatly improves our ability to parameterize flare events.

2.6 Stacking the Flares

Following the work of D14, we stacked all of the classical flare events onto a common time and flux axis to construct the flare template. The large sample of flares helps us achieve fine sampling. For instance, if the typical flare event is about 30 minutes long, we can get less than 1 second resolution by stacking hundreds of flares onto each other. By stacking the flares we get higher sensitivity to short timescale features.

We start by replicating the stacking procedure from D14. For each of the flares we first subtract off the starspot modulations from the mean GP, described in Section 2.4.1. Once the continuum is subtracted, we divide each flare by the maximum flux (peak) within each event. Each flare was therefore normalized to a relative flux scale between 0 (before and after the flare occurs) and 1 (peak flux). Each flare was also set to a relative timescale. To account for the rapid rise and decay phases, we linearly interpolated each flare to a time

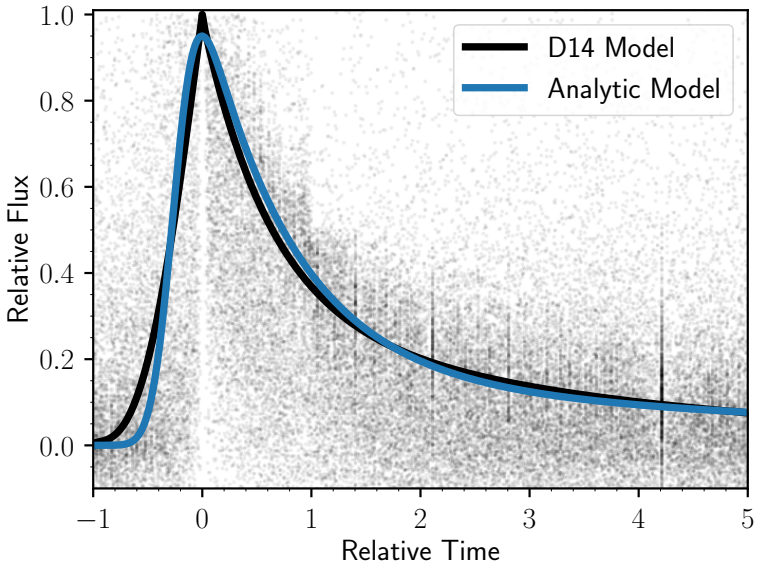

Figure 2.2 Comparison of the piece-wise flare template from D14 (black curve) and the initial version of our continuous flare model (blue curve). For reference, we show the full 885 flares sample stacked using the D14 procedure (grey points), which produces significant scatter in flux from forcing each flare to a peak of exactly 1. We also note the aliasing from improperly estimating the FWHM for short duration events (vertical bands) from the 1-minute cadence *Kepler* data.

resolution that was 10 times higher to yield a more accurate value of the full time width at half the maximum of the flux (FWHM), also known as $t_{1/2}$ in previous studies (Kowalski et al., 2013). This allowed us to reproduce the same flare stack that D14 created (see Figure 2.2), which was based on three free parameters: peak time, scale time, and amplitude.

However, the stacking procedure used in D14 has a number of limitations. One major limitation is that all of the flares were pinned at an infinitesimal peak of exactly one. This means the peaks of flare events were systematically underestimated and it also increased the relative flux scatter in the stack, which can be seen in Figure 2.2. By forcing all of the flares to align to a center time there is also an additional source of scatter added to the relative time. Furthermore, the stacking procedure used in D14, imprecisely estimated the

FWHM of flares by using an arbitrary linear up-sampling of the light curve. This caused scatter in the relative time, which created aliasing or over-dense regions of the stack as seen in Figure 2.2 (vertical grey bands). These features are present in the D14 paper, but cannot be seen due to the logarithmic contour map used to present the data in D14 Figure 4. D14 also used local polynomials to detrend the starspots, which are dependent on the order of the polynomials and the flare masking. This technique also did not provide the associated starspot model uncertainties, which were therefore not incorporated into the D14 model.

2.6.1 Improving the Stacking Procedure

Here we present an updated stacking procedure that addresses the limitations of the D14 stacking procedure. First, we used a non-linear least squares optimization to fit the initial version of our flare model shown in Figure 2.2 to each of the 414 flares in our sample. We used the parameters of the individual flares from D14 to initialize our fits. Our least-squares fitting was weighted by the photometric and GP errors added in quadrature. We then conceptually used the same alignment procedure as D14 to stack the flares, scaling each flare by the fit amplitude and FWHM, and aligning each event by the center time. Note this center time may not exactly correspond to the observed peak. By using these fits to align the flares, we are able to produce a stack that is not dependent on the peak estimate from the light curve, as in D14.

In Figure 2.3, we can see the updated model overlaid onto the stack of 414 classical flares that uses the new stacking procedure. In total, there are 13421 epochs of data represented among the stacked flares. We also show the binned median of the data (bins=200), and we can see the updated model traces the underlying shape of the flares. The stack of flares is much cleaner and has a reduced scatter in comparison to the stack of flares used in D14 (see Figure 2.2). The updated model therefore uses an updated stacking procedure that is less sensitive to sampling effects.

To quantitatively compare the two stacking procedures, we first fit a rolling median to each of the flare stacks. Then we calculated and compared a reduced χ^2 for each of the

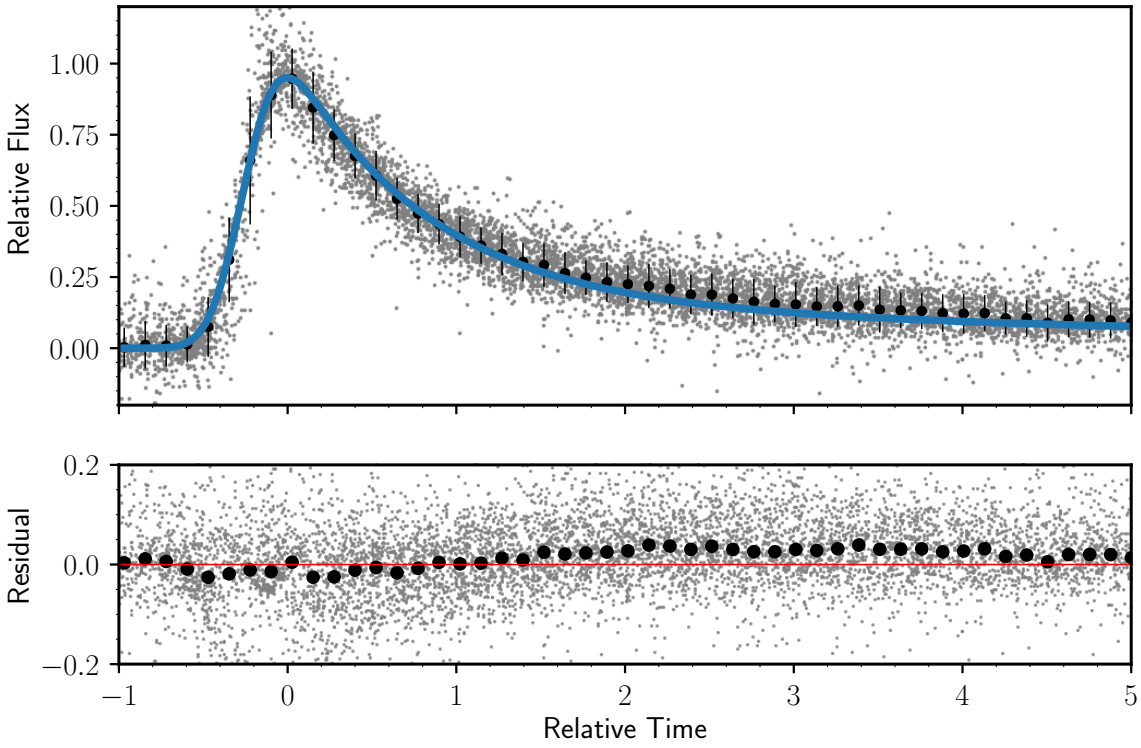

Figure 2.3 **Top:** The updated continuous analytical model (blue) overlaid onto the final vetted sample of 414 classical flares from the DR25 *Kepler* data release. The solid black points are the binned median with the respective standard deviation of the points inside of each bin. The flares are overlaid using a new stacking procedure that is less sensitive to sampling effects and scales each flare to a relative time and amplitude. **Bottom:** The residuals of the model (grey) and the binned residuals of the model in black which are mostly uniform and flat. The structure in the decay phase of the flares is caused by a combination of uncertainties in the stop times of flares and the starspot detrending. The combination of using a GP to model the starspots + continuous model + vetted flare sample + new stacking procedure has produced a more robust flare template.

Table 2.1. Best fit coefficients for Equation 2.4, and their respective uncertainties from the Markov Chain Monte-Carlo analysis, which define the flare shape as shown in Figure 2.3.

Parameter	Value	Uncertainty
A	0.969	7e-3
B	-0.2513	4e-4
C	0.2268	6e-4
D1	0.156	1e-3
D2	1.215	4e-3
F1	0.127	1e-3

resulting rolling medians. For the D14 rolling median we compute a reduced χ^2 of 16.5. Meanwhile we calculated a reduced χ^2 of 10.8 for the rolling median of the latest stack of flares. The lower χ^2 values that we calculated quantitatively demonstrate the improvements to the stacking procedure.

We also tried other stacking procedures to test which approach would further improve the flare model. Specifically, we drew from work in the exoplanet community that uses cumulative distributions to understand the distributions of planet eccentricities (Moorhead et al., 2011). However, this technique of using a cumulative distribution did not produce the correct center time and scale time alignments for flares. In comparison to the D14 model, we found that the updated stacking procedure used in this work both qualitatively and quantitatively improved the flare model.

2.7 Fitting the New Model

We use the python package `EMCEE` (Foreman-Mackey et al., 2013) to perform a Markov Chain Monte Carlo analysis, which fits the stacked flare sample. To initialize the walkers we used

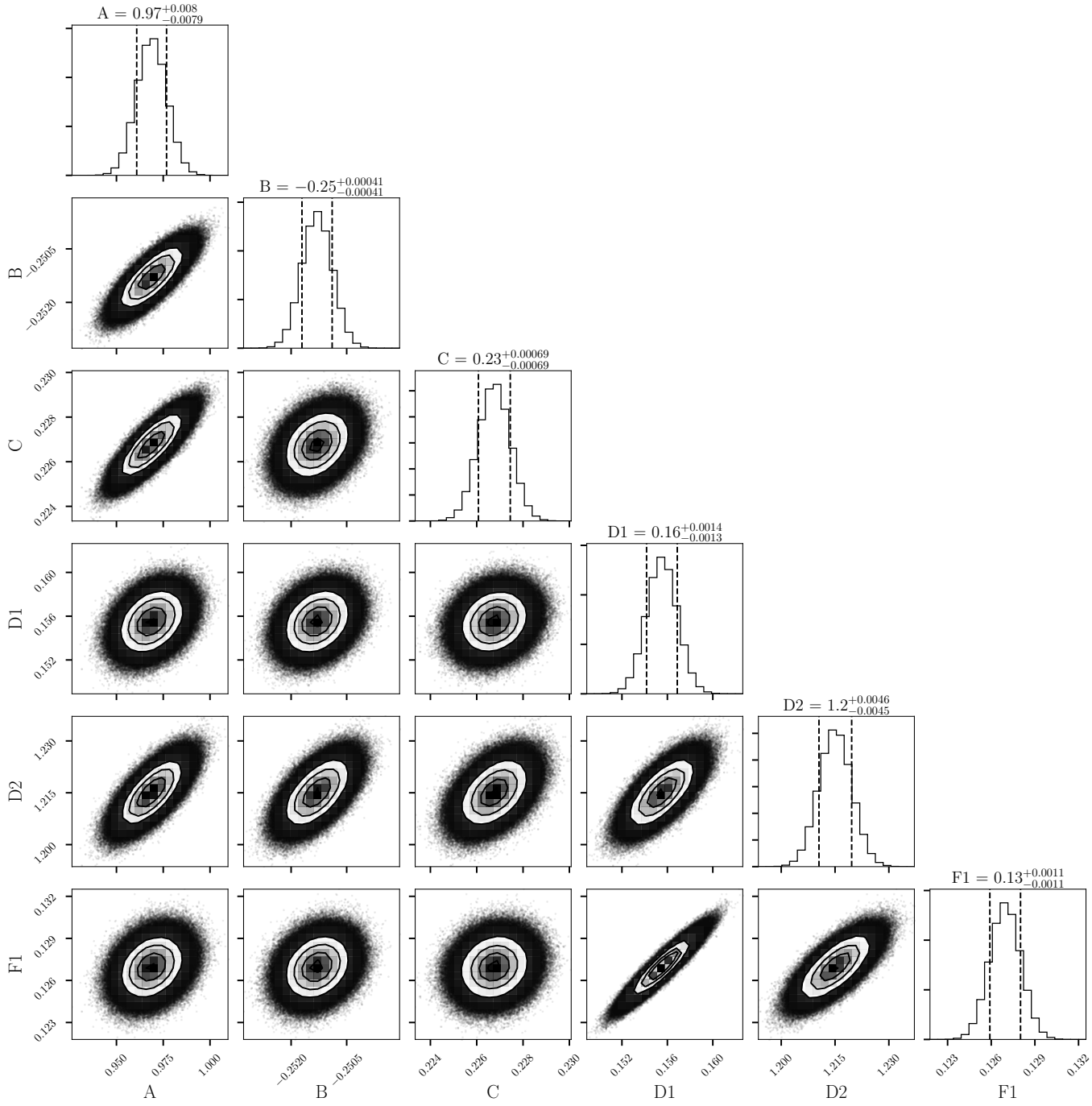

Figure 2.4 The results from the MCMC analysis showing the posterior probability distributions of each of the model parameters from Equation 2.4. This figure was made using `corner.py` (Foreman-Mackey, 2016).

our flare fits (see Section 2.6.1). We ran `EMCEE` using 256 walkers, 30,000 steps and we discarded the first 10% as burn in which we found was sufficient to reach convergence. The acceptance fraction was 0.516 with a mean auto correlation time of 65.01 steps. We used a χ^2 test with a tight boundary ($D1 > 0$) for our log likelihood model and assume a flat prior on all parameters. In addition, we used both the photometric and GP uncertainties added in quadrature. We note that the photometric errors are the ones that primarily contribute to the scatter, and the GP errors don't exceed the photometric errors. In the bottom panel of Figure 2.3, we include the residuals of the model and find that they are mostly uniformly scattered and flat. This tells us the data are well fit by our model. We see some structure in the residuals that correspond to the decay phase of the flare events. This structure is a result of uncertainties in the stop times of flares as well as uncertainties with the GP. During the end of the decay phases we reach comparable timescales with the starspots evolving and long tailed flares. Therefore, this is the regime where we are most affected by the GP detrending and the manual identification of the stop times of flares.

The best fit parameters from Equation 2.4 and their respective errors are presented in Table 2.1. In Figure 2.4, we present the typical corner plot of the resulting MCMC analysis, which shows the posterior probability distributions for each of the six model parameters. This fit defines the new flare template shape.

As in D14, this new flare template can be applied to observations via the same three scaling parameters used in making our stacked flare sample in Figure 2.3: center time, FWHM (also known as $t_{1/2}$ in Kowalski et al. (2013)), and amplitude. This is similar to the process used in scaling supernovae template to fit light curves (Papadogiannakis et al., 2019). In Figure 2.5, we show both an example of a classical flare profile that was modeled using our updated analytic flare template, as well as the three scaling parameters used to fit individual flares (center time, FHWM, and amplitude). The code for the updated flare model is made publicly available on GitHub .

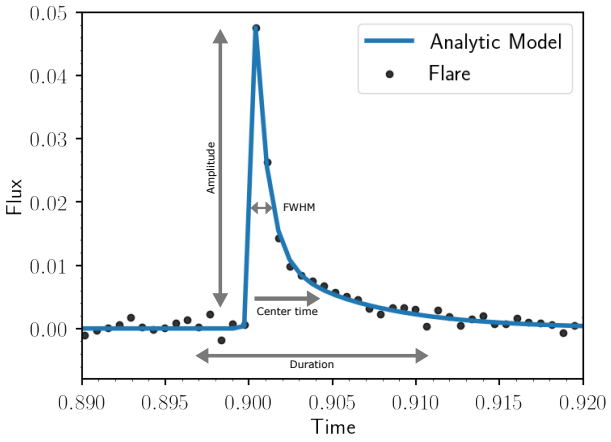

Figure 2.5 Example flare from the vetted set of *Kepler* classical flares with the analytic model overlayed. We show the final flare model can be parameterized using the following three scaling parameters: amplitude, FWHM, also known as $t_{1/2}$ in Kowalski et al. (2013), and center time (which is similar to tpeak in D14).

2.7.1 Model Comparison

The updated analytic flare model is both qualitatively and quantitatively more robust than the previous model presented in D14. In Figure 2.6, we can see the two flare models overlayed onto the vetted, 414 classical flares that were stacked using the new stacking procedure described in Section 2.6. Qualitatively, we can see the scatter from the stacked flares is both reduced and more uniform in comparison to the stacked flares shown in Figure 2.2. With the new stacking procedure we also account for the aliases that were present in the D14 stacking procedure that were a result of the alignment and scaling procedure used.

To quantitatively compare the two models, we calculated the reduced χ^2 for each of the stacking procedures that were used to derive the respective flare models. Using the D14 model and updated stacking procedure described in Section 2.6.1, we calculated a reduced χ^2 of 13.9. Meanwhile, the reduced χ^2 that uses the updated model derived in Section 2.7 and shown in Figure 2.3 is 9.1. This is a lower value in comparison to D14, showing the new

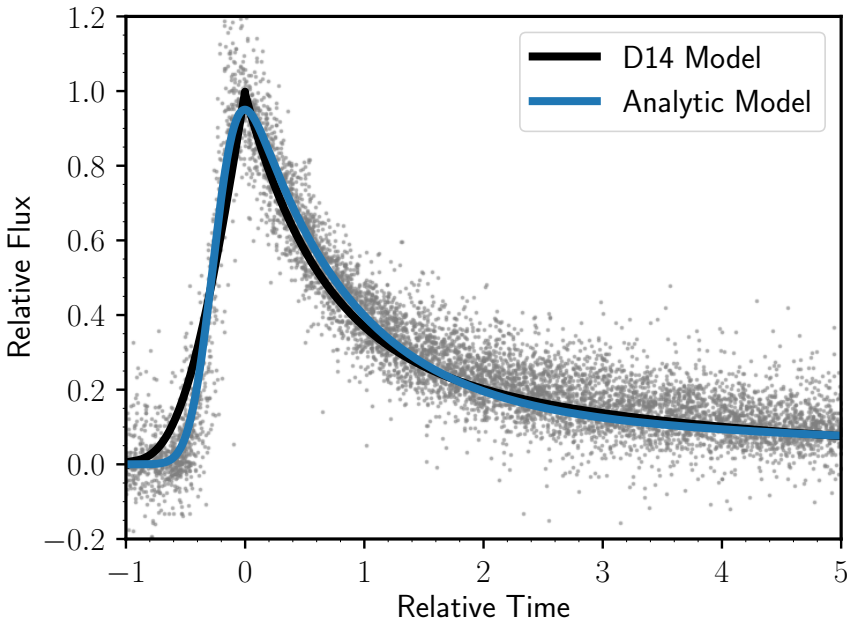

Figure 2.6 Comparison of the D14 and updated analytic flare templates overlayed onto the new stacked flares data set (grey points). The scatter in the data is from nearby, low energy flares. In black, is the piece-wise model from Davenport et al. (2014) and in blue one is the new analytic template that uses the convolution of a Gaussian and a double exponential. The updated analytic model is continuous and more accurately describes the peak of the flare events.

model is a better fit to the stack. In addition, we fit the vetted sample of 414 *Kepler* classical flares with both D14 and the new model. This allowed us to compare the changes between the resulting model fits for the same set of flares. We calculated the χ^2 of both models for every individual flare as a function of log flare energy. At higher flare energies ($logE > 31$) we find the updated model shows a lower χ^2, indicating the new model provides a better fit for higher energy flares. This is likely due to decreased resolution for lower energy flares. Overall, the updated model presented in this work has a lower χ^2 for an individual flare in comparison to the D14 model.

Table 2.2. Classical Flare Properties

t_{peak} (days)	FWHM (days)	Amp (relative)	t_{peak} Error (days)	FWHM Error (days)	Amp Error (relative)	Source
539.6503088	0.00153389	0.008934698	6.49E-05	0.000213685	0.000716695	*Kepler*
1685.732989	0.005316529	0.011036421	0.000218928	0.000694793	0.000953418	*TESS*

Note. — Flare properties of 414 classical *Kepler* flares and 25 classical *TESS* flares. These are the results of our model fits as described in Section 2.7.2. This table is available in its entirety in machine-readable form in the online journal. A portion is shown here for guidance regarding its form and content.

2.7.2 Updated Flare Properties

We use the flare fits described in Section 2.7.1 of the 414 classical flare events from the *Kepler* data to explore the relationships among the various flare parameters. We include these flare fits in Table 2.2 so future studies may use properties of real flare events as inputs for various simulations. In Figure 2.7, we show the relationship between the fit flare parameters: amplitude, full time width at half of the flux maximum (FWHM), and duration as a function of the event energy. The equivalent duration is computed by integrating the fractional flux under each flare (Gershberg, 1972; Hunt-Walker et al., 2012) and is used to measure the flux event energies. The correlations between flare energy and flare duration are consistent with what we expect: higher energy events occur over longer timescales, while short duration flares typically have lower energies. Similarly, higher energy flares have larger amplitudes. The same trend is true when we consider FWHM as a function of flare energy, however there is a larger scatter in this correlation.

Previous studies have explored the physical interpretation of the correlation between flare energy and duration. For instance, Maehara et al. (2021) carried out time-resolved

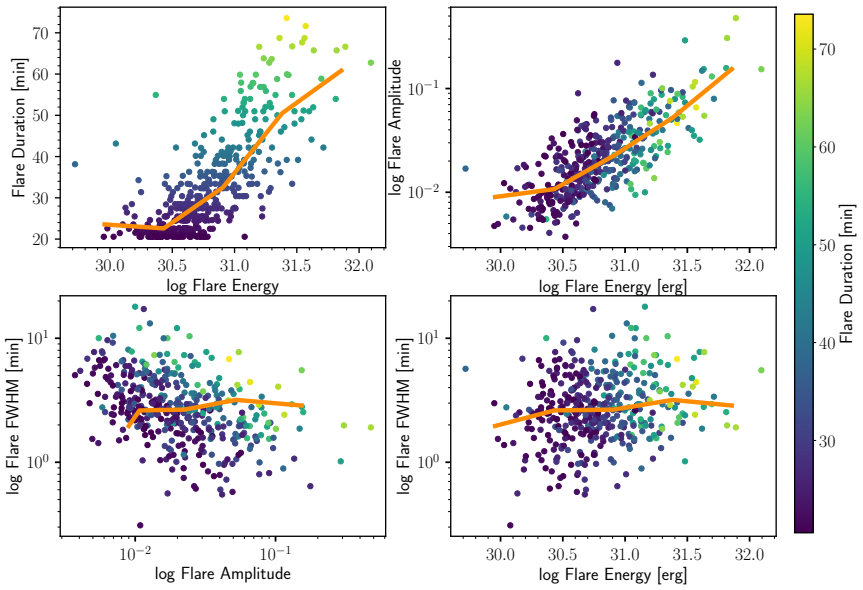

Figure 2.7 **Top:** The top two panels follow the correlation we expect. Flares with higher energies occur over longer timescales and also have higher amplitudes. Meanwhile, lower energy flares occur over shorter timescales and have shorter amplitudes. **Bottom:** There is significant scatter among the FWHM plots which shows that there are flares that are both tall and narrow as well as short and wide. The combination of FWHM and flare amplitudes allow us to characterize the flare profile. The orange lines represent the binned medians for each of the datasets. The color gradient shows flares with different durations (yellow = longer flares and purple = shorter flares).

photometry and spectroscopy of the M-type star YZ CMi and found that the duration of flares showed a positive correlation with the flare energy. Specifically, they find the duration of flares increases with energy as $\tau_{flare} \propto E_{flare}^{0.21\pm0.04}$. However, this is a lower correlation than was found for G-type stars, which suggests a higher coronal magnetic field strength around active M-type stars like YZ CMi and GJ 1243 (Maehara et al., 2021). This timescale versus energy relation is consistent with our FWHM versus energy plot in Figure 2.7, which is expected since GJ 1243 and YZ CMi are of similar mass. We note the timescales are not

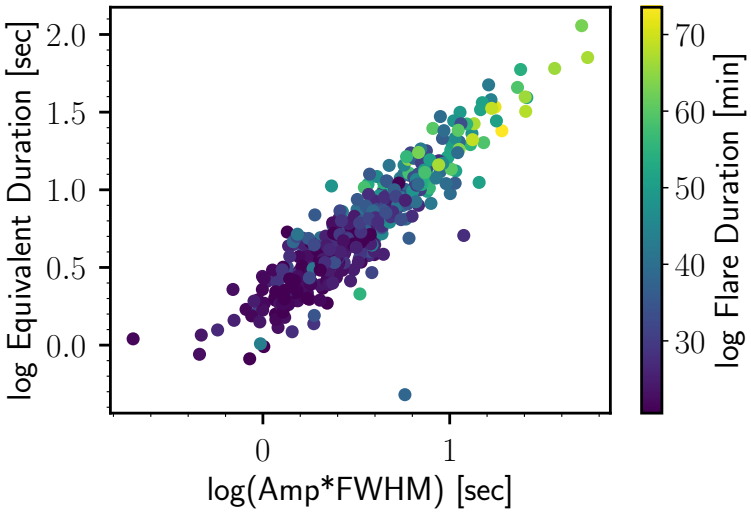

Figure 2.8 Here we show the product of FWHM and amplitude versus the equivalent duration of flare events, both in units of seconds. The data points are color coded by time durations in units of minutes, where lighter colors correspond to longer flare events and darker colors correspond to shorter flare events. The tight correlation between these parameters indicates taht the combination of flare amplitude and FWHM are sufficient to characterize the flare event profile with our model.

exactly the same because we use flare FWHM and Maehara et al. (2021) uses e-folding time.

To further show how these parameters characterize the flare event profile, in Figure 2.8 we consider the correlation between the equivalent duration and the product of the FWHM and amplitude. This product effectively gives an equivalent duration for the impulsive phase of the flare (see Figure 2.5), which D14 showed only encompasses about one third of the total event energy. There is a tight correlation of this product with the flare total energy, which parallels a 1-to-1 trend in Figure 2.8. This demonstrates that while there can be a large scatter in the individual flare properties (e.g. Figure 2.7), the total event can be robustly described by these two impulsive properties (FWHM, Amp), which we use to scale our flare template when fitting actual events.

2.8 Applications

To test our new analytic flare model using a different data set, we turned to the Transiting Exoplanet Survey Satellite (Ricker et al., 2014). *TESS* recently revisited the *Kepler* field, which included GJ 1243 (TIC 273589987) and provided us with 50 days of new short-cadence (2-minute) observations from Sectors 14 and 15 (Davenport et al., 2020). *TESS* has provided the most detailed light curve for this star since the end of the original *Kepler* mission, and has observations that are at longer and redder wavelengths relative to the *Kepler* bandpass. By convolving a 10,000 K blackbody curve with each of the filters, Davenport et al. (2020) showed that within typical uncertainties for distance and flux calibrations, *TESS* and *Kepler* are well suited for comparison since they have similar flare energy yields. They also found that when the flare frequency distributions were modeled for each data set the flare activity remained unchanged from the *TESS* to *Kepler* epochs (Davenport et al., 2020). This provided us with the ideal opportunity to test our new flare model on a data set that had both a different cadence and wavelength coverage for the same star.

2.8.1 GJ 1243 TESS Data

We use the set of 133 flares (classical and complex) from GJ 1243 that were identified using the FBEYE tool by Davenport et al. (2020) in *TESS* sectors 14 and 15. We compared the FBEYE catalog to `stella`, an algorithm that uses a convolutional neural network (CNN) to find flares (Feinstein et al., 2020). To initialize `stella`, we set a flare finding threshold of 0.75, which limits what light curve features get classified as flares versus non-flares. We ensemble the 10 CNN training models provided in Feinstein et al. (2020) and average over the predictions of each of the training models. Ensembling provides a more robust flare classification, which reduces false positives and provides a higher confidence in the true positives. In the end, `stella` successfully recovers 75 flares from the same light curve. We note that GJ 1243 is near the stellar rotation period limit of `stella` (0.59 days), which can be a reason for the discrepancy in the total number of flares that were identified by each

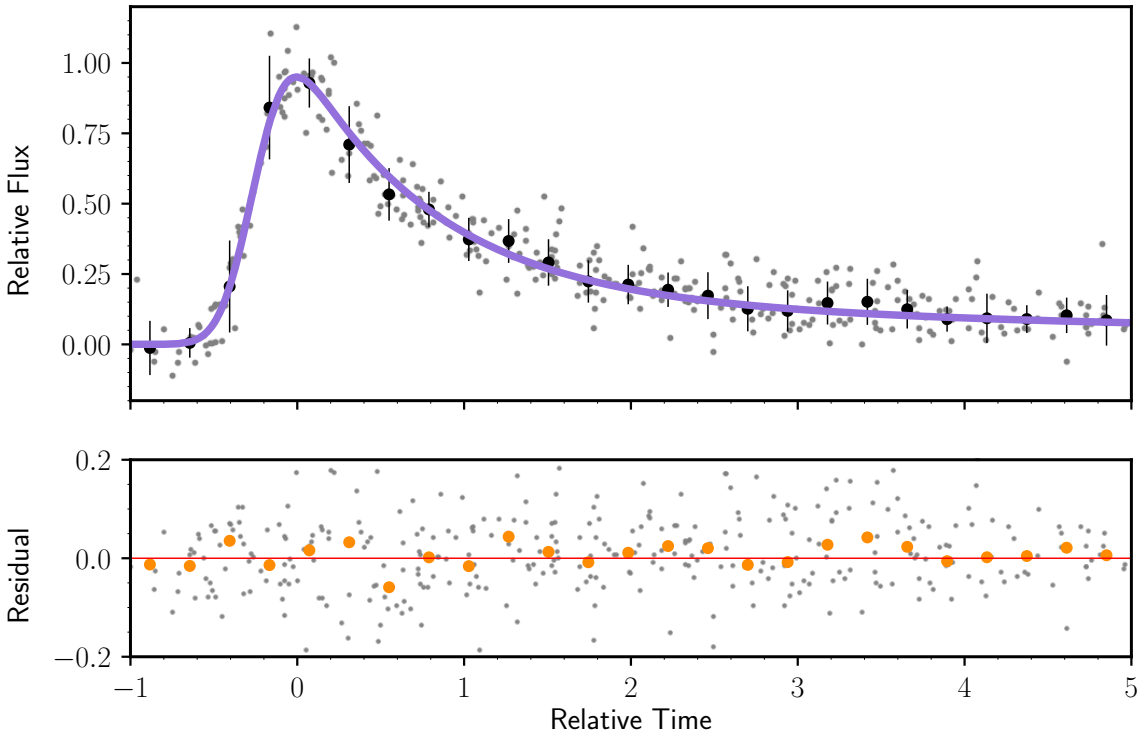

Figure 2.9 We test the GP modeling, stacking procedure and flare identification on *TESS* data. **Top:** Overlay of the updated flare template (purple) onto 25 classical flares from sectors 14 and 15 of GJ 1243 *TESS* data (grey) that are all scaled to a relative time and amplitude. The black points are the binned median of the data with the respective standard deviation of the points inside of each bin. **Bottom:** The residuals of the model (grey) and the binned median of the residuals (orange). The scatter is fairly uniform and the residuals are low suggesting the data is well fit by the model. The flare template can be used to model flares from different datasets and observations at different cadences.

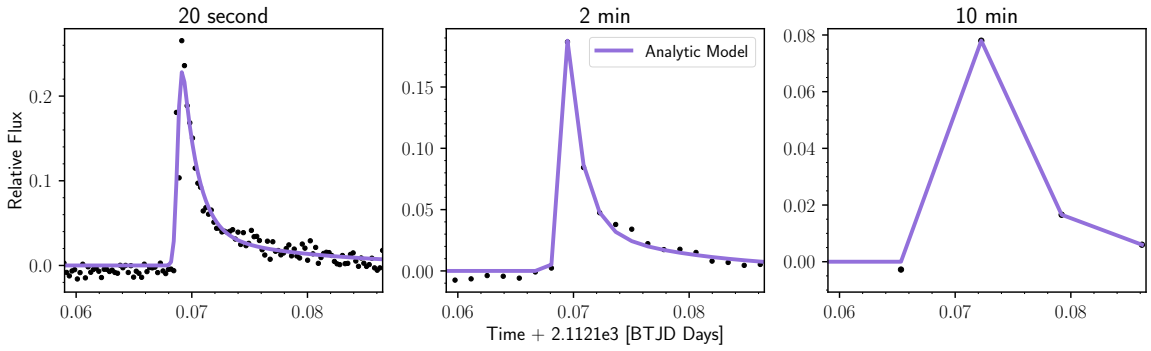

Figure 2.10 We use the new analytic flare template to model one of the flare events occurring on the M3.5 star (TIC 197829751) that was observed by *TESS*. We compare how our model works at different time resolutions. On the far **Left:** we have 20 second data, in the **Center:** we have 2 minute data, and on the **Right:** is the 10 minute data for the same target. Note the increased amount of structure that is revealed in the 20-second flare data vs the 10-minute data. The higher resolution highlights some secondary features in the cooling phase of this particular flare that are not as apparent in the 2-min or 10-min data, hence the different model fits. A table of the best fit values for each cadence mode can be found in Table 2.3.

flare-finding technique. However, `stella` serves as a fast and reliable tool for finding flare events in the *TESS* two minute light curves. Further by-eye analysis is needed to determine which flares are complex versus classical from the `stella` catalog. For this data set, we identified 25 classical flares that were within the 20-75 minute duration range, and we used these flares to test our model.

As in the procedure used for the *Kepler* data, we masked out the flares and used a GP to model the starspot modulations. We used the same initial parameters and rotation period as described in Section 2.4. Once we had modeled the starspot variability, we stacked the classical flares onto a common relative time and flux space using our updated stacking procedure described in Section 2.6. We were then able to overlay our analytical model onto the stack of *TESS* classical flares. In Figure 2.9, we see the results of our analytic flare template from Section 2.7 overlayed onto the 25 stacked *TESS* flares. We also show the binned median of the data. Similar to the case with *Kepler*, we find that the residuals are mostly uniform and flat. Again, we find the photometric errors primarily outweigh the GP errors. Given the small sample of *TESS* classical flares (25) we do not present a *TESS* specific model for this work. Instead, we apply our existing model to the *TESS* data to show its versatility. We find that our flare model can be used to model the morphology of white-light flare events from other data sets with differing observation cadences (e.g. 1-minute versus 2-minute).

2.8.2 Flares at Different Cadences

TESS also provides 20 second observations for a subset of stars. This presented an opportunity to study how flares change across observational cadences. For instance, Shibayama et al. (2013) showed that *Kepler* super flares at 1-minute and 30-minute cadence have similar measured flare energies within the errors. Here we select a low mass flare star (similar to GJ 1243) from *TESS* and use our flare template to model one of the highest signal-to-noise, classical flare events in the light curve. The target (TIC 197829751) is an M3.5 star (Schneider et al., 2019) with a rotation period of about 3.1 days. *TESS* observed the star at 20-second,

2-minute, and 10-minute cadence modes in Sector 29 (see Figure 2.10). In the 20-second cadence data we are able to see the finer structure and complexity of the flare event that is revealed. Meanwhile, the 2-minute data does not show as much detail, especially in the decay phase of the flare event. The 10-minute data shows even less structure of the flare than the 2-minute data. It is interesting to note that the flare event complexity revealed in the 20 second cadence *TESS* data might provide further examples of late phase EUV brightening (e.g. Liu et al., 2015; Chen et al., 2020) and also quasi-periodic pulsations (QPPs) (e.g. Pugh et al., 2016; Howard & MacGregor, 2021).

Higher time resolution observations allow us to both detect smaller flares and understand the complexity of the events. Longer cadence data misses short flares or confuses them for classical events instead of resolving the multi-peak, complex structure. In Figure 2.10, we use our flare template to model the same flare event at three different cadences. We provide the best fit parameters for each of the three cadence modes in Table 2.3. At the 2-minute and 10-minute cadence modes our template is able to describe the morphology of the flare. However, at the 20-second cadence mode it becomes clear that even classical flares reveal complex behavior given high enough time resolution (Howard & MacGregor, 2021). Overall, this example highlights the flexibility of our flare model when used with data taken at various cadences.

2.9 Discussion and Conclusions

We have developed an updated analytic flare template to describe the morphology of white-light flares in precise, space-based photometry. The analytical model is an update to the piece-wise model generated in Davenport et al. (2014). Using a combination of improved *Kepler* light curve processing, an improved flare parameterization from Jackman et al. (2018), and new detrending techniques to account for background starspot variability, we generated an analytic and continuous flare template that can be used to model the white-light flare events on active stars. The flare model shape is described by a function that uses the convolution of a Gaussian and a double exponential, with six coefficients defining the flare

Table 2.3. TIC 197829751 Flare Properties

Cadence	t_{peak}	FWHM	Amp
20 second	0.0692	0.0015	0.2408
2 minute	0.0691	0.0016	0.2363
10 minute	0.0702	0.0011	0.3789

Note. — Best fit coefficients for the example M3.5 *TESS* flare at three different cadence modes (see Figure 2.10).

morphology. We used a total of 414 unique classical flares from 11 months of GJ 1243 *Kepler* data to derive the model. Our updated stacking procedure avoids using the peak flare time or height as parameters as these are sensitive to sampling effects and causes us to systematically underestimate the peak of the flares. Instead we used a center time that leverages the entire flare profile data, which reduced the uncertainty in the stacking procedure. By stacking hundreds of flares together we were able to get fine sampling (e.g less than one second effective resolution) and higher sensitivity to short timescale features (e.g. a smooth turn over at the peak of flares). The final analytic model can be used to fit individual flare events using the following three scaling parameters: amplitude, center time, and FWHM, which is also known as $t_{1/2}$ in previous studies (Kowalski et al., 2013). The model can also be used to model white-light flare events on other stars and with different datasets.

We also studied the morphology of GJ 1243 flares in both the *Kepler* and *TESS* datasets. The data set of 133 flare events detected by *TESS* allowed us to test our updated analytic flare template using a new data set. We see more scatter in the 2-minute *TESS* sample in comparison to the 1-minute *Kepler* data due to cadence and signal-to-noise differences but find our updated flare template is able to model the flares from a different dataset. Our model

can be applied to data from different photometric observations at different cadences, which will prove useful when coupled to other stellar variability and transit modeling algorithms.

In addition to GJ 1243, we analyzed another low mass star (TIC 197829751) that was observed by *TESS* at three different cadences. We were able to use our analytic flare template to model one of the classical flares on the star. We find our model works well at modeling the flares on other active stars. It also can be used to model flares from different datasets and observation cadences. In the 20-second cadence observations, finer flare structure is revealed within a single flare event, whereas in the 10-minute cadence observations the data are more sparse, making it more difficult to see the entirety of the flare shape. However, in all cases our model was able to characterize the underlying flare shape.

Future studies will be able to use the analytical template to model complex (multi-peak) flare events. In the updated flare sample we classified 379 complex flare events that have not yet been modeled with our flare template. Similar to the work in D14, our template can be used as a model to decompose complex flares. This is under the assumption that complex events can be described as the superposition of many classical flares. By linearly adding the models one could use a series of analytic templates to describe the multi-peak flare events. Modeling complex flares will be important especially as we get shorter cadence observations (e.g *TESS* 20 second targets) that are capable of resolving additional complexity present during the flare event. For instance, Howard & MacGregor (2021) sampled 226 flare stars using *TESS* 20 second data and found 49 candidates experienced quasi periodic pulsations (QPPs) and another 17% of the sample showed complex flare morphology. By decomposing the complex flares using the updated model we can compare and model the QPPs and complex structure revealed from new observations.

Beyond flare studies, our analytic flare template will also be a powerful tool for modeling transits in the presence of flares. Currently, many planet detection algorithms account for transits and flares separately (e.g. Luger et al., 2017b) or the flares are simply masked out, which increases the uncertainty in the transit profile. More recent studies have simultaneously modeled the stellar activity within the planet search algorithm (Gilbert et al., 2021),

however, the flare template used in the analysis is from D14, which is improved upon in this work. Our new flare template can be incorporated into existing detection and characterization tools (e.g. Günther & Daylan, 2021; Gilbert et al., 2022). By combining the stellar flare and starspot analysis methods described here with transit models we will be able to both refine existing star-planet parameters and search for transiting exoplanets around active stars that have not yet been detected.

2.10 Acknowledgements

We thank Benjamin Montet, Emily Levesque, and the anonymous reviewer for their insightful suggestions, which greatly improved this manuscript.

The authors acknowledge that this research was conducted on the traditional lands of the Coast Salish peoples, the lands which touch the shared waters of all tribes and bands within the Duwamish, Suquamish, Tulalip and Muckleshoot nations. We honor with gratitude the land itself and the tribes.

GTM acknowledges support from the National Science Foundation Graduate Research Fellowship Program under Grant No. DGE-1762114. Any opinions, findings, and conclusions or recommendations expressed in this material are those of the author(s) and do not necessarily reflect the views of the National Science Foundation.

JRAD acknowledges support from the DIRAC Institute in the Department of Astronomy at the University of Washington. The DIRAC Institute is supported through generous gifts from the Charles and Lisa Simonyi Fund for Arts and Sciences, and the Washington Research Foundation.

This research was supported by the National Aeronautics and Space Administration (NASA) under grant number 80NSSC19K0375 from the TESS Cycle 1 Guest Investigator Program, and grant number 80NSSC18K1660 issued through the NNH17ZDA001N Astrophysics Data Analysis Program (ADAP).

This research has made use of the NASA Exoplanet Archive, which is operated by the California Institute of Technology, under contract with the National Aeronautics and Space

Administration under the Exoplanet Exploration Program.

2.11 De Colores: Kepler + TESS

After this work was published, we explored the multi-wavelength flare properties between the sample of *Kepler* and TESS flares we had detected for GJ 1243. Using 11 months of *Kepler* 1 minute cadence data, (Davenport et al., 2014) identified 6107 flares on the active M star, GJ 1243. From that sample, 5162 flares were classical single-peak events and 945 were complex, multi-peaked events. Furthermore, TESS observed GJ 1243 with a 2 minute cadence and we were able to identify a total of 183 flares using Sectors 14 and 15. Within the TESS sample, 125 flares were complex and 58 were classical flare events. We note that since the time of this work TESS has re-observed GJ 1243 and there now exists 5 more sectors of data (sectors 41, 54, 55, 74, and 75) which will be a rich dataset for future studies.

Figure 2.11 shows the flare properties for GJ 1243. We specifically show the distribution of flare energies as a function of flare amplitudes. In orange we show a total of 183 flares identified with TESS Sectors 14 and 15, and in blue are the 6107 flares identified with 11 months of Kepler data. Since flares are hot, blue, and energetic events their emission is more easily detected at shorter wavelengths. Given *Kepler* observes in the optical and at a shorter cadence we are able to probe smaller (less energetic and lower amplitude) events. Meanwhile, TESS observes in the near infrared and at a longer cadence for this sample of flares, so we probe more energetic (higher amplitude) events. In Figure 2.12 we show a flux calibrated spectrum for GJ 1243 and M4 stellar template with the bandpasses for *Kepler* and TESS overlayed (Davenport et al., 2020). The slight offset in bandpasses allows us to probe a different of part of the stellar spectrum and thus could provide information about the flare temperature. However, the *Kepler* and TESS observations are not contemporaneous making the comparison between the two flare samples more challenging. The multi-bandpass observations of flares motivated our work to explore the flare temperatures of other active stars as I describe in Chapter 3 of this thesis.

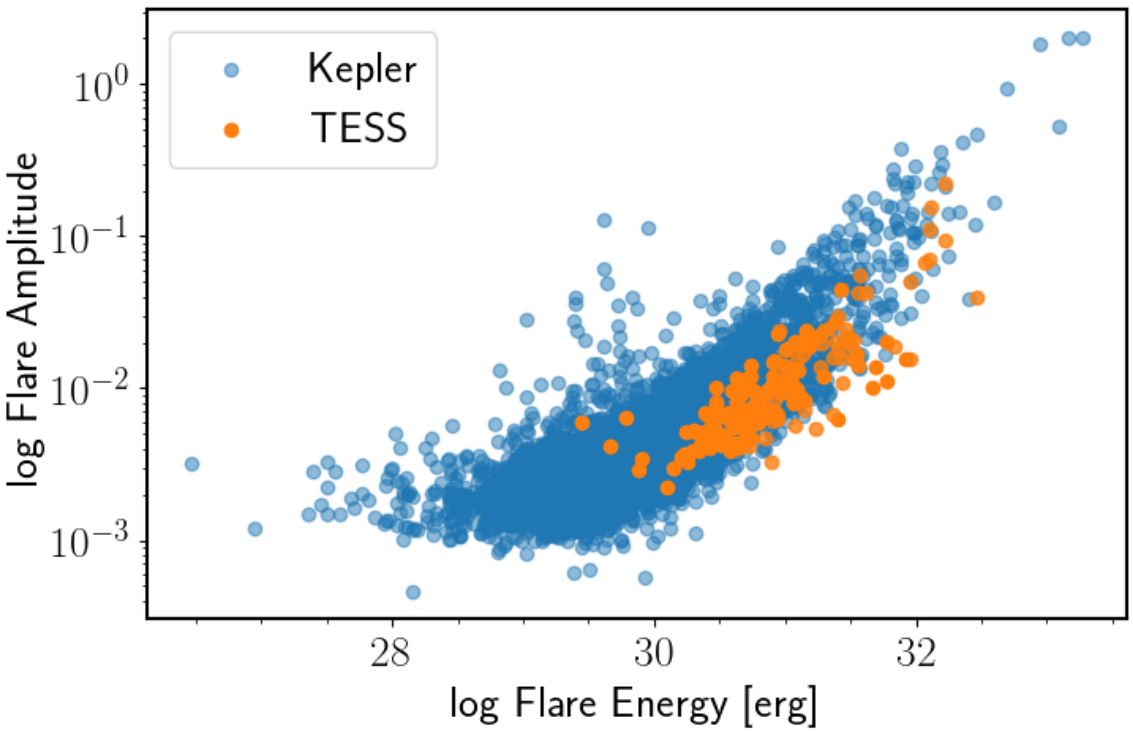

Figure 2.11 Distribution of flare energy as a function of flare amplitude for the sample of GJ 1243 flares. In orange we show a total of 183 flares identified with TESS Sectors 14 and 15, and in blue are the 6107 flares identified with 11 months of *Kepler* data.

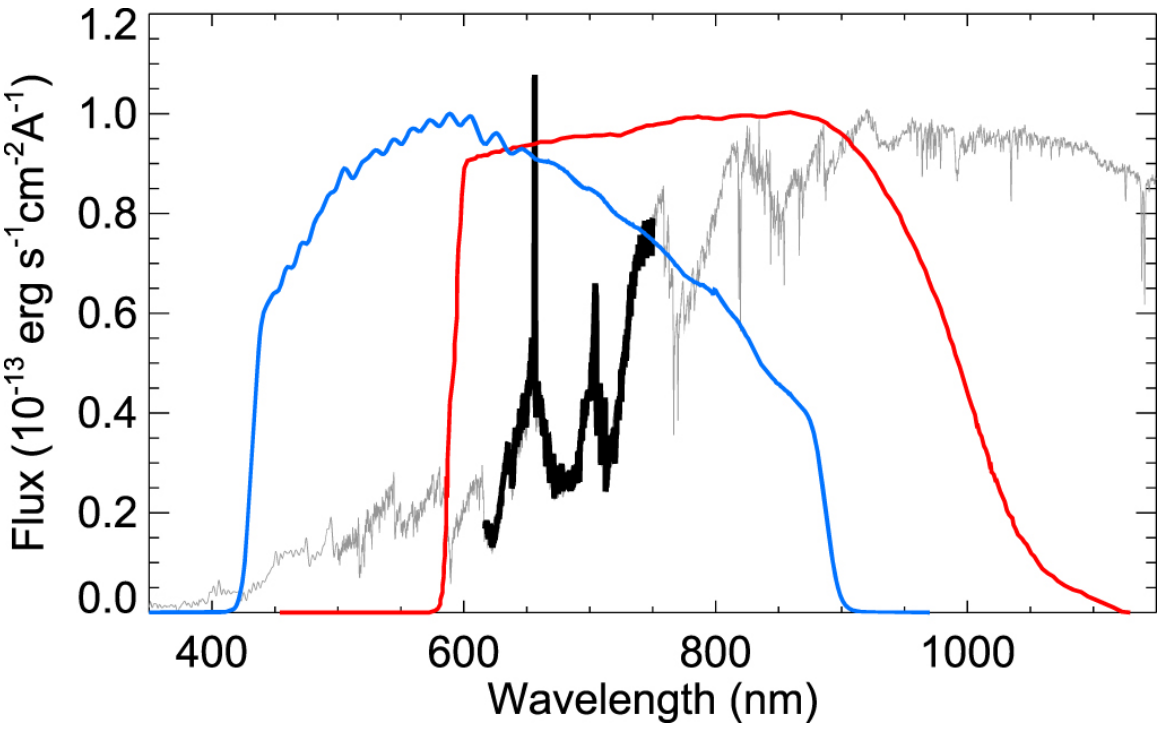

Figure 2.12 Flux-calibrated spectrum for GJ 1243 (thick black line) from (Reid et al., 1995), with the scaled NUV–NIR M4 template (thin gray line) from (Davenport et al., 2012), which is used to calculate the quiescent luminosity for GJ 1243 in the Kepler (blue line) and TESS (red line) bandpasses. Figure from (Davenport et al., 2020).

Chapter 3

REVISITING THE STELLAR FLARES OF TRAPPIST-1 WITH THE SPITZER SPACE TELESCOPE

3.1 Summary

We revisit the archival Spitzer data for TRAPPIST-1 to explore flare temperatures at infrared wavelengths. We analyze 40 days of photometric data at a 2 minute cadence to identify flare events. We present the largest homogeneous sample of flares to date for a single object in the infrared. We find a total of 15 flare events ranging in duration from 7 minutes up to almost 3 hours. We compare the flare occurrence rate to K2 and JWST results. Using a spectral energy distribution for TRAPPIST-1 we convert all the flare energies to TESS energies and explore a grid of blackbody effective temperatures [3000-15000 K] to determine which flare temperatures result in the same flare frequency distribution (FFD) across the ensemble of bandpasses. An effective flare temperature of at least 5480 $\pm$ 83 K is needed to reproduce the FFD. We find the TRAPPIST-1 flare temperatures in the infrared are cooler than those in the optical, in broad agreement with recent studies of flares from JWST for TRAPPIST-1.

3.2 Introduction

Low mass stars, especially M dwarfs, are known to be highly magnetically active on all timescales (Lacy et al., 1976; Kochukhov, 2021). The turbulent stellar dynamo and rotation fuel their levels of magnetic activity. Star spots, faculae, plage, and flares are some of the manifestations of magnetic activity we detect on these stars (Berdyugina, 2005; Benz, 2008). M dwarfs are also some of the most abundant stars in our universe, comprising almost 70% of the stellar population (Henry et al., 2006). Despite the presence of stellar activity, low-mass stars are still the most favorable targets for transmission spectroscopy because

the strength of the planetary atmospheric features scales inversely with the square of the star size. Planets transiting smaller stars thus produce stronger features and can be better characterized (Kempton et al., 2018).

Located about 12 parsecs away, TRAPPIST-1 (T-1) is an M8V star (Gillon et al., 2017b) with a rotation period of 3.3 days (Luger et al., 2017b; Roettenbacher & Kane, 2017). Its fast rotation drives the stellar magnetic activity we see on the surface of the star. Recent studies with JWST have determined that TRAPPIST-1 emits flares ($> 10^{30}$ erg) at a rate of 3.6 flares per day (Howard et al., 2023); these energetic flares affect studies of the TRAPPIST-1 planets.

TRAPPIST-1 hosts seven known planets (Gillon et al., 2017b; Delrez et al., 2018). Three of the planets (d, e, and f) are in the habitable zone – the distance from a star where liquid water can be sustained (Kopparapu, 2013). These planets are prime targets for atmospheric characterization and have been followed up with JWST transit observations (Mandt et al., 2022). Exoplanet transmission spectroscopy has proven to be a powerful tool to identify the presence of molecules, gases, and clouds in the atmospheres of transiting exoplanets (e.g. Seager & Sasselov, 2000; Sing et al., 2016). During a transit, starlight filters through the planet's atmosphere and comparisons of spectra during and outside of transit are used to reveal the planet's atmospheric makeup. The key to exoplanet transmission spectroscopy is that transit depths—the observed decreases in flux due to a planet blocking a small fraction of a star's light—are wavelength dependent. For a given wavelength, some atoms and molecules in the planet's atmosphere absorb incident light, while others allow light to pass through. Greater absorption causes the disk of the planet to appear more opaque and larger, leading to deeper observed transits. Transit depth as a function of wavelength yields a transmission spectrum, a unique spectral fingerprint which can then be compared to models to infer the planet's atmospheric constituents. For instance, thermal emission measurements using JWST MIRI have revealed TRAPPIST-1c has no atmosphere (Zieba et al., 2023), and upcoming general observing programs will improve our understanding of the compositions of the other 6 planets in this system.

Transmission spectroscopy requires that we have a precise understanding of the wavelength-dependent flux of the star that is being occulted. Transmission spectroscopy assumes that part of the spectrum of the stellar atmosphere, underneath the transit chord, is the same as the disk-averaged stellar spectrum. However, stars are magnetically active, and as a star rotates, we see different features come into and out of view (e.g. spots, faculae, and flaring active regions). Therefore, unocculted spots or faculae can leave behind their spectral signatures (the transit light source effect) (Rackham et al., 2018). These brightness variations (from spots or flares) can dilute or enhance the measured transit depths, leading to errors in the observed spectrum, also known as stellar spectral contamination (e.g. Sing et al., 2011; McCullough et al., 2014; Rackham et al., 2018). For instance, spots can change the spectrum of the star by a few percent on order of days timescale (Lim et al., 2023), and flares can create many percent changes on order of minutes to hours timescale even if they are not near the transit chord (Howard et al., 2023). Stellar contamination can introduce positive or negative features in an observed spectrum that can mimic or suppress features in the intrinsic planetary spectrum. Stellar activity continues to contaminate the atmospheric spectrum and future work is needed to disentangle the two signals (Lim et al., 2023; Howard et al., 2023).

Since its discovery in 2016, the TRAPPIST-1 exoplanet system has been observed by dozens of ground and space based telescopes (Luger et al., 2017b; Gillon et al., 2017b; Delrez et al., 2018; Grimm et al., 2018; Burdanov et al., 2019). In particular, the Spitzer space telescope (Werner, 2005) has over 1000 hours of observations of TRAPPIST-1 and its planets spanning from from February 2016 to October 2019 through the Spitzer Exploration Program Red Worlds (Delrez et al., 2018). The goals of the program were to constrain the dynamical properties, masses, and orbital parameters of the planets using transit timing variations (TTVs)(Agol et al., 2020). Furthermore, the Spitzer observations provided an infrared analysis of the stellar variability. Here we use all of the 41 days of Spitzer data for our analysis.

The physics and impacts of stellar activity at infrared wavelengths remains an active

area of research. We know flares, which are explosive magnetic events that occur on the surfaces of stars, have peak energies at near-ultraviolet and blue wavelengths (Kowalski et al., 2010). However, the energy released during these events is detected across the entire electromagnetic spectrum (Osten & Wolk, 2015; Macgregor et al., 2021). Historically, flares have been modeled as having a 9,000 - 10,000 K blackbody spectrum. However, recent studies are showing flare temperatures outside of this regime. Some studies show flares that are much hotter at UV and optical wavelengths (Howard et al., 2020; Jackman et al., 2022) and others that are significantly cooler (Maas et al., 2022), especially in the infrared (Howard et al., 2023). Our understanding of flares in the IR is crucial especially in the era of JWST and exoplanet characterization (Davenport, 2017).

As more observations continue to be collected our understanding of the TRAPPIST-1 system grows. However, the impact that stellar activity has on the seven exoplanets is still an open question and very active area of research. In this work, we revisit the archival Spitzer infrared data to identify a comprehensive list of stellar flares. Our primary goal is to quantify the infrared flare rate of TRAPPIST-1 and place it into the context of existing work. We compare our flare frequency distributions to the findings from K2 and JWST. Furthermore, we provide a discussion on infrared flare temperatures and their implications for habitability.

3.3 Methods

3.3.1 Detrending the Spitzer data

The Spitzer archival data provides a rich database for an analysis of T-1 [1]. The data were collected as part of the Spitzer Exploration Science program Red Worlds (ID 13067), DDT program 12126, DDT program 13175, and DDT program 14223 (Gillon et al., 2017a; Delrez et al., 2018; Ducrot et al., 2020; Agol et al., 2020) all of which sought to characterize the T-1 system. With over 1000 hours of observations of the T-1 system, we are able to detect both

[1] `https://irsa.ipac.caltech.edu/applications/Spitzer/SHA/?__action=layout.showDropDown&`

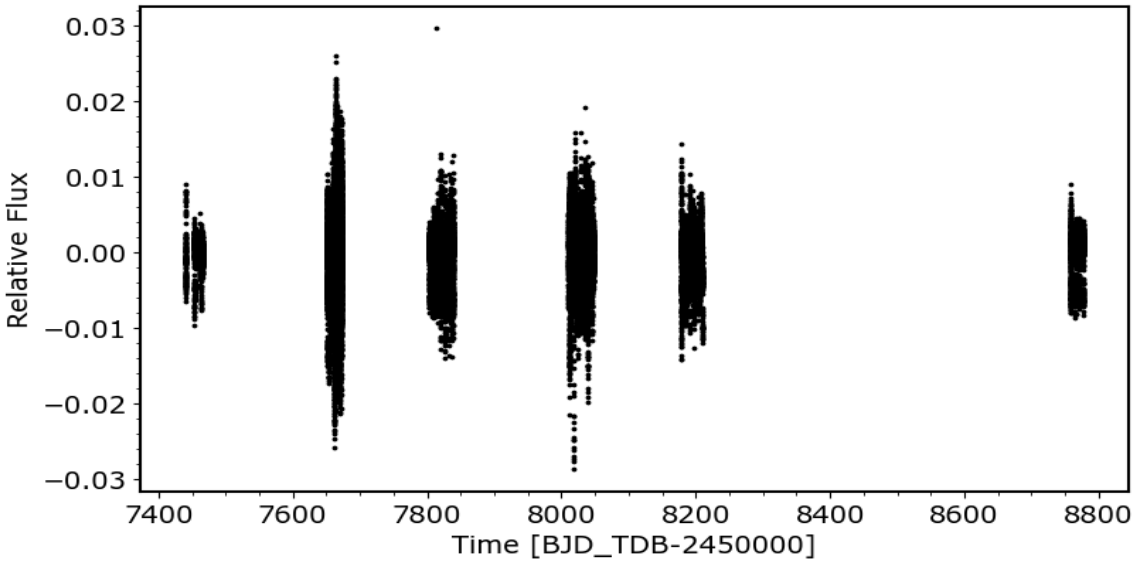

Figure 3.1 Raw Spitzer light curve of over 1000 hours ($\approx$ 40 days) of TRAPPIST-1 observations from Feb. 2017 - Oct 2019. Photometric measurements were taken using both the 3.6 μm and 4.5 μm bandpasses. These data were collected as part of the Spitzer Exploration Science program Red Worlds (ID 13067), DDT program 12126, DDT program 13175, and DDT program 14223 (Gillon et al., 2017a; Delrez et al., 2018; Ducrot et al., 2020; Agol et al., 2020). The data is available on the Spitzer Heritage Archive database.

planetary transits and stellar flares in the data. Initially there was a 20-day long (480 h) near-continuous monitoring of the system at 4.5 µm, followed by high-precision monitoring of the known planetary eclipses at 3.6 and 4.5 µm from 2017 to 2018 (520 h) (Ducrot et al., 2020). For all observations in both bandpasses, each frame is composed of 64 sub-exposures each of 1.92 s on the target plus an additional 0.8 s for read out, which gives a cadence of 2.06 min (Ducrot et al., 2020). Figure 3.1 shows the light curve of all of the Spitzer data used for our analysis in this work.

There are known telescope pointing deviations in the data that need to be addressed to perform our analysis (Ducrot et al., 2020). To detrend the data we first accounted for the telescope pointing flux variations at each visit. To do this we used a linear regression model (Gould, 2003). We use three components in our linear regression model as follows:

$$model = c_1 + c_2 * dx + c_3 * dy \tag{3.1}$$

where dx and dy are vectors that represent the changes in x and y pixel position at each time for a given exposure. We use `scipy.linalg` to perform a linear regression between dx, dy, and the observed flux. The astrophysical flux does not correlate with the x- & y-positions, so this is evidence that the measured flux is affected by the variation in pointing of the telescope. We subtract off these linear pointing-dependent flux variations, and are left with the resulting astrophysical component. We perform this detrending for each of the observation windows.

Transit Model

Transit models have been developed to analyze and understand the planetary properties such as mass, radius, and density. One analysis method that has been widely used to characterize planetary systems like T-1 is TTVs. As the name suggests, TTVs are the deviations in time and duration that occur when you have multi-planet systems that have non-Keplerian orbits (Agol & Fabrycky, 2018), and thus we can detect the gravitational interactions between

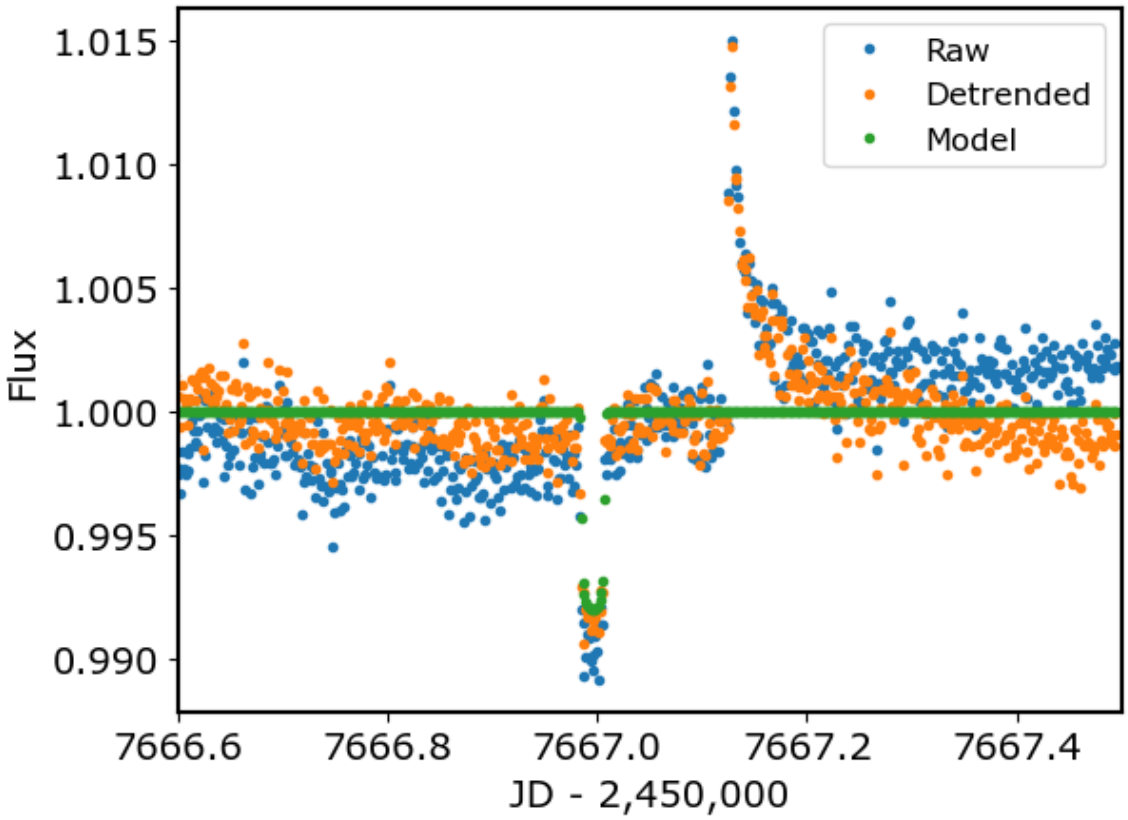

Figure 3.2 A zoom in of two days of photometric observations of TRAPPIST-1 where we can see both an exoplanet transit and a flare occurring. The raw data is in blue. The detrended data is in orange. In green we show the transit model. By detrending the raw data we are able to improve the point-to-point scatter by a factor of 1.4.

the planets. The information encoded within TTV data has led to the detection of many new worlds, including longer period, non-transiting systems (Holman et al., 2010) as well as refined exoplanet characteristics, such as masses (Agol Eric et al., 2005; Agol et al., 2021).

To further detrend the light curve and aid in our flare identification process we used a transit model to remove the known transits from the light curve. Within the Spitzer data 188 exoplanet transits were identified by (Ducrot et al., 2020). Figure 3.2 shows a zoom in of two days of data where we can see both a flare and transit occurring within the same time window. The photometric transit model we use for this analysis is based on the analysis described in (Agol et al., 2020). In that work the authors fit a photo-dynamical model to the Spitzer data, which uses an N-body TTV model to estimate both the stellar density and planet-to-star ratios. The quadratic limb darkening of the star is accounted for in each of the Spitzer bands, see Agol et al. (2020) and references therein, for the details of each of the 19 parameters which are fit. Finally, we divide the transit model out of the data to remove the transits, and we are left with only the stellar signals. In Figure 3.2 we show our detrending which accounts for both telescope pointing flux variations and we also show the transit model that is later subtracted off.

3.3.2 Identifying Flares

Once the data was detrended and the transits were removed, we began the flare identification process. The entire 40 days of Spitzer data were manually inspected to identify flares. Events of excess flux or with the highest amplitudes that deviated by at least 3 sigma amount above the noise were flagged as potential flare events (Ducrot et al., 2020). The light curves were then manually inspected by three different people, each identifying start and stop times for the flare events, as well as a time of peak amplitude. For each flare, the maximum duration (start and stop times) were then used in our analysis. This broadly follows the manual inspection procedure outlined by Davenport et al. (2014). A total of 15 flares were identified from the data, which is three times the number of flares previously published from Spitzer data Ducrot et al. (2020). We note that previous work by Ducrot et al. (2020) only identified

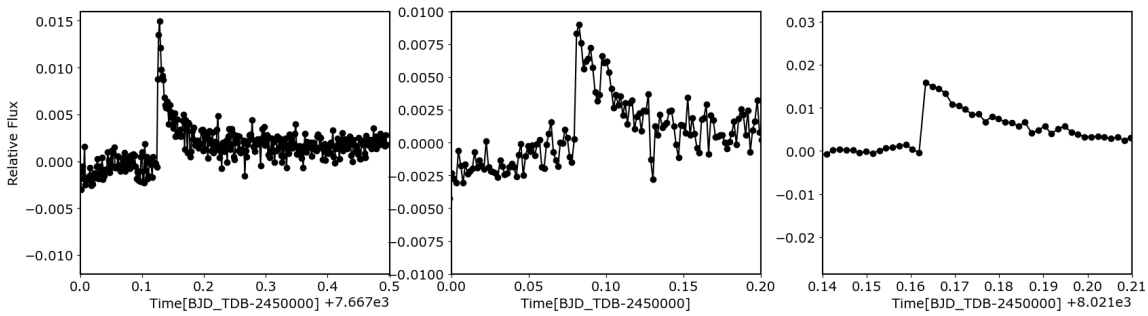

Figure 3.3 A zoom in of the three largest T-1 flare events that were identified in the Spitzer data. From left to right the flares have durations of 158, 64, and 82 minutes. The first two flares were observed with the 4.5 μm bandpass, and the rightmost flare was observed at 3.6 μm. We note starspot modulations have not been subtracted, we only do spatial detrending.

the 5 largest flares in the data. We find flares ranging from 7-158 minutes in duration. Our sample has both classical (single-peaked) and complex (multi-peaked) events. The properties of the flare events are listed in Table 3.1. A zoom in of three of the longest duration flare events are shown in Figure 3.3.

3.3.3 Flare Properties

We use the flare template from Tovar Mendoza et al. (2022) to fit our sample of 15 flares. The flare template can be used to model the morphology of stellar flares. This model improves upon previous studies (e.g. Davenport et al. (2014)) by using an updated parameterization that ensures the model is continuous at the flare peak, and more accurately represents the heating and two-phase cooling processes that occur during flare events (Jackman et al., 2018). The result is a continuous and analytic model that allows us to parameterize classical, single-peaked flare events and later decompose complex (multi-peak) flare events into a series of classical events as seen in Davenport et al. (2014). This flare model has been adopted to model flares in both *Kepler* and *TESS* data (Barclay et al., 2023). Here we apply it to the Spitzer infrared data. To model the flares the template relies on three parameters: amplitude,

peak time, and the full width at half of the maximum (FWHM). We use `scipy.curvefit` to fit the flare template to each of the flares.

Table 3.3.3 provides the flare properties for all 15 of the T-1 flares in the Spitzer data. We include the start and stop times of the flares in days, flare amplitude, duration, and the channel with which the flare was observed. We use these properties to compute the equivalent durations for each of the flares. The equivalent duration is computed by integrating the fractional flux under each flare (Gershberg, 1972; Hunt-Walker et al., 2012) and is used to measure the flux event energies. In other words, equivalent durations tell us how long it would take a star (T-1 in this case) in quiescent state to release the same amount of energy released during the flare (time integral).

3.3.4 Flare Frequency Distributions

Flare frequency distribution (FFD) diagrams are used to compare the frequency of flares per day on a star a function of flare energy (e.g. Lacy et al., 1976; Shibayama et al., 2013). We can model FFDs using a power law distribution. For solar-type stars, this power law distribution has been shown to have a fixed slope over 10 orders of magnitude in flare energy (Shibayama et al., 2013; Maehara et al., 2015). FFDs are mathematically described as:

$$\log(\nu) = \alpha \log(\epsilon) + \beta \tag{3.2}$$

where ν is the cumulative rate of flares observed, ϵ is the flare energy, and α and β are the linear coefficients of the power law fit. FFDs typically show many low energy flare events, where the lower limit is set by the detection threshold. Meanwhile, high energy flares are rare and we are Poisson limited at the high energy regime.

Recently, Scoggins et al. (2019) showed that stars with significant differences in the power law would indicate changes in flare activity levels. A star whose flare activity level changed over a few years timescale may be undergoing activity cycles.

Table 3.1. TRAPPIST-1 Spitzer Flare Properties

t_{start} (days)	t_{stop} (days)	Amp (relative)	Duration (min)	Channel (microns)
7655.968	7655.98	0.00692	17.28	4.5
7659.375	7659.42	0.01051	64.8	4.5
7667.12	7667.23	0.01569	158.4	4.5
7807.813	7807.827	0.0027	20.16	3.6
7809.5458	7809.5548	0.00416	12.96	3.6
8021.16	8021.217	0.016	82.08	3.6
8046.812	8046.82	0.007	11.52	3.6
8184.9649	8184.9721	0.007	10.368	3.6
8186.9834	8186.9942	0.002	15.552	3.6
8201.03	8201.039	0.003	12.96	3.6
8208.77	8208.78	0.005	14.4	3.6
8757.66	8757.676	0.007	23.04	4.5
8758.209	8758.214	0.0064	7.2	4.5
8769.9525	8769.9576	0.004	7.344	4.5
8777.038	8777.0485	0.009	15.12	4.5
8777.1607	8777.166	0.004	7.632	4.5

Note. — Flare properties of the 15 identified Spitzer flares.

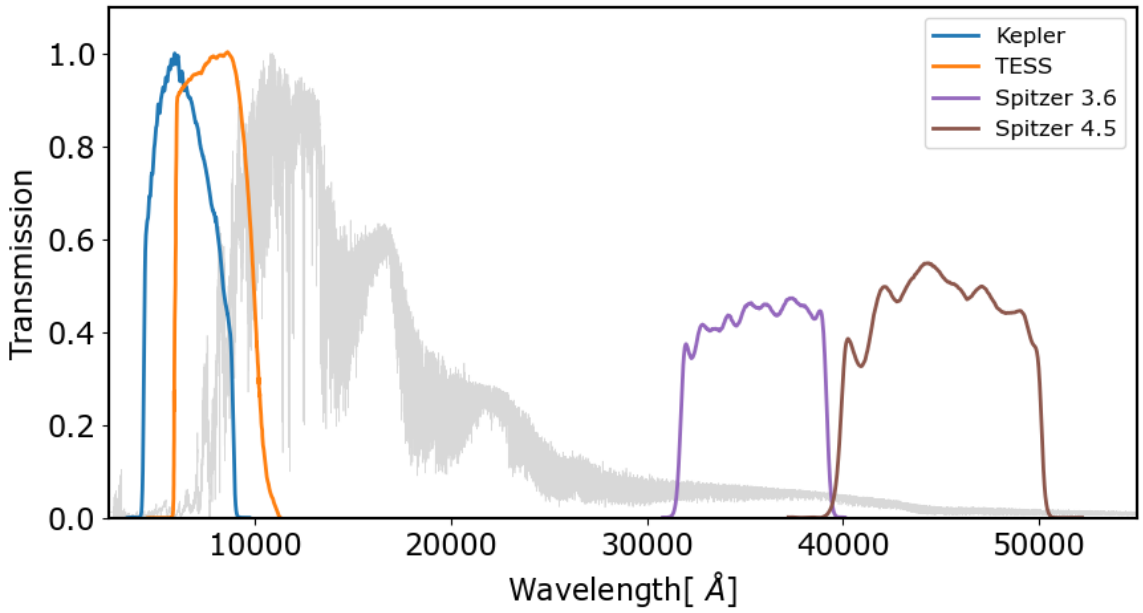

Figure 3.4 Filter curves for each of the datasets considered in this work. The Kepler (blue) bandpass covers wavelength ranges from 4000-8650 angstroms, and TESS (orange) covers 6000-10000 Angstroms. Meanwhile, the Spitzer Infrared Array Camera (IRAC) (Fazio et al., 2004) provides simultaneous 5.2' × 5.2' images at 36000, 45000, 58000, and 80000 Angstroms, for this work we only consider the first two channels. In gray is the Mega-MUSCLES T-1 spectrum from (Wilson et al., 2021).

3.3.5 K2 Data

The *Kepler*/K2 mission provided us with observations of over 500,000 stars. The T-1 system was also observed by K2 (Vida et al., 2017; Davenport, 2017). From these observations several teams were able to analyze the optical flares of T-1. For instance, (Vida et al., 2017) found 42 flares ranging in energy from $10^{30} - 10^{33} erg$. Furthermore, (Davenport, 2017) reported comparison of flare rates of T-1 in the optical with K2 and Spitzer in the infrared. At the time, only 4 flare events had been identified in the Spitzer data. In Figure 3.4 we show the filter curves for each of the datasets we consider in this work.

Figure 3.5 shows the FFD as a function of equivalent duration of the 35 flares identified with K2 and the 15 flare identified with Spitzer. The offset is due to the difference in bandpasses, with K2 covering optical wavelengths from 4000-8650 Angstroms and Spitzer observations at 36000 and 45000 Angstroms. Since flares are hot, blue, energetic events, we expect to detect peak flare emission at shorter wavelengths. The impacts of infrared flares on transit studies has been explored for mid-M type stars by (Tofflemire et al., 2012). Similarly, (Davenport et al., 2012) showed the infrared flare flux contrast is stronger for later spectral types. This was determined by using flare rates from M0-M6 stars and converting the peak flare fluxes between optical and infrared bandpasses. Following this trend we expect the flux contrast of T-1 flares to also be higher than it would be at optical wavelengths.

3.3.6 Luminosity Calibrations

Many of the fundamental parameters of T-1 have been determined using a distance-calibrated spectral energy distribution (SED) (Filippazzo et al., 2015). Here we use the SED from (Gonzales et al., 2019) for our luminosity calculations. The SED was created by using spectra, photometry, and a parallax, which helped determine a bolometric luminosity. Specifically, the SED includes photometry from Pan-STARRS (Chambers et al., 2016), Gaia (Moitinho et al., 2017; Collaboration et al., 2018), 2MASS (Cutri et al., 2003), and WISE (Cutri & et al., 2012). We also use filter curves from *Kepler* (Borucki et al., 2010), *TESS* (Ricker

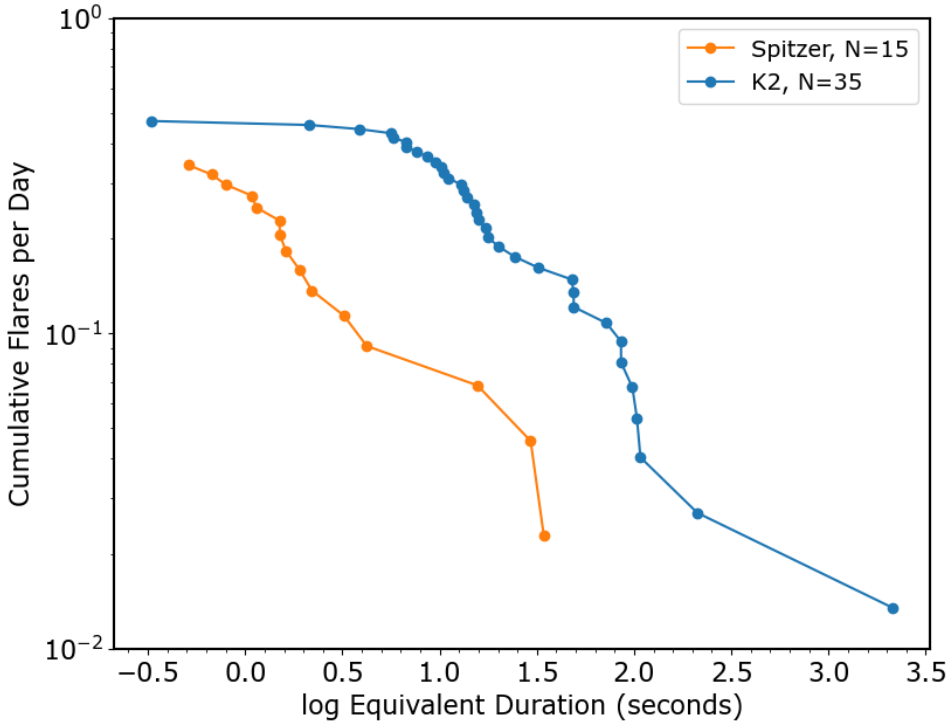

Figure 3.5 Flare Frequency Distribution (FFD) of T-1 flares showing the cumulative number of flares observed per day as a function of their log equivalent durations. In orange are the 15 flares observed by Spitzer and in blue are the 35 flares that were observed by K2 (Davenport, 2017). The offset is due to the differences in bandpasses with K2 observing at optical wavelengths and Spitzer observing in the infrared.

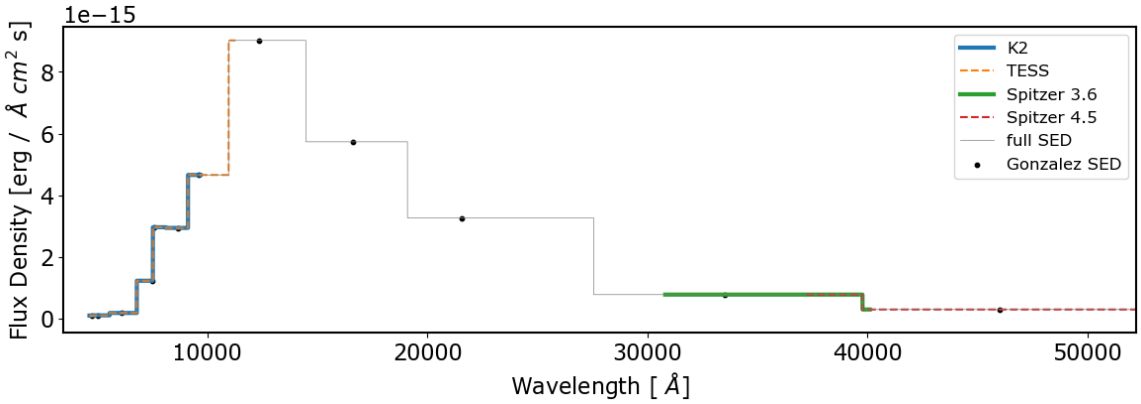

Figure 3.6 A reconstructed distance-calibrated SED of TRAPPIST-1 from (Gonzales et al., 2019). We include photometry from K2 and TESS. The solid lines represent the flux-conserved interpolation over the various bandpass ranges.

et al., 2014), and Spitzer (Werner, 2005). Using the published SED and the filter curves we convolve the SED into these bands. We also use `specutils.FluxConservingResampler`, which conserves the overall integrated flux to interpolate over the entire SED. The results of our interpolation and the reconstructed SED are shown in Figure 3.6.

We then calculate the quiescent luminosities for T-1 at each of the bands. We use the distance calibrated SED and convolve it with the response function of each band. We assume the distance of TRAPPIST-1 to be 12.43pc (Chambers et al., 2016). We find the following log luminosities for T-1 at the various bandpasses: $L_{Kepler} = 32.02$, $L_{TESS} = 32.38$, $L_{Spitzer,3.6} = 32.56$, $L_{Spitzer,4.5} = 32.55$. We note there is an error associated with the luminosities.

Next, we convert all of our luminosities to the TESS bandpass for ease of comparison to previous work. To do this we calculate bolometric energy correction factors. We start by assuming a blackbody temperature and calculate the fraction of blackbody flux that is measured at each bandpass. Using these correction factors we can now calculate the energy in each bandpass using the following:

$$E_\lambda = log(ED) + log(L_\lambda) - C_\lambda \tag{3.3}$$

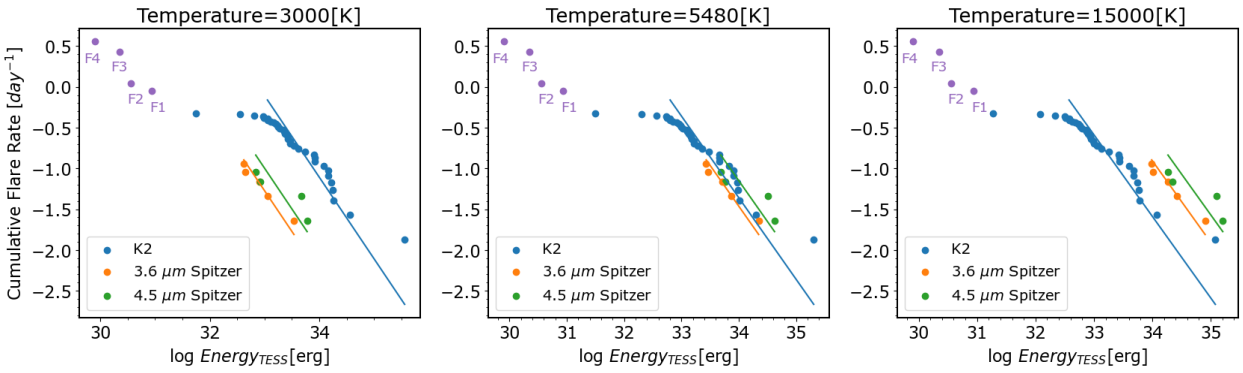

Figure 3.7 Flare Frequency Distributions (FFD) of T-1 flares from K2 and Spitzer, converted to TESS flare energies assuming a fixed blackbody flare temperature. We treat the two Spitzer bandpasses independently. Each panel assumes a different blackbody temperature for the flares. JWST T-1 flares from Howard et al. (2023) are shown for qualitative comparison, but were not used in our analysis (purple points). Straight lines indicate the power law fits assuming a slope of $\alpha = -1$. The middle panel highlights the scenario where the FFDs from K2 and the two Spitzer bands most closely align. In other words, a mean flare temperature of $\approx$ 5480 K produces a consistent flare rate across all bandpasses in our sample.

where ED is the flare equivalent duration, L is the luminosity at a given bandpass, and C is the correction factor at a given bandpass. We are then able to vary the assumed initial blackbody temperatures and measure which temperature gets the FFDs to align. Our flare temperature analysis is discussed in detail in Section 3.4.

3.4 Flare Temperature Analysis

In this ensemble analysis of the T-1 flares we explore what effective flare temperature allows for the optical and infrared flares to align. Figure 3.7 shows the flare frequency distributions of T-1 flares across various bandpasses including: K2, Spitzer 3.6 μ m, Spitzer 4.5μ m, and JWST. We converted all of the flares into TESS energies for ease of comparison to previous studies. The JWST flares were identified and measured in Howard et al. (2023).

Given a blackbody temperature we calculate the correction factor. Specifically, we ran a grid of temperatures from 3000 - 15000 K in steps of 1 Kelvin to determine which temperature would get the FFDs to align (e.g. produce the same flare rate). Next, we fit a slope of -1 to the FFDs as determined by (Ilin et al., 2021a) and calculated the y-intercepts for each of the FFDs with respective uncertainties. The uncertainties are propagated into the covariance. We find that a temperature of 5480 K allows for the FFDs to align. In other words, a mean flare temperature of 5480 K is needed to reproduce the observed flare rates. We note this is an ensemble flare temperature analysis and discrepancies are due to the following: the flare SED is not a single blackbody, all flares are not the same temperature, and there has been suggestions of a cooler flare temperature component present in the infrared (Kowalski et al., 2016a). To quantify our results we perform a chi squared analysis described in the Section 3.4.1.

3.4.1 Chi Squared Analysis

We perform a χ^2 analysis to quantify our temperature results. We can calculate the reduced χ^2 using the following standard equation:

$$\chi^2 = \frac{1}{N}\Sigma(\frac{O_i - E_i}{E_i})^2 \tag{3.4}$$

where N is the number of degrees of freedom in the model (here $N = 3$ for our FFD samples), O is the observed values (i.e. the FFD intercepts of the three bandpasses), and E is the expected value (i.e. the mean FFD intercept evaluated at each temperature). This statistical test allows us to compare how our expected values compare to the actual observations, in effect minimizing the scatter in our optical and infrared FFDs to find the ensemble flare temperature that best describes our sample. Figure 3.8 shows the results of this analysis. We find the minimum value of $\chi^2 = 3.68$ happens at a temperature of $T_{eff} = 5480$ K. To estimate the uncertainty in this temperature, we follow the standard procedure of finding the values in Figure 3.8 where the χ^2 increases by 1. This gives us an temperature uncertainty

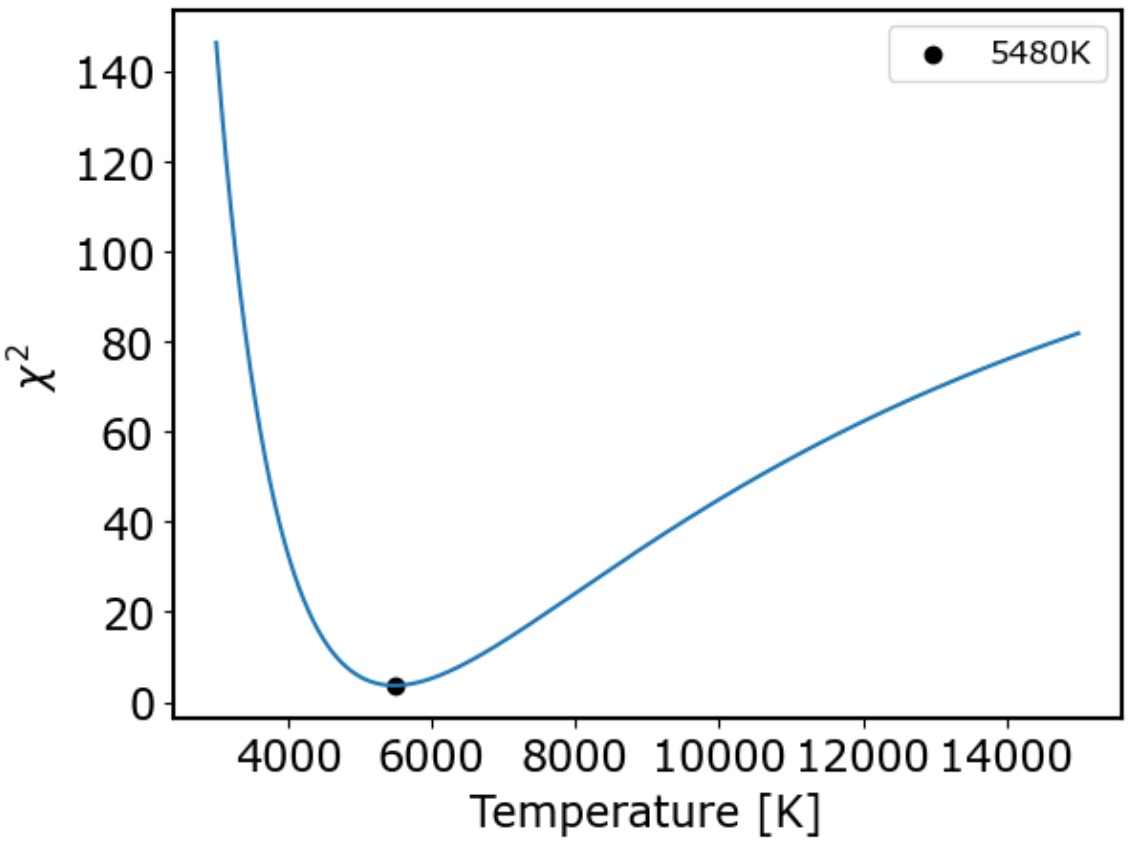

Figure 3.8 χ^2 results after performing a grid search in steps of 1°K in temperature. We find the minimum value of $\chi^2 = 3.68$ happens at a temperature of $T_{eff} = 5480$ K $\pm$ 83 K.

of 83 K.

3.5 Results & Discussion

In this work, we use archival Spitzer data to study the infrared flares of TRAPPIST-1. We analyze a total of 40 days of photometric Spitzer data at a cadence of 2 minutes and at two different bandpasses (3.6 and 4.5 microns). We present the largest homogeneous sample of flares to date for a single object in the infrared. We find a total of 15 flare events ranging in duration from 7 minutes up to almost 3 hours, tripling the previous number of identified flares (5) in the Spitzer data for T-1. Using a SED for TRAPPIST-1 we convert all the flare energies to TESS energies and explore a grid of blackbody effective temperatures [3000-15000 K] to determine which flare temperatures result in the same flare frequency distribution (FFD) across the ensemble of bandpasses. An effective flare temperature of at least 5480 $\pm$ 83 K is needed to reproduce the FFD. We also compare the flare occurrence rate to K2 and JWST results. Below we provide a discussion of infrared flare temperatures, comparisons to JWST, and future directions of this work.

3.5.1 Infrared Flare Temperatures

The temperatures we find in this analysis suggest infrared flares are significantly cooler than typically assumed for optical flares. Recent work by (Maas et al., 2022) used T-1 optical observations from MuSCAT2, and found the blackbody flare temperatures derived from their SED to be 7940 K and 6030 K. Furthermore, the peak flare temperatures for each was determined to be 13620 K and 8290 K respectively. In comparison, the flare temperature we derived from our SED was 5480 K which is over 1000 K cooler than those detected in the optical. Our results are consistent with recent work by (Howard et al., 2023), which finds JWST flare temperatures of T-1 to be well described by blackbody emission with an effective temperature of 5300 K.

Furthermore, our results suggest that the canonical 10,000 K blackbody assumption does not hold true at infrared wavelengths. Whereas a 10,000 K blackbody temperature can

explain flares in the UV and optical our results suggest a cooler component (e.g. excess cool emission) must be dominant at infrared wavelengths. A physical explanation for this could be due to varying filling factors (Kowalski et al., 2013). Our cooler temperatures in the IR are consistent with work by (Kowalski et al., 2016b) which also observed a cooler blackbody component at longer wavelengths.

3.5.2 Comparison to JWST

JWST is probing infrared (IR) wavelengths where the flux contrast between a planet and its star is more favorable (Deming et al., 2009), and where the impacts of stellar magnetic activity are typically considered to be minimal. However, recent studies have shown that stellar flares (e.g., Davenport et al., 2019; Howard et al., 2023) and spots (e.g., Morris et al., 2018; Rackham & de Wit, 2023) contaminate transits, which impact transmission spectra and TTVs.

For example, infrared transit transmission observations of the TRAPPIST-1 system with JWST (e.g. Greene et al., 2023; Lim et al., 2023) show strong evidence of stellar contamination which dominates the planetary signal. Furthermore, there is poor stellar model fidelity causing high levels of uncertainty of up to an order of magnitude above observing precision. JWST has been able to observe T-1 and even though the primary focus has been to characterize the 7 rocky worlds, we are still able to gain useful insight into the stellar variability of the star.

(Howard et al., 2023) used NIRISS SOSS and NIRSpec BOTS JWST data (0.6-3.5μm) to study the IR flares of T-1 and found four flares. They found T-1 has flares large enough to impact transit observations (flare energy ¿ 10^{30} erg) occurring at a flare rate of 3.6 flares per day. They find effective flare temperatures of 5300 K. In the context of our work we find the Spitzer flares also have comparable temperatures to JWST at 5480 K. This is expected given their similarities in wavelength coverage. Furthermore, our analysis provides an independent validation of the infrared flare temperatures of T-1.

3.5.3 Future Directions

As more photometric and spectroscopic multi-wavelength data is collected of active stars we will be able to construct a better picture of the physics of stellar magnetic activity (e.g. flares) and the resulting impacts on exoplanet environments. These future observations will provide us with more accurate inputs into on our planetary atmosphere and retrieval models and thus help us infer the compositions of these exoplanets. Furthermore, as more IR data of active stars is collected with JWST and the upcoming Nancy Grace Roman Space Telescope (Spergel et al., 2015; Akeson et al., 2019) we will be able to study how stellar mass and age impacts flare properties.

Chapter 4

CHISPAS DE LUZ: STELLAR FLARE YIELDS WITH THE NANCY GRACE ROMAN SPACE TELESCOPE

Portions of this chapter were originally published in collaboration with Robert F. Wilson, Allison Youngblood, Laura D. Vega, Thomas Barclay, James R. A. Davenport, and Jordan Ealy (July 2023) to the Roman Core Community Survey White Paper call as well as to arXiv (arXiv:2307.05806 ; https://doi.org/10.48550/arXiv.2307.05806), and are reproduced below with the permission of the author.

4.1 Summary

The next NASA flagship mission is the Nancy Grace Roman Space Telescope (Roman), which is expected to launch in 2026. One of Roman's core community surveys, the Galactic Bulge Survey (GBTDS) will collect precise, time-series photometric data for over 100 million stars. Flares are a key observable for understanding stellar magnetic activity, and the GBTDS will be the first survey of its kind to focus on an older stellar population. Here we consider one season of Roman observations and assess the stellar flare yields for G, K, and M stars in the galactic bulge. To assess types of flares to which Roman will be sensitive, we run 10,000 simulations each for G, K, and M stars which include realistic noise properties and injected stellar flares. Furthermore, we compare two read-out strategies: a logarithmic case and one which preserves all read frames to study which maximizes the Roman flare science return. We are able to recover flares on 1% of G stars, 0.3 % of K stars, and 10% of M stars. We find Roman will be sensitive to super flares of energies greater than or equal to 10^{32} ergs.

4.2 Introduction

The Nancy Grace Roman Space Telescope (Roman) will expand our understanding of dark energy, exoplanets, and infrared astrophysics (Spergel et al., 2015; Akeson et al., 2019). With a field of view >100 times wider than Hubble, Roman will be able to image more of the sky in less time and at the same spatial resolution. Roman's Design Reference Mission (DRM) includes three core community surveys: the Galactic Bulge Time Domain Survey (GBTDS), the High Latitude Time Domain Survey (HLTDS), and the High Latitude Wide Area Survey (HLWAS). The primary instrument for Roman is the Wide Field Instrument (WFI), which will provide wide-field imaging and multi-object, slitless spectroscopy over a 0.281 deg^2 field-of-view. WFI has 8 different filters which cover 0.48 – 2.3 microns in wavelength space. One of the objectives of the GBTDS is to meet gravitational microlensing requirements by observing the dense Galactic bulge. For the 5-year primary mission survey, Roman will monitor microlensing events at a cadence of ∼15 minutes with the F146 wide-band filter (0.927-2 microns) for a period of at least 60 days, twice a year. While the Galactic bulge has a high density of stars, Roman's exquisite imaging (0.11" pixel^{-1}) and sensitivity (1% at F146=21 mag per 15 min cadence) will resolve over 56 million individual sources and precisely monitor their time variability. This survey is also expected to yield over 100,000 transiting exoplanet detections (Montet et al., 2017b).

Over the past decade, flare stars have been the subject of intensive research thanks to an abundance of wide-field, long-baseline, high-precision data from *Kepler* (Borucki et al., 2010) and *TESS* (Ricker et al., 2014). Stellar flares are caused by magnetic reconnection events in the outer atmospheres of stars, which can release accelerated charged particles and significant amounts of electromagnetic radiation ranging from gamma-ray to radio emission (Kowalski, 2024). Intense, frequent flares and associated particles or coronal mass ejections can heat the upper atmosphere of a planet, causing it to expand and potentially leading to atmospheric escape. It has been suggested (Cherenkov et al., 2017; Lammer et al., 2007; Segura et al., 2010) that frequent stellar flares, and energetic particles launched by the star,

can change the atmospheric composition or completely erode the atmosphere of an exoplanet over time. This loss can have a significant impact on the habitability of a planet, as it can affect the planet's ability to retain water and maintain a stable climate (Chen et al., 2021). On the other hand, these events can be the source of ultraviolet radiation needed for prebiotic chemistry to take place (Rimmer et al., 2018). Overall, the study of magnetic stellar activity is an essential aspect of exoplanet research, as it allows us to better understand the conditions that make a planet habitable and assess the potential for life beyond our solar system.

Roman takes the next step, achieving sensitivity and spatial resolution orders of magnitude better than *Kepler* and TESS, allowing us to measure stellar flares of a completely different stellar population for the first time. For instance, *Kepler* and TESS have only surveyed some of the closest and brightest stars ($<$ 17th mag) in our neighborhood (Hawley et al., 2014; Barclay & Barentsen, 2018; Günther et al., 2020). Meanwhile, bulge stars are generally older and more metal-poor than stars in the the solar neighborhood (Buck et al., 2018). With Roman we will be able to probe what happens to magnetic stellar activity beyond "field age" (5 Gyr) and at low metallicity.

Stellar flares are a manifestation of a star's dynamic surface magnetism, which is strongly dependent on stellar age (Davenport et al., 2019). Over a star's lifetime, the stellar wind causes the angular momentum loss, so the star spins down over time, which in turn, weakens the magnetic dynamo (Skumanich, 1972). Reduced flare rates with increasing stellar age have been seen in the solar neighborhood, but there are exceptions (old stars that are active; Proxima Centauri and Barnard's Star) (France et al., 2020), and there are relatively few stars in the solar neighborhood whose ages exceed 10 Gyr. What happens to the flare rates of such old stars is essentially unconstrained. Given the expected low flare rates of such an old population, a wide field, long time baseline survey like the GBTDS is ideal for probing these flare rates.

Another unique aspect of studying stellar flares with Roman is the wavelength regime. A high-precision, wide field time domain survey has never been conducted in the near infrared (NIR). For stellar flares, this will enable us to probe a different part of the flare spectral

energy distribution. This will directly provide information on stellar flare contamination of exoplanet transmission spectroscopy performed in the infrared with JWST (Davenport, 2017).

Here we present the first end-to-end simulations of flare recovery in one season of simulated Roman light curves for GKM dwarfs. We consider two possible read-out strategies or cadence modes for Roman, and quantify which schematic maximizes the Roman flare science return. In Section 4.3 we describe our methods. Section 4.4 highlights our flare yields and the optimal read-out schematic. We conclude with a discussion of our results and future applications of this work.

4.3 Methods

Stellar flares from foreground (disk) and bulge stars in Roman's GBTDS will provide important constraints on our understanding of stellar activity evolution, yet they will be an undesirable source of contamination for other studies. To prepare for and enhance the science return of Roman, we must consider how Roman's cadence, read-out strategy, and filter choices impact our ability to detect stellar flares. Here we simulate one season of Roman observations (66 days) for G, K, and M-type stars, using two different read-out strategies to study the sample of flares Roman will be able to detect.

4.3.1 Assumed Stellar Population

For this work we adopt the stellar population model from Wilson et al. (2023). This model is based off of the Besan con Galactic Model (BGM1612; Robin et al., 2003, 2012; Czekaj et al., 2014), but modifies the extinction model and the bulge population initial mass function to better match empirical results from the Hubble Space Telescope Terry et al. (2020). Based on the assumed galactic model, the GBTDS survey will monitor $\sim 24 \times 10^6$ G dwarfs, $\sim 31 \times 10^6$ K dwarfs, and $\sim 10^6$ M dwarfs with F146 $\leq$ 21 mag. The stars in the galactic bulge are older ($\geq$ 1 Gyr) than those found in the outer disk ($\leq$ 1 Gyr).

The primary stellar populations considered in this model are the thin disk, thick disk,

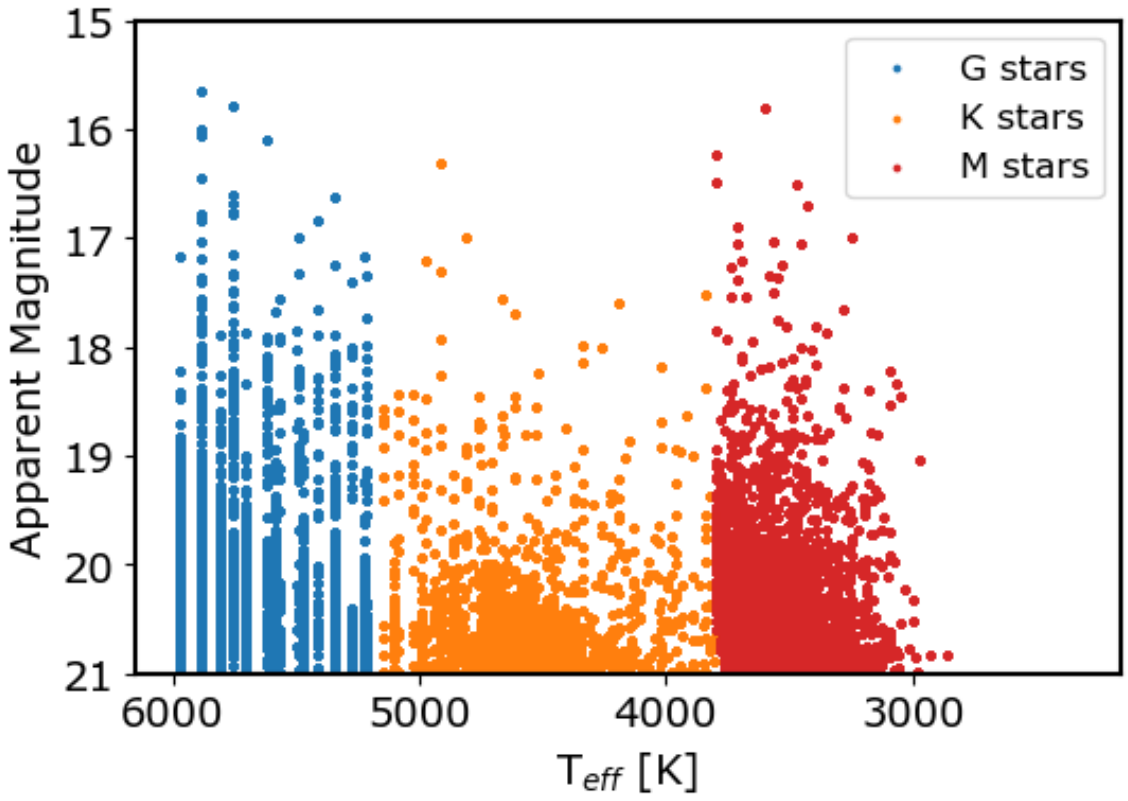

Figure 4.1 Apparent magnitude versus temperature of the simulated G (blue), K (orange), and M (red) stars in our sample.

and bulge. The thin disk is modeled as a set of mono-age populations ranging from ∼0.1 Gyr to ∼8 Gyr, with older populations (∼8 Gyr) dominating closer to the Galactic bulge, and younger populations (mean: ∼4 Gyr) dominating closer to the Solar neighborhood. The thick disk is modeled as a mono-age population of 8 Gyr with an exponential spatial distribution with scale height ∼1.5 kpc and radial scale length of ∼3 kpc. The bulge population is modeled as a mono-age population of 10 Gyr. Figure 4.1 shows the apparent magnitude versus temperature of the GKM stars we simulate for this work. The stars were pulled from isochrones models. The discrete temperature values we see are due to the different ages and metallicities assumed in the simulations.

4.3.2 Generating Synthetic Roman Light Curves

For these simulations, we assumed properties for the wide field instrument (WFI) and GBTDS mostly consistent with the simulation framework from Wilson et al. (2023). For the survey parameters, we assume an observing cadence of 15 minutes, an effective exposure time of approximately 54 seconds and a season duration of 66 days. All of the synthetic light curves in this work were generated in the $F146$ filter (0.927 μm - 2 μm).

To generate synthetic GBTDS light curves, we first generate a model light curve with injected flares and rotational modulation at a cadence of 1 second. The choice for the number of flares and flare parameters, as well as the rotational period and amplitude, are described in more detail in the sections below. To inject realistic noise into each light curve, we integrate the total flux of the source over the appropriate integration time. Unlike CCDs which integrate for a set amount of time and then destructively read out the collected charge, the H4RG-10 arrays used in the WFI read out non-destructively continuously during a single exposure at a rate of every 3.04 s, dictated by the speed of the detector electronics. We simulate this readout process for each exposure, in the process injecting stellar Poisson noise, thermal background flux (0.98 e^-/s/pixel), zodiacal background flux (4.25 e^-/s/pixel), and read noise ($\sigma_{\rm read}$ = 11 rms e^-/pixel/read). Our methodology for simulating more detailed detector read-out schematics is described in more detail in the subsections below.

Injecting Stellar Flares

To inject flares into the light curves, we assigned a designated flare frequency distribution (FFD) to each star based on its age and mass according to Davenport et al. (2019). We note that the flare yield we present is an upper limit since Roman will be probing an older ($\geq$ 1 Gyr) and redder stellar sample than the stars considered to derive the age based FFD in Davenport et al. (2019). We considered super flares with energy ranges between $10^{30} - 10^{40}$ erg. The low energy limit is defined by the minimum energy flare Roman is expected to detect for typical stars in our sample, which is limited by cadence and signal-to-noise. The high energy limit corresponds to the largest energy events recovered for GKM dwarfs in optical studies (e.g. Günther et al., 2020).

We use the the recently updated stellar flare profile from Tovar Mendoza (2022) (hereafter TM22), which is publicly available on GitHub[1] to draw the shapes of the flares. This stellar flare template describes the brightness time-series of a classical flare event: a fast rise and slow decay. The TM22 profile is an update to the Davenport et al. (2014) flare profile that was based on the Kepler-observed flares from the M dwarf GJ 1243. The TM22 relies on 3 scaling parameters: peak time, amplitude, and FWHM. We can also integrate the TM 22 flare model to calculate flare energies. This results in the following relationship: flare energy = 2.0487 x amplitude x FWHM. To estimate the flare amplitudes we drew from the Kepler flare properties presented in (Althukair & Tsiklauri, 2023). Since the amplitudes described in Althukair & Tsiklauri (2023) were in the Kepler bandpass we converted the values to the Roman bandpass assuming a 10,000K blackbody. With the flare energy and amplitude in hand, we derived the full width half maximum (FWHM) from the above equation. Once we had all of the flare properties we were able to inject realistic flares into the Roman light curves.

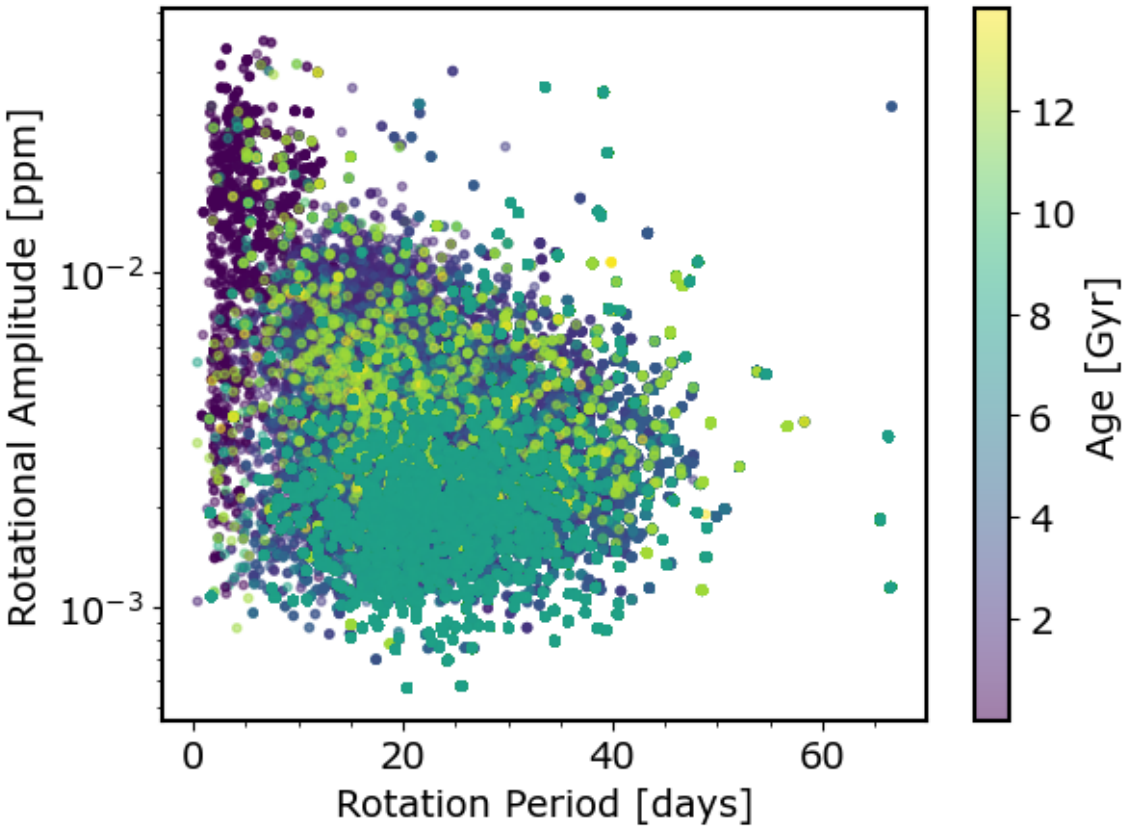

Figure 4.2 Rotation amplitude versus rotation period of the stars we simulated. The color bar shows the age distribution of stars.

Table 4.1. Flare Injection & Recovery Results

T_{eff} (Kelvin)	log(E) (erg)	t_{peak} (min)	Amp (relative)	FWHM (days)	Ramp	Expo
5821	30.20	4.43e+6	1e-6	186.928	0	0
4372	34.38	4.75e+6	.01	966.913	1	1
3585	33.63	1.97e+5	.02	1401.247	0	1

Note. — Summary table of all of the flares that were injected and recovered for each of the 10,000 simulated G, K, and M stars. A portion of the table is shown here for guidance regarding its form and content. This table is available in its entirety in machine-readable form in the online journal and on FigShare.

Injecting Rotational Modulation

Starspots on stellar surfaces moving in and out of view as the stars rotate cause a periodic modulation in their light curves. To account for these rotational modulations, we drew data from McQuillan et al. (2014) and Reinhold & Gizon (2015) which provide rotation periods for FGK stars in the original *Kepler* field-of-view. The catalog by Reinhold & Gizon (2015) contains more than 30,000 rotation periods, and photometric amplitudes, derived by using systematic automated searches from a well-defined sample of main-sequence stars observed by Kepler. The authors excluded about 2000 targets without T_{eff} or log(g) values, eclipsing binaries, and introduced a $T_{eff} < 6500$ K limit to reduce contamination of pulsating stars from the instability strip.

We combined both data sets by Kepler Input Catalog (KIC) number and only used the targets that had a rotation period, mass, and age values. Our final list contains 16,779

[1]https://github.com/lupitatovar/Llamaradas-Estelares

targets. We randomly drew rotation periods and amplitudes from the merged table with ages and masses within 10% of our randomly chosen star. To account for the differences between the Kepler and Roman bandpasses we reduced the amplitude signal by a factor of 0.45, which should be approximately consistent with temperature contrasts between the optical *Kepler* bandpass and the Near-IR H-band, similar to the Roman $F146$ bandpass (Gould et al., 2015). We then add a sinusoidal signal with the drawn period and amplitude to the synthetic light curve, with a randomly assigned phase. Figure 4.2 shows the rotational amplitude versus rotation period of the stars we simulated in this work. The color bar showcases the distribution of ages in our sample.

Injecting Noise and Simulating Ramp-Level Data

Because the WFI detectors can be read non-destructively, the nominal strategy for the GBTDS will be to "sample up the ramp" (SUTR; Fowler A.M, 1990; Casertano, 2022). This methodology has several benefits, including effective cosmic ray removal, reduced read noise, and improved dynamic range. SUTR records the accumulating voltage in each pixel of the H4RG-10 arrays at a rate of every 3.04 seconds (the read out time of the array), and the flux in each pixel is evaluated by fitting the slope of the increasing voltage. This final, evaluated flux we refer to hereafter as the "exposure-level" flux. Because each of the non-destructive reads (i.e., a "read frame") can be saved in principle, one can derive time-series photometry from each individual read at a cadence limited only by the read out time of the array. We refer to this flux hereafter as the "ramp-level" flux. In practice, however, the data generation rate that would result from preserving each read frame is higher than the data down link rate of the Roman spacecraft. Therefore, some sub-sample of the total number of read frames within an exposure must be either dropped or averaged together to lower the data volume and maintain uninterrupted observations. The resulting frames (referred to as "resultant frames" in the Roman literature) constructed by either preserving certain read frames or averaging 2+ read frames are then used to determine the exposure-level flux. The optimal read-out schematic for determining how resultant frames are generated from

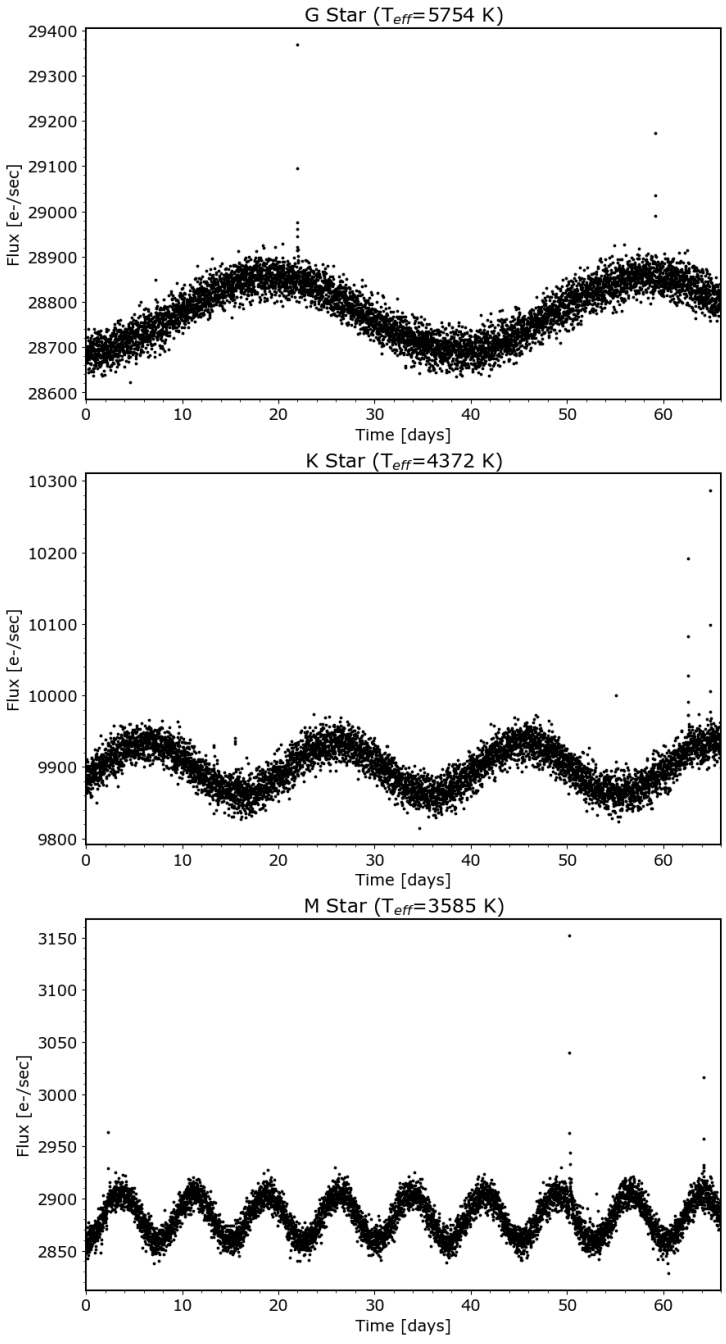

Figure 4.3 Simulated Roman light curves of a G, K, and M star with corresponding noise and crowding properties. The flares that are injected into each light curve were drawn from an age based flare frequency distribution (Davenport et al., 2019).

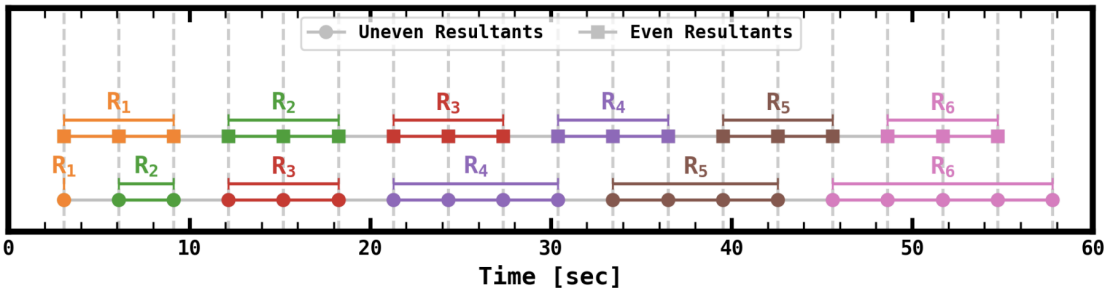

Figure 4.4 Candidate readout strategies introduced in Casertano (2022). Each individual point represents one read frame, and each color represents one resultant frame (e.g., R1, R2, etc.). Each resultant frame will consist of the average of one or more read frames.

the available read frames depends on the science case. The GBTDS is expected to employ a readout schematic wherein each exposure will result from 18-19 read frames and six resultant frames, resulting in an effective exposure time (i.e., the time between the first and last read frame) of 54-57 sec Casertano (2022). Figure 4.4 shows a schematic of the readout strategies.

To add noise to the synthetic model light curves, we simulate each individual read by integrating the model light curve over the readout time to determine the number of collected source photons in each read. Then, we draw the number of collected photons per read from a Poisson distribution with mean and variance equal to that of the expected number of photons from the source plus the thermal and zodiacal light background flux. For each read, the number of collected photons is accumulated from all previous reads. We assume that the flux is evaluated within a 3×3 pixel grid, resulting in background flux from nine total pixels, which should be a reasonable approximation for stars at the faint end of our simulations ($F146 < 21mag$) and inconsequential for stars on the bright end of our simulations ($F146 > 15mag$), which will be dominated by source photon noise. Finally, we add to each read a Gaussian read noise component. To account for saturation effects, the magnitude of the Poisson noise is artificially adjusted to be no smaller than that associated with a full well depth of 10^5 electrons, effectively creating a photometric noise floor of 0.3% per read frame. The inferred

signal from each of these reads is then used to generate resultant frames, according to the read-out schematic being applied.

Because many flares are known to occur with durations shorter than the GBTDS effective exposure time of 54-57 sec, we wish to evaluate the impact of exploiting the ramp-level flux in detecting short duration flares in the Roman data. Therefore, for each synthetic light curve we simulate every read frame, generate resultant frames, and from the resultant frames we produce two light curves per simulation: one exposure-level light curve and one ramp-level light curve. The ramp-level light curves are created by subtracting successive resultant frames from each other. The exposure-level light curves are generated by subtracting the accumulated signal inferred from the first resultant frame from the that inferred in the last resultant frame, resulting in an average flux across all 18-19 read frames. Note, that we are not directly performing a linear least squares fit to the resultant frames to derive the flux. This is because in the limit where the photometric error is dominated by correlated Poisson noise, the optimal scheme for weighting each of the resultant frames when performing the least-squares fit is equivalent to this treatment (Casertano, 2022).

To test the effect of read out strategy, we consider two different readout schematics (see Table 4.2). We consider one in which successive frames are averaged together (`AVG`; Casertano, 2022). While not feasible due to hardware limitations, we also consider a readout schematic in which all read frames are preserved (`ALL`). We test each schematic by applying our flare detection algorithm to the ramp-level light curves, as detailed below.

4.3.3 Flare Detection

To identify the flares in the light curves we first detrend the rotational modulations. We use the open source `wotan` (Hippke et al., 2019) light curve analysis package to remove the starspots from the time-series data. We specifically use the biweight filter with a window of 0.5 days, which effectively takes a sliding mean of the data, but with flux outliers (e.g., flares) penalized so as not to bias the interpretation of lower-frequency trends in the time-series with high-frequency signals.

Table 4.2. Readout Schematics Considered.

Name	N_{Frame}	N_{Res}	Sequence
`ALL`	19	19	1, 2, 3, ..., 18, 19
`AVG`	19	6	1, 2-3, 4-6, 7-10, 11-14, 15-19

Note. — Each row details the number of read frames per exposure (N_{Frame}), the number of resultant frames per exposure (N_{Res}), and which read frames are used to construct each resultant frame (Sequence).

We then use a simple algorithm to identify the flare events. For the full exposure level light curve, we run a sigma-clipping routine on the detrended light curve and identify all cadences that are 5 sigma above the mean. Next, we calculate the amplitude of all of the nearby flares that are within a peak time of 10 FWHM. The flare with the largest amplitude is cataloged as a detected flare. For the ramp-level light curve, each resultant pair is split into its own light curve given that the noise properties for pairs of resultants change significantly. The same flare detection procedure is then applied to each resultant light curve.

False Positive Flare Detections

Due to our flare simulation framework, and some of the simplifying assumptions in our flare injection code, we detect many false positives. To reduce the computational load we only calculate the shapes of flares within 100 times FWHM from the peak of the flare. This affects our detrending since the start and stop times of longer flares may be truncated. Furthermore, there are statistical fluctuations in our simulations.

To infer the false positive rate, we identify all detected flares with amplitudes $< 10^{-3}$, which is the noise floor of our simulations. Therefore, any flares with amplitudes lower than

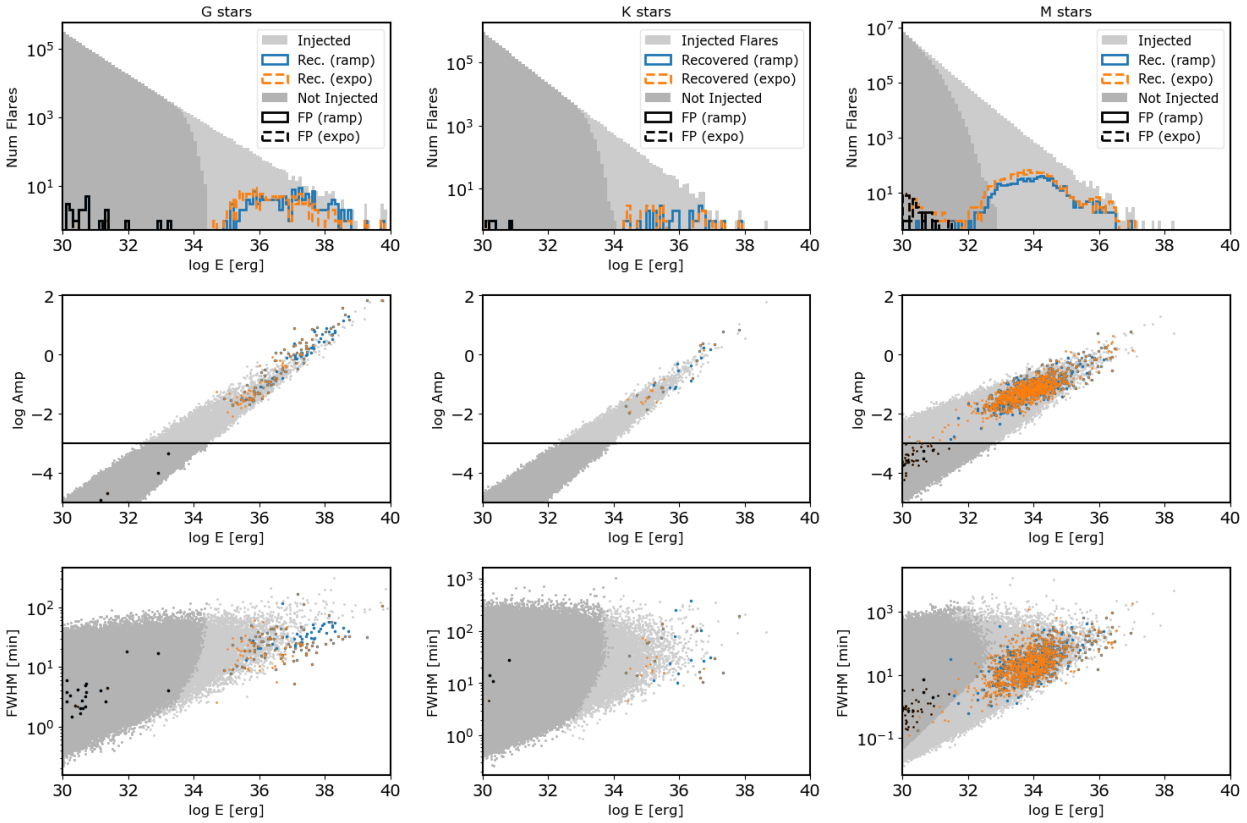

Figure 4.5 Flare yields for G, K, and M star simulations and corresponding flare properties for a logarithmic read out scenario. The first row shows histograms of the total injected flares by log flare energy [erg] for each stellar type. The second row shows the log amplitude of the flares versus log flare energy. The final row is the FWHM versus log flare energy. Across all panels the darker shaded regions are the false positives that were injected, the black dots are the recovered false positives. In orange are the flares recovered in the full exposure data, and in blue are the flares recovered in the ramp data.

this are lost in the noise, and thus not injected or recovered in our simulations.

4.4 Results

4.4.1 Flare Yields

We run a total of 10,000 simulations for each spectral type (GKM) then analyze the resulting light curves. We define the stellar bins by temperature: G stars $>$ 5200 K; 3800 $<$ K stars $<$ 5200, M stars $<$ 3800 K. First, we consider the logarithmic read-out schematic. For the G stars we are able to recover a total of 132 flares in the full exposure light curve and 150 flares in the ramp data. For the K stars we recover 33 flares in the full exposure data and 31 in the ramp data. Given their high activity levels and nearby proximity to the disk, the M stars yield the highest rates of flares: 1080 recovered in the full exposure data and 651 in the ramp data. Overall, using the logarithmic read-out we are able to recover flares on 1% of G stars, 0.3 % of K stars, and 10% of M stars. Table 4.1 shows the both the stellar and flare properties that were recovered in our simulations. The light curves are also made publicly available on Figshare.

We also consider the read-out schematic which preserves all read frames. In this scenario we are able to recover 128 flares in the full exposure data and 98 in the ramp data for the G stars. For the K stars we recover 38 flares in the full exposure light curve and 29 in the ramp data. We recover less flares around the K stars because the stars are less luminous and also fainter in the bulge (21st mag). Finally, for the M stars we recover 678 flares in the full exposure data and 132 in the ramp data. Using the read-out schematic where we preserve all frames we are able to recover flares on 1% of G stars, 0.3 % of K stars, and 6% of M stars.

Figures 4.5 and 4.6 show histograms of the total number of flares injected and recovered for each stellar type. We also highlight the relationships between flare energies, amplitudes, and FWHMs for all injected and recovered flares. We note that the flare yield is an upper limit. Since our stellar sample is older and redder than the sample considered to derive the age based FFD (Davenport et al., 2019).

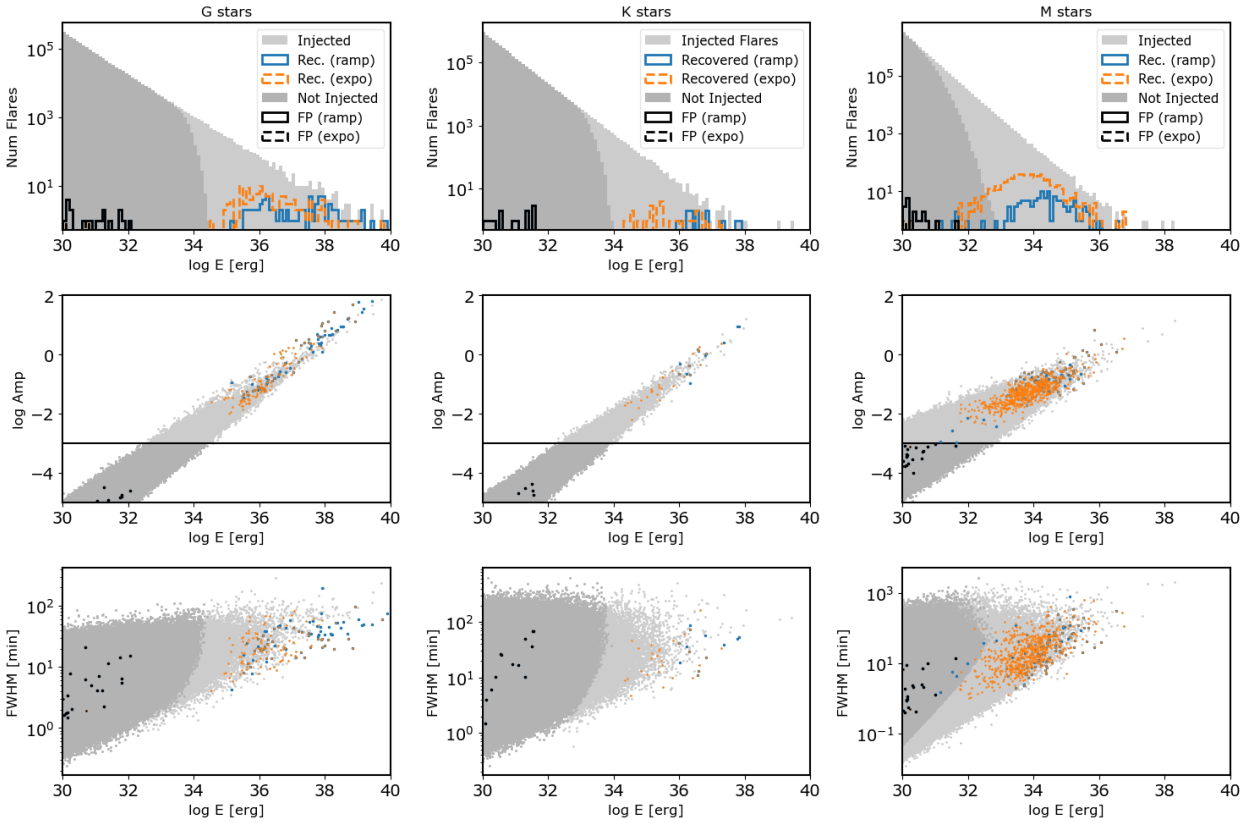

Figure 4.6 Flare yields for G, K, and M star simulations and corresponding flare properties for a read-out scenario where all read frames are preserved. The first row shows histograms of the total injected flares by log flare energy [erg] for each stellar type. The second row shows the log amplitude of the flares versus log flare energy. The final row is the FWHM versus log flare energy. Across all panels the darker shaded regions are the false positives that were injected, the black dots are the recovered false positives. In orange are the flares recovered in the full exposure data, and in blue are the flares recovered in the ramp data.

4.4.2 Optimal Read-Out Schematic

For both read-out cases we find that shorter duration flares (shorter FWHM) are more easily recovered in the ramp data. Whereas, longer duration flares (high FWHM) are more easily detectable in the full exposure data. It is also important to note that the single point uncertainty in the ramp data is larger than in the full exposure data, resulting in some flares going undetected because they fall within the noise limit of a given ramp exposure. In Figure 4.7, we see the stellar luminosities versus the log(flare energies) of our simulated stars. We highlight the flares that are recovered in both the full exposure and ramp data and show the comparison between the two read-out cases.

We find the read-out schematic that saves all of the read frames is most advantageous for short duration, high amplitude flares. When we preserve all of the read frames we end up with a shorter integration time, which yields higher noise per cadence. Although, this read-out schematic will not be feasible for Roman because it is too much data to store and then down link it is important to consider for future mission designs.

4.5 Discussion

Roman will be one of the first space-based missions to conduct a wide-field time domain survey of the galactic bulge at infrared wavelengths. Roman will be essential for exoplanet demographic studies (Wilson et al., 2023), which will also inform us about stellar demographics in the galactic bulge.

For stellar flares, this will enable us to study the flare rates of an old population of stars and also probe a different part of the flare spectral energy distribution (Maas et al., 2022). Flare effective temperatures are an active area of research (Howard et al., 2023) and the use of multiple filters would yield new information about the flare emission mechanisms at play (Osten et al., 2005; Paudel et al., 2021). Roman's wide filter F146 would enhance the overall signal-to-noise, however, the timescales of flares will be too short for Roman to observe a single flare in multiple filters. We expect bluer filters to have higher flare-star contrast

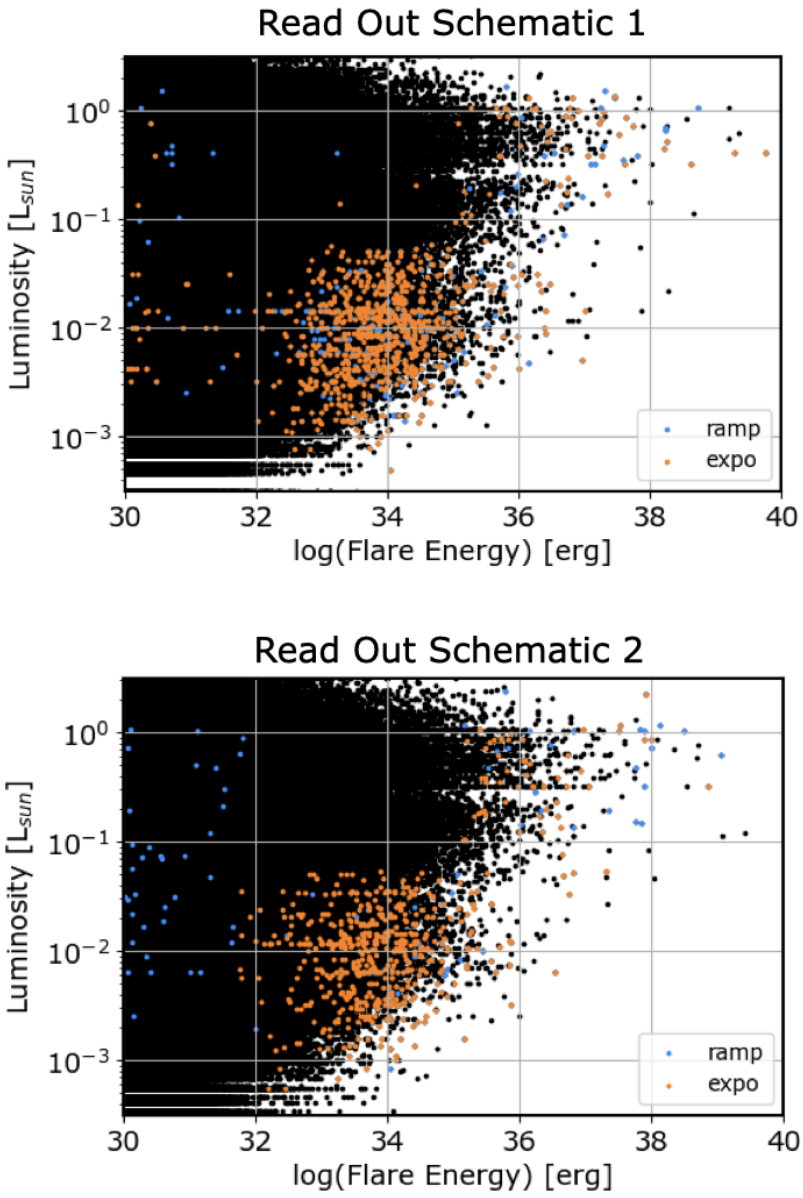

Figure 4.7 Simulated stellar luminosities [L_{Sun}] versus the log flare energies [erg] (black). The orange data are flares that were recovered in the full exposure light curve and in blue are the flares recovered in the ramp data. On the top are the results for the logarithmic read-out schematic and on the bottom are the results for the read-out schematic that preserves all the read frames.

ratios and improve the detectability of flares overall. However, redder filters are likely to improve our sensitivity with regard to lower-mass stars, reduce the effects of extinction, and probe deeper into the Galactic Bulge, exposing new and exciting stellar populations to flare demographics studies. This will directly provide information on stellar flare contamination, informing transiting exoplanet studies with JWST and future NASA missions (Davenport, 2017). Even though Roman likely could not capture individual flares with multiple filters, observing similar populations of stars in multiple filters would enable a population-level study of flare emission mechanisms (Brasseur et al., 2023; Jackman, 2022).

In this study we consider which types of flares Roman will be sensitive to and how the read-out schematic of choice impacts the science return. All of the light curves are made publicly available on FigShare along with the injected and recovered flare properties. We find Roman will be most sensitive to super flares with energies greater than 10^{30}erg. Many observed flares are complex (i.e., multi-peaked events) (Howard, 2022), particularly high energy events (Davenport et al., 2014). Complex flares can be modeled as a superposition of several classical flares Davenport et al. (2014); Tovar Mendoza (2022). Given Roman's planned 15-min cadence, many complex flares will be under-sampled and likely appear as classical flares, as seen in e.g. Kepler 30-min data (Maehara et al., 2015).

Results from the TESS mission have highlighted the importance of shorter cadence observations for flare studies. At higher time resolution, the measured flare energies are more accurate and finer structure of flare events is revealed ((Howard & MacGregor, 2021; Tovar Mendoza et al., 2022), such as the presence of multi-peak or complex flares. Even though Roman's cadence will not be able to resolve the most common, lower-energy events, it will be able to detect them. For the high-energy events with durations greater than 30 minutes (twice the observing cadence) Roman will be able to measure the flare energies. An advantage of the GBTDS observing strategy compared to previous high-cadence photometric surveys such as TESS and *Kepler*, is the shorter effective exposure time. Although the photometric precision is lower, high-frequency signals are not averaged out by the photon noise added in the longer exposure. As a result, short duration flares are detectable, even though

they are not resolvable. Although a single exposure is insufficient to derive a robust flare energy, the amplitude of the event will be sufficient for deriving a lower limit on the flare energy. A large sample of such lower limits when analyzed as a population will place strict constraints on higher energy flare frequencies. The fraction of detectable short duration flares can be approximated by the observing duty cycle, t_{exp}/cadence, which for the nominal GBTDS design is 6%. Thus, in the context of this proposed statistical study, the observing cadence directly correlates to the detection efficiency of short duration flares, and a shorter cadence is always better for flare science.

When we consider the Roman noise properties we are limited to stars brighter than 21st magnitude. We note that differential reddening is not taken into account in these simulations. However, Roman may be able to detect fainter stars in it's field-of-view if any of them have super flares (Osten et al., 2012). We also note our flare detection analysis does not make use of temporal sampling, which limits our recovery fractions. Future work should explore more novel ways to disentangle the flare signals and their temperatures in the infrared.

4.6 Acknowledgments

This research was supported by the National Aeronautics and Space Administration (NASA) under grant number 80NSSC23K0970 from the Astrophysics Data Analysis Program (ADAP). The material is based upon work supported by NASA under award number 80GSFC21M0002 from the CRESST II Cooperative Agreement. JRAD acknowledges support from the DiRAC Institute in the Department of Astronomy at the University of Washington. The DiRAC Institute is supported through generous gifts from the Charles and Lisa Simonyi Fund for Arts and Sciences, and the Washington Research Foundation. L.D.V. acknowledges the support from the Heising-Simons Astrophysics Postdoctoral Launch Program.

Chapter 5

CONCLUSIONS

In this last chapter, I give a summary of the key results found from the various projects described in each chapter of the thesis. I then give an overview of future work, remaining open questions, and the exciting stellar flare science that is yet to be uncovered with upcoming observatories.

5.1 Summary

In Chapter 2, I presented a flare template that can be used to model the morphology of white-light flares. Stellar flares share a common underlying formation mechanism; therefore a time-dependent profile can be derived to model the morphology of flares Davenport et al. (2014). To develop the continuous, analytical, and open-source flare template, I used Kepler stellar flare data from GJ 1243. I also used a Gaussian process regression model to account for the underlying starspots, and a Markov Chain Monte Carlo analysis to fit the model (Tovar Mendoza et al., 2022). This model improves upon previous studies by using an updated mathematical parameterization that ensures the model is continuous at the flare peak and more accurately represents the heating and two-phase cooling processes that occur during flare events (Jackman et al., 2018). The result is a continuous and analytic model that allows us to parameterize classical, single-peaked flare events and later decompose complex (multi-peak) flare events into a series of classical events as seen in Davenport et al. (2014). We demonstrated the utility of the model on the TESS data at various cadence modes and found the template could be used to accurately fit both classical (single-peak) and complex (multi-peak) flare events.

In Chapter 3, I used archival Spitzer data to understand the infrared flares of TRAPPIST-

1. I explored how infrared flare temperatures compare to optical measurements and the implications this has for the exoplanets in orbit around TRAPPIST-1. I concluded by comparing our results to the latest JWST observations of TRAPPIST-1.

In Chapter 4, I considered the capabilities that future missions such as the Nancy Grace Roman Space Telescope (Roman) will have on stellar flare science. Roman will probe millions of old stars in the galactic bulge in search for planets, many of which will be in orbit around active flare stars. I simulated Roman light curves with realistic noise properties and use a flare frequency distribution model to inject flares into the light curves. Then, we assessed the total expected flare yield across spectral type. We found that Roman will need to consider cadence, filters, and read-out strategies in order to maximize and expand our knowledge of stellar magnetic activity.

During my seven years of graduate school I was able to collaborate on many projects and generate any new ideas, not all of which were published. I conclude my thesis with the future directions of this work and a brief overview of the research ideas that did not make it to publication in the subsections below.

5.2 Future Work

We are in the era of both exoplanet and stellar characterization. In the coming years many surveys and observatories will be coming online and releasing new datasets that will allows us to deepen our understanding of exoplanets and their host stars.

5.2.1 Understanding Flare Energetics with Gaia

Since it's launch in 2013, Gaia has revolutionized our understanding of the stars in our Milky Way. By providing photometric and spectroscopic observations of millions of stars we have improved our knowledge on the positions, distances, movements, and changes in brightness of these celestial objects. More recently, the Gaia alerts pipeline has also been proving nightly alerts of any objects that are rapidly changing in brightness over time. The alerts provide simultaneous photometric and low resolution spectroscopic data. Among the

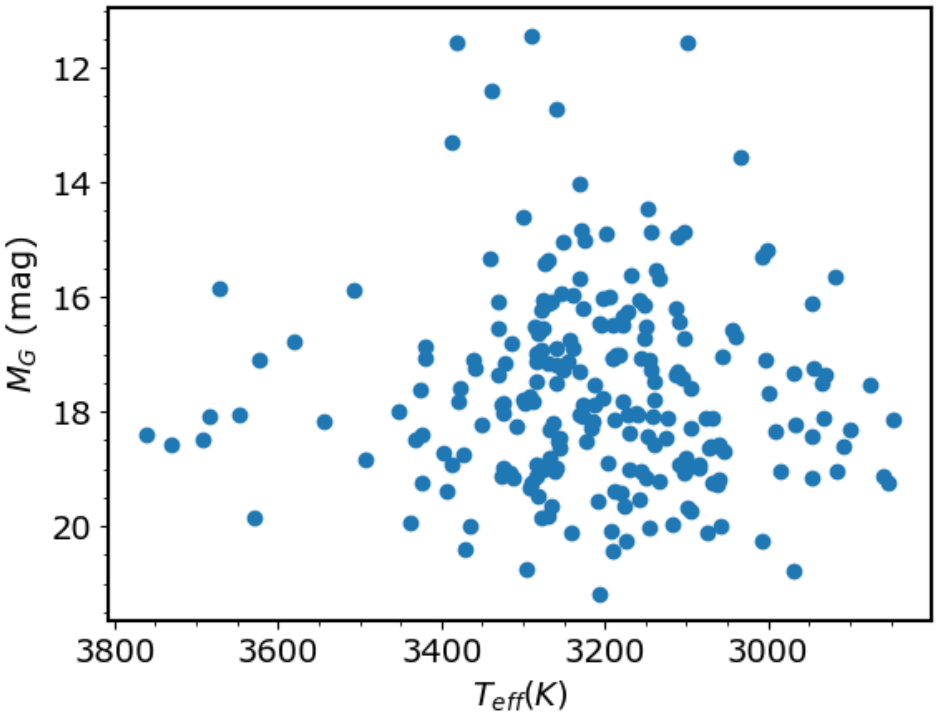

Figure 5.1 Apparent Gaia G-band magnitudes and effective temperatures for the 228 stars pulled from the Gaia alerts on April 2024 with following cuts: Temperature $\leq$ 3850; Radii $\leq$0.6 ; Magnitude (M_G) $\leq$ 17.

alerts we find supernovae, quasars, eclipsing binaries, variable stars, and of course stellar flares. Gaia Data Release 4 (DR4) is set to be publicly available no earlier than 2025. DR4 will provide multi-color photometry and mean spectra for millions of stars including all of the current Gaia alerts. Here we highlight the power of Gaia for stellar flare science and the bright future we have to look forward to with Gaia.

Flare energetics across stellar age, mass, and temperature remain largely unexplored. There have been efforts to investigate the impact of flares on planetary atmospheres (Segura et al., 2010; Tilley et al., 2019). However, future studies should be expanded to account for a variety of flare properties (e.g. temperatures, durations, energetics) and star-planet configurations (e.g. exoplanets around stars of different temperatures and masses). Vida

et al. (2017) analyzed the flares produced by TRAPPIST-1 using K2 data and found that both the high frequency of flares and flare energies are likely disadvantageous for life. In addition, Feinstein et al. (2020) showed that high flare rates increase the amount of photo-evaporative atmospheric mass loss for young planets. Specifically, when flares are present during the first 200 Myr, a planet can lose up to 4-7% more atmosphere than a model that does not take flares into account and that number increases the longer that flares persist. Furthermore, (Luger et al., 2015) showed that XUV emission of M dwarfs alone can remove several Earth masses of hydrogen and helium from mini-Neptune exoplanets. Their model did not consider the impacts of frequent flares and coronal mass ejections, which was stated could lead to erosion beyond what was modeled in their analysis. As we continue to collect more exoplanet observations it is critical to understand how the flare energetics of specific spectral types impact exoplanet environments.

The *Gaia* alerts provide multi-color photometry, which is useful for identifying stellar properties such as: temperature, age, and elemental composition (Vallenari et al., 2022). The blue photometer (BP) covers a wavelength range between 330–680 nm and the red photometer (RP) spans a wavelength range of 640–1050 nm. The multi-band observations will provide us with the data needed to study the temperatures of flares across spectral types. Furthermore, the Gaia alerts database also provides simultaneous low resolution spectroscopy (R$\sim$100) data. As of April 2024, we have identified 228 active flare stars within the Gaia alerts database that have simultaneous photometry and low-resolution spectra (see Figure 5.1). With Gaia we have the opportunity to answer the following questions 1) Do we see flare temperature evolution across different spectral types? and 2) How does this influence our modeling of exoplanet atmospheres?

Within the *Gaia* alerts, we only get a few data points for a given flare event[1] given Gaia's observing strategy. Figure 5.2 shows an example of a flare observed by *Gaia*. Even though we do not get photometric data for each epoch of the flare event we can still use the

[1] `http://gsaweb.ast.cam.ac.uk/alerts/alert/Gaia22bam/`

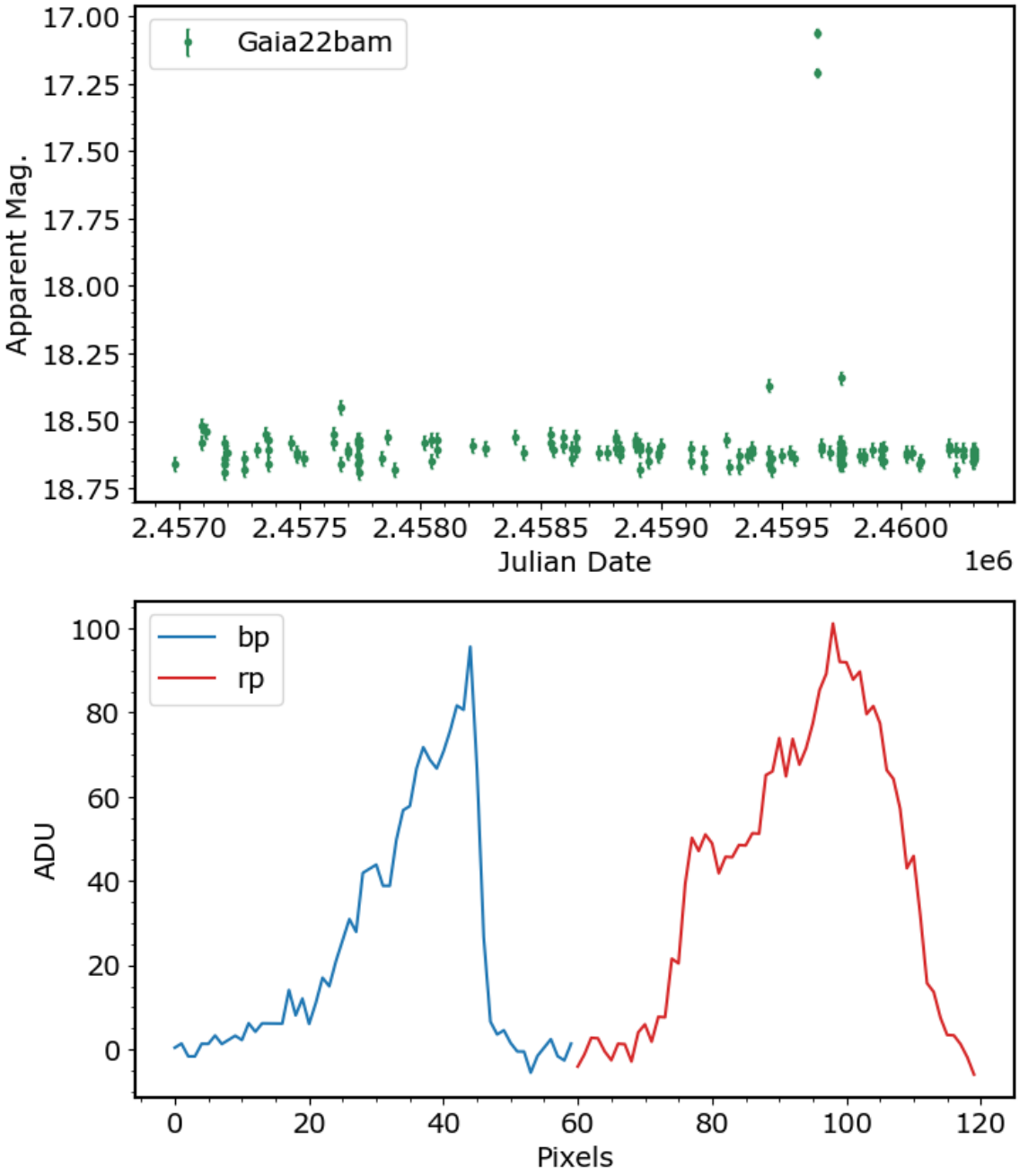

Figure 5.2 Top: Example Gaia alert of an active M star showing a 2 magnitude flare. Bottom: Simultaneous low resolution bp/rp spectra of the same target at the time of the flare event.

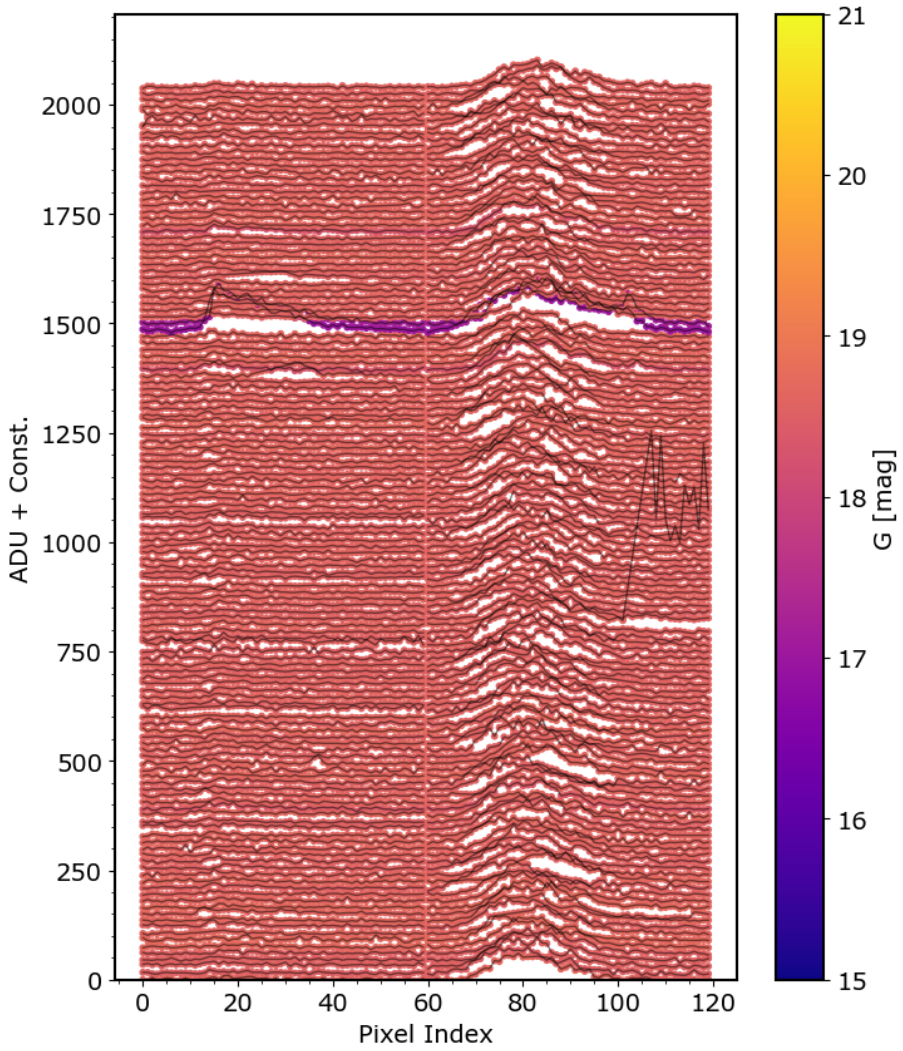

Figure 5.3 Raw epochal bp/rp spectra for 137 epochs for a flaring M5 dwarf that generated the Gaia alert Gaia22bam (TIC 354134293). Each epoch is colored by the published mean G magnitude. The blue channel is pixels 0–59, while the red channel is pixels 60–119. Note the pixel direction for the blue channel has been flipped relative to the observed Gaia data, so that it is in wavelength order. During the flare event (purple curve) we see an increase of two orders of magnitude in the blue channel, and a slight increase in the red channel, consistent with our expected behavior for a hot flare on this cool star.

multi-bandpass, low-resolution, spectra to say something about the color and temperature of the flares. Figure 5.3 shows the raw epochal spectra corresponding to the Gaia alert shown in Figure 5.2. During the flare event, we see an increase of two orders of magnitude in the blue filter because flares are hot, energetic, and thus blue events. Although the mean, higher resolution, spectra are still not available for these alerts we attempt to calibrate the data and extract temperature information (see subsection below).

Data Calibration

The Gaia Photometric Science Alerts (GPSA) are updated daily and the data is reported to the alerts website[2]. However, the spectra reported is only shown as a function of pseudo-wavelength (pixels) and ADU (counts) as seen in Figure 5.2. A conversion into wavelength and flux is required for each alert in order to perform a temperature analysis. To convert from pixels to wavelength space we used the rough conversion shown in (Carrasco et al., 2021), where pseudo-wavelength values 10 and 50 pixels approximately correspond to wavelengths 860 and 330 nm in the blue and 630 and 1090 nm in the red filter.

Next, we focused on converting ADU counts to flux values by generating data-driven response model function to perform the flux calibration. To do this we used an M4 stellar template (Davenport et al., 2012) to match the stellar type of the reported alert, and calibrated it to align with the Gaia filter range. Once we convolved the spectrum with the Gaia filter we were able to calculate the luminosity of the alert. From here, we divided the mean Gaia spectrum out of the M star template to estimate a source function. We show a proof of concept in Figure 5.4. Specifically, we show an example of the response function derived in the blue and red filters using stellar templates. We note the calibration can be significantly improved with higher resolution spectra that will be released in the coming years for all of the alerts. Furthermore, there is still ongoing work to calibrate the the spectra using other astrophysical phenomena such as supernovae (Barbary et al., 2022). Once the spectra are

[2] `http://gsaweb.ast.cam.ac.uk/alerts/`

properly calibrated in both the blue and red channels we will be able to fit a blackbody to the flaring epochs to determine temperatures for the flare events.

Future work will involve getting temperature distributions across stellar type. The temperature distribution of flares across spectral types will inform the next generation of exoplanet atmospheric modeling. Specifically, the optical flare temperatures of varying spectral types will be able to be used as updated inputs into atmospheric climate + photochemical models that seek to understand exoplanet environments with realistic effects from the host star.

Future work will also explore the synergies between *Gaia* and TESS. To date, TESS has observed many of the flare stars within the Gaia alerts. Figure 5.5 shows an example of an M star that was flagged by the Gaia alerts and a sector of 30 min TESS data. By combining the two datasets we can study the rotational modulations and also get constraints on the flare rates of the stars. Together, we will have a more complete picture of the activity cycles and energetics of these flare stars.

5.2.2 Probing Infrared Flares with JWST

The advent of the James Webb Space Telescope (JWST) represents a fundamental leap in our ability to probe and characterize the atmospheres of exoplanets using transmission spectroscopy. JWST is probing infrared (IR) wavelengths where the flux contrast between a planet and its star is more favorable (Deming et al., 2009), and where the impacts of stellar magnetic activity are typically considered to be minimal. However, recent observations of exoplanet atmospheres with JWST, the most advanced telescope launched to space to date, are contaminated with stellar activity features, making it difficult to disentangle planetary signals from stellar signatures. Specifically, stellar flares and spot modulations are producing signals up to an order of magnitude stronger than the planetary signals. Recent studies have shown that stellar flares (e.g., Davenport et al., 2019; Howard et al., 2023) and spots (e.g., Morris et al., 2018; Rackham & de Wit, 2023) contaminate transits, which impact transmission spectra and transit timing variations (TTVs).

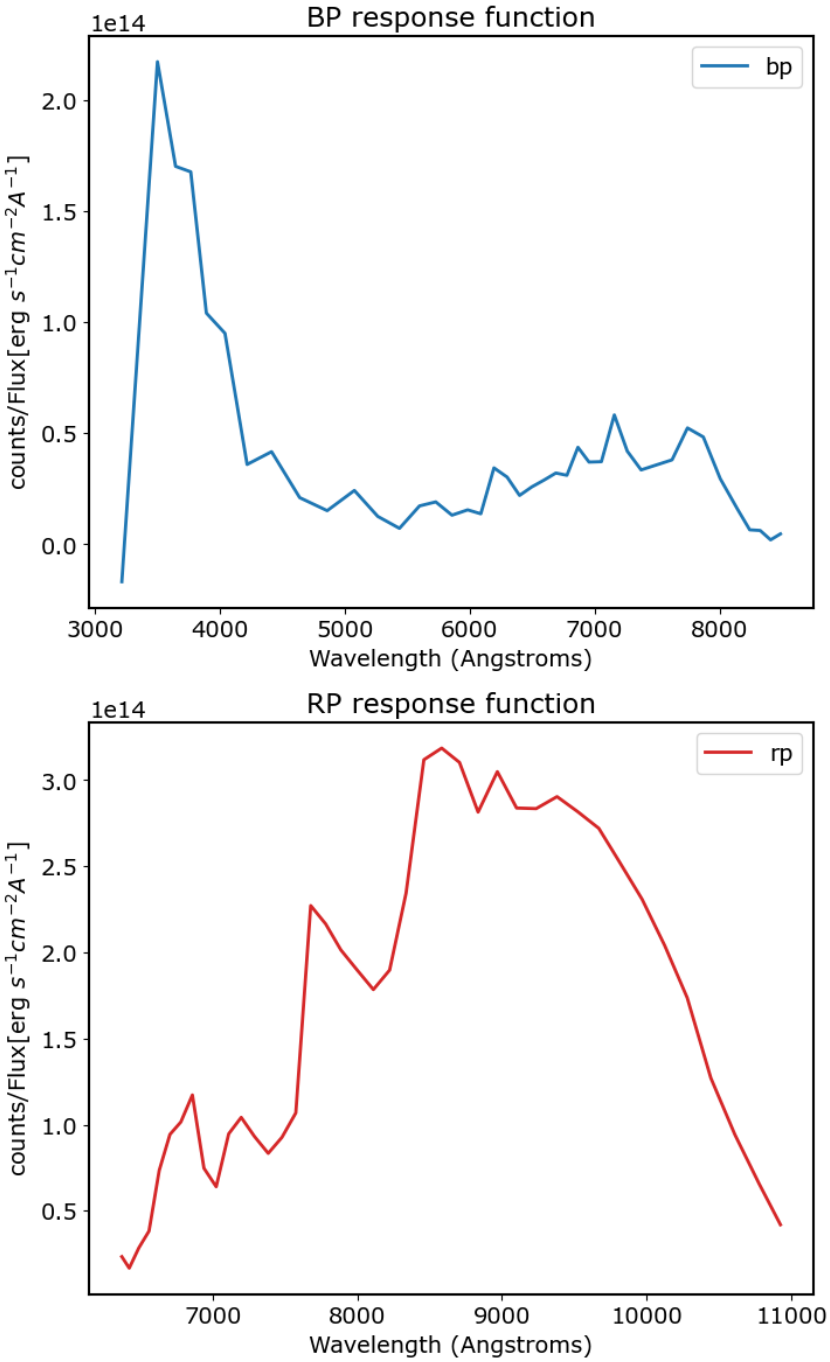

Figure 5.4 Example of a response function derived for the blue and red gaia filters for the flaring M5 star (gaia22bam). We note the response functions will be significantly improved when the higher-resolution mean *Gaia* spectra becomes available in a couple of years.

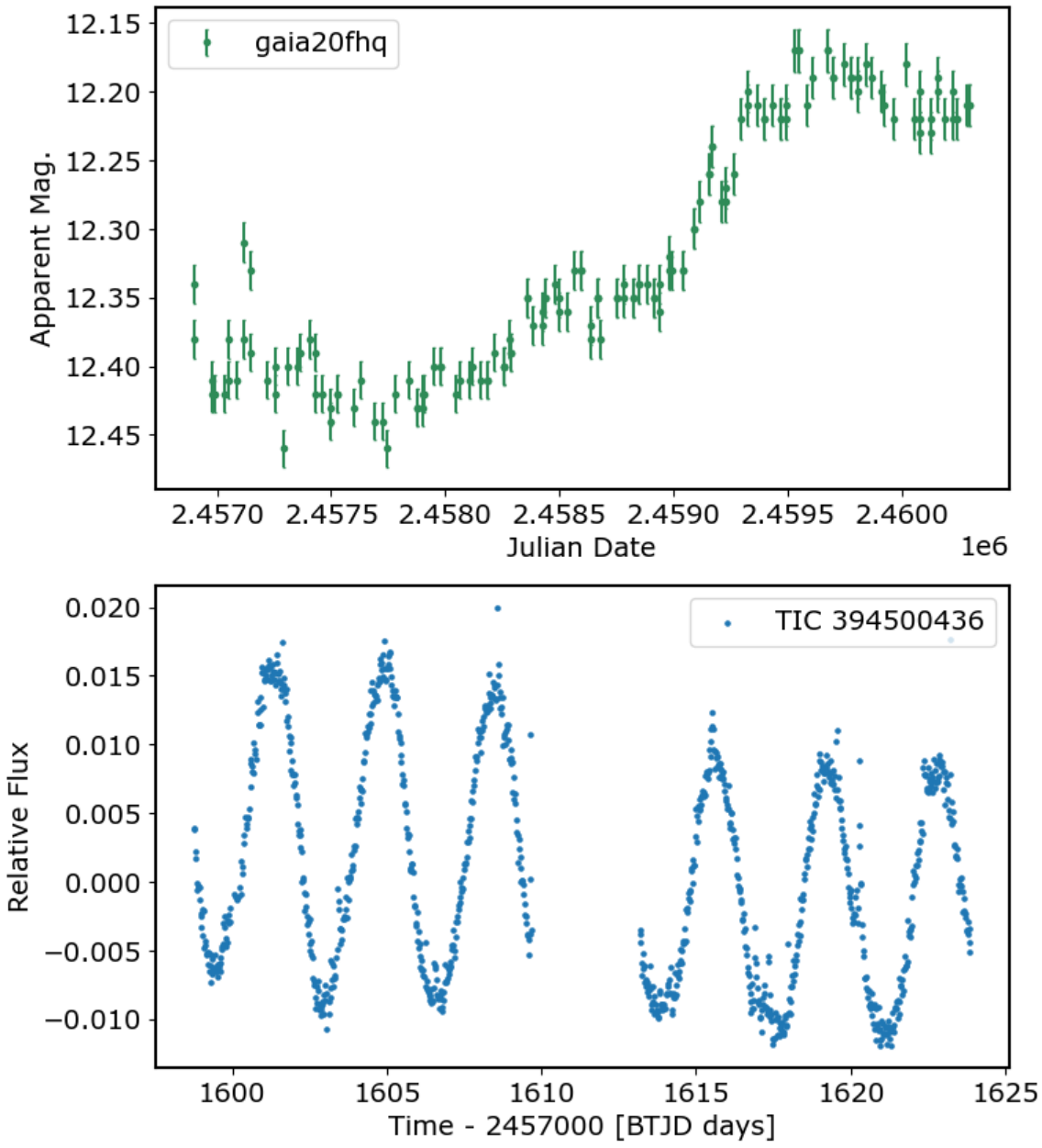

Figure 5.5 Top: G band light curve of a *Gaia* alert of an active M star. The long base line combined with the steady brightening is a sign of spot modulations. Bottom: Corresponding TESS 30 min data (sector 11) of the same target, confirming the rotational spot modulations.

Furthermore, early science results from JWST are showing that stellar contamination may be the limiting factor in the interpretation of the high-precision observations. For example, infrared transit transmission observations of the TRAPPIST-1 system with JWST (e.g. Greene et al., 2023; Lim et al., 2023) show strong evidence of stellar contamination which dominates the planetary signal. Furthermore, there is poor stellar model fidelity causing high levels of uncertainty of up to an order of magnitude above observing precision.

As a postdoc, I will lead a research program aimed to address the impacts of stellar activity on the measurements and interpretation of exoplanet atmospheres. First, I plan to develop a wavelength sensitive flare template to model the morphology of stellar flares in JWST infrared observations. I will build on my graduate research, which focused on using *Kepler* and TESS optical data to study the empirical morphology of stellar flares, and use JWST infrared data to develop a (publicly accessible) flare template and flares catalog that can be used to accurately model flares. I also plan to use a data-driven approach to generate stellar contamination models that include flares, spots, and faculae, and can be used by the wider scientific community to account for stellar signatures in transit transmission data. The results of this research program will help to identify and better understand the chemical composition of any existing exoplanet atmospheres.

5.2.3 Future Observatories

Past and current observatories have broadened our understanding of magnetically active stars. However, many open questions still remain such as: How does stellar magnetic activity influence the habitability of exoplanets over long timescales? How do flares impact exoplanet atmospheres? How do flare temperatures evolve over time and across spectral type? Upcoming observatories will allow us to conduct both individual monitoring of active stars and larger surveys (millions of stars) to help address these outstanding questions. In the subsections below, I highlight a few of the ground and space-based observatories that will be coming online in the next 1-5 years and the science they will enable for stellar magnetic activity.

Ground-Based Observatories

Ground based observatories have been critical for photometric and spectroscopic follow up observations of both stars and their planets. As we enter the era of large ground-based observatories our ability to monitor stellar variability will improve. Beginning operations in 2025, the Vera C. Rubin Observatory will conduct a 10-year survey of the Southern Hemisphere sky (Legacy Survey of Space and Time, or LSST). Using its 8.4 meter mirror, the Rubin Observatory is expected to provide over 10 billion light curves in six photometric filters: *ugrizy* (Ivezić et al., 2019). Stellar flares are stochastic, stellar transients that are likely to appear within LSST data. However, LSST is unlikely to detect flares with more than one data point in its main survey due to the short duration of these events. A recent study by (Clarke et al., 2024) shows that even with single-epoch detections we will be able to use Differential Chromatic Refraction to constrain flare temperatures.

The Extremely Large Telescope (ELT) is a project led by the European Space Observatory (ESO) agency and is currently under construction in Chile with first light expected in 2028. The 39 meter telescope is set to be the largest ground-based, optical, and near-infrared telescope. The ELT will provide observations that will impact all subfields of astrophysics. For instance, the ELT will allow us to characterize exoplanets and their stars with unprecedented detail from the ground (Padovani & Cirasuolo, 2023). The ELT is being designed to detect and characterize the atmospheres of Earth-sized planets. In addition, the ELT will be able to provide information about the chemical composition and ages of stars, which will provide us with a more complete picture of the relationships between exoplanets and their stars.

5.2.4 Space-Based Observatories

The second half of this decade will bring us three new space-based missions that will further our understanding of exoplanets and their host stars. The is the Nancy Grace Roman Space Telescope, which is set to launch in 2026. Roman will provide new insights into exoplanet

demographics and will probe the flare activity of some of the oldest stars in our galaxy (See Section 1.4.5 and Chapter 4 for more details). Also set to launch in 2026, is the European Space Agency (ESA) Planetary Transits and Oscillations of stars mission, Plato. With its 26 optical cameras, Plato aims to study rocky exoplanets around Sun-like stars. Plato will observe over 200,000 Sun-like stars over its mission lifetime and the team aims assemble a catalogue of confirmed and characterised planet and host star properties. Finally, in 2029 ESA will launch the Atmospheric Remote-sensing Infrared Exoplanet Large-survey (Ariel) mission. The primary goals of Ariel are to study what exoplanets are made of and how planetary systems form and evolve (Giovanna Tinetti et al., 2020). To do this, Ariel will study about a thousand exoplanets around a range of host stars which will reveal information about both planetary and stellar properties. Ariel will have photometric and spectroscopic capabilities at optical and infrared wavelengths (0.5 to 7.8 μm).

Small Satellites

Small satellites are a low cost and high reward opportunity especially for stellar flare science (Shkolnik, 2018). While flagship missions like JWST and the Nancy Grace Roman Space Telescope will provide great survey science of active flare stars (see Chapter 4), their observation time will also be shared with other astrophysics subfields. Thus, the overlap in mission timelines with flagship missions and small satellites is critical for follow up observations. Below I highlight four upcoming small satellites that will study exoplanets and their host stars.

Pandora is a small satellite mission selected for NASA's inaugural Astrophysics Pioneers program that will study approximately 20 stars and exoplanets in visible and infrared light with a primary goal of providing precise measurements of exoplanetary atmospheres. Pandora is set to launch in 2025. Pandora will provide the first dataset with simultaneous, multi-band, long-baseline observations of exoplanets and their host stars (Quintana et al., 2021). One of Pandora's main goals is to use its multi-wavelength observations to disentangle star and planet signals in transit spectroscopy to detect and robustly measure atmospheric

compositions. Pandora will observe a wide range of exoplanets around K and M-type stars and seeks to identify worlds with water or hydrogen-dominated atmospheres.

Twinkle is another small satellite set to launch in 2025 with a primary goal of studying exoplanets, bright stars, and solar system objects. Twinkle has a 0.45m primary mirror and will perform infrared (0.5-4.5 μm) spectroscopic observations. The mission lifetime is designed to be 7 years during which Twinkle will provide long term-observations of active stars. These observations will allow us to measure the variability of stars, help us place constraints on flare rates and determine the impact spots and faculae have on exoplanet transmission spectra (Stotesbury et al., 2022).

Mauve is an ultraviolet (200-700nm) satellite set to launch in 2025 with the goal of studying the stars in our galaxy [3]. Specifically, Mauve will provide spectroscopic observations of bright active stars which will enable us to study the flare evolution, chromospheric activity, and its impact on exoplanets. The satellite will have a 13cm primary mirror and will operate in a low-Earth orbit to maximize the observations along the ecliptic plane.

The Star-Planet Activity Research CubeSat (SPARCS) is set to launch in 2025 with a primary goal of monitoring the flares and star spot activity of low-mass stars (K and M spectral type) to assess how habitable the space environment is for planets orbiting them. Specifically, SPARCS will provide information about star's flare and quiescent emission, which powers photochemical reactions on the atmospheres of exoplanets. During the first year of its mission SPARCS will monitor 10 stars to measure short (minutes) and long (months) term variability. The observations will be simultaneous at near-ultraviolet (280 nm) and far-ultraviolet (162 nm) wavelengths (Ardila et al., 2018; Scowen et al., 2018).

In 2026, NASA and the Laboratory for Atmospheric and Space Physics will launch a CubeSat designed to be Monitoring Activity for Nearby sTars with uv Imaging and Spectroscopy (MANTIS) (Indahl & Wilson, 2022). MANTIS will investigate the impact of stellar UV emission on exoplanet atmospheres. Since solar observations from 2001, there have been

[3] `https://bssl.space/mauve/`

little to no observations of the full EUV spectrum from other stars. MANTIS will conduct observations at the extreme-ultraviolet (100–1200A; EUV), far-ultraviolet (1300–2200A; FUV), near-ultraviolet (2200–3500A; NUV), and visible (3500–10000A; VIS) wavelengths. MANTIS will be in operations at the same time as JWST and will help us characterize the high-energy stellar radiation that drives atmospheric photochemistry and escape of the worlds JWST is observing in the infrared.

To conclude, the future holds many exciting observatories that will be coming online to further our knowledge about the cosmos. As we continue to collect more observations we will be able to update our theories and models, leading us one step closer to understanding the relationship between stars and their planets.

BIBLIOGRAPHY

Agol, E., Cowan, N. B., Knutson, H. A., et al. 2010, Astrophysical Journal, 721, 1861, doi: 10.1088/0004-637X/721/2/1861

Agol, E., & Fabrycky, D. C. 2018, Handbook of Exoplanets, 797, doi: 10.1007/978-3-319-55333-7{_}7

Agol, E., Dorn, C., Grimm, S. L., et al. 2020, The Planetary Science Journal, 2, doi: 10.3847/PSJ/abd022

—. 2021, Planetary Science Journal, 2, 1, doi: 10.3847/PSJ/abd022

Agol Eric, Steffen J, Sari R, & Clarkson W. 2005, MNRAS, 359, 567

Airapetian, V. S., Glocer, A., Gronoff, G., Hébrard, E., & Danchi, W. 2016, Nature Geoscience, 9, 452, doi: 10.1038/ngeo2719

Akeson, R., Armus, L., Bachelet, E., et al. 2019, eprint arXiv:1902.05569, doi: 10.48550/arXiv.1902.05569

Althukair, A., & Tsiklauri, D. 2023, Research in Astronomy and Astrophysics, 0, doi: 10.1088/1674-4527/acdc09

Alvarado-Gómez, J. D., Cohen, O., Drake, J. J., et al. 2022, The Astrophysical Journal, 928, 147, doi: 10.3847/1538-4357/ac54b8

Andrews, A. D. 1965, Irish Astronomical Journal, 7, 20

Angus, R., Morton, T., Aigrain, S., Foreman-Mackey, D., & Rajpaul, V. 2018, Monthly Notices of the Royal Astronomical Society, 474, 2094, doi: 10.1093/mnras/stx2109

Ardila, D. R., Jewell, A., Nikzad, S., et al. 2018, arXiv e-prints, 1, doi: 10.48550/arXiv.1808.09954

Arney, G. N. 2020, arXiv, 873, L7, doi: 10.3847/2041-8213/ab0651

Aschwanden, M. J. 2002, Particle Acceleration and Kinematics in Solar Flares, 1, doi: 10.1007/978-94-017-2541-5{_}1

Aschwanden, M. J., Dennis, B. R., & Benz, A. O. 1998, THE ASTROPHYSICAL JOURNAL, 497, 972

Babcock, H. 1961, Astrophysical Journal, 133, 572, doi: 10.1086/147060

Ballard, S., & Johnson, J. A. 2016, The Astrophysical Journal, 816, 66, doi: 10.3847/0004-637X/816/2/66

Barbary, K., Bailey, S., Barentsen, G., et al. 2022, SNCosmo, Zenodo, doi: 10.5281/zenodo.7117347

Barclay, T., & Barentsen, G. 2018, Research Notes of the AAS, 2, 192, doi: 10.3847/2515-5172/aae9e2

Barclay, T., Endl, M., Huber, D., et al. 2015, The Astrophysical Journal, 800, 46, doi: 10.1088/0004-637X/800/1/46

Barclay, T., Sheppard, K. B., Latouf, N., et al. 2023, eprint arXiv:2301.10866. http://arxiv.org/abs/2301.10866

Barros, S. C. C., Demangeon, O., Díaz, R. F., et al. 2020, A&A, 634, 1, doi: https://doi.org/10.1051/0004-6361/201936086

Batalha, N. M., Rowe, J. F., Bryson, S. T., et al. 2013, Astrophysical Journal, Supplement Series, 204, doi: 10.1088/0067-0049/204/2/24

Bazilevskaya, G. 2017, Journal of Physics: Conference Series, 798, doi: 10.1088/1742-6596/755/1/011001

Benz, A. O. 2008, Living Rev. Solar Phys, 5, 1. http://www.livingreviews.org/lrsp-2008-1http://www.astro.phys.ethz.ch/staff/benz/benznf.html

Benz, A. O., & Güdel, M. 2010, Annual Review of Astronomy and Astrophysics, 48, 241, doi: 10.1146/annurev-astro-082708-101757

Berdyugina, S. V. 2005, Living Reviews in Solar Physics, 2, 1, doi: 10.12942/lrsp-2005-8

Berger, T. A., Schlieder, J. E., & Huber, D. 2023, eprint arXiv:2301.11338, doi: 10.48550/arXiv.2301.11338

Berger, T. E., Title, A. M., Tarbell, T. D., et al. 2007, New Solar Physics with Solar-B Mission ASP Conference Series, 369, 103

Borucki, W. J., Koch, D., Basri, G., et al. 2010, Science, 327, 977, doi: 10.1126/science.1185402

Brasseur, C. E., Osten, R. A., Tristan, I. I., & Kowalski, A. F. 2023, The Astrophysical Journal, 944, doi: 10.3847/1538-4357/acab59

Brun, A. S., & Browning, M. K. 2017, Living Reviews in Solar Physics, 14, 1, doi: 10.1007/s41116-017-0007-8

Buck, T., Ness, M. K., Macciò, A. V., Obreja, A., & Dutton, A. A. 2018, The Astrophysical Journal, 861, 88, doi: 10.3847/1538-4357/aac890

Burdanov, A. Y., Lederer, S. M., Gillon, M., et al. 2019, Monthly Notices of the Royal Astronomical Society, 487, 1634, doi: 10.1093/mnras/stz1375

Carrasco, J. M., Weiler, M., Jordi, C., et al. 2021, Astronomy and Astrophysics, 652, 1, doi: 10.1051/0004-6361/202141249

Carrington, R. 1859, Monthly Notices of the Royal Astronomical Society, 20, 13, doi: 10.1093/mnras/20.1.13

Casertano, S. 2022, Determining the best-fitting slope and its uncertainty for up-the-ramp sampled images with unevenly distributed resultants, Tech. rep., STScI

Chambers, K. C., Magnier, E. A., Metcalfe, N., et al. 2016, eprint arXiv:1612.05560, doi: 10.48550/arXiv.1612.05560

Charbonneau, P. 2014, Annual Review of Astronomy and Astrophysics, 52, 251, doi: 10.1146/annurev-astro-081913-040012

Chen, H., Zhan, Z., Youngblood, A., et al. 2021, Nature Astronomy, doi: 10.1038/s41550-020-01264-1

Chen, J., Liu, R., Liu, K., et al. 2020, The Astrophysical Journal, 890, doi: 10.3847/1538-4357/ab6def

Cherenkov, A., Bisikalo, D., Fossati, L., & Möstl, C. 2017, The Astrophysical Journal, 846, 31, doi: 10.3847/1538-4357/aa82b2

Clarke, R. W., Davenport, J. R. A., Gizis, J., et al. 2024, The Astrophysical Journal Supplement Series, 272, doi: 10.3847/1538-4365/ad4110

Collaboration, G., Brown, A. G. A., Vallenari, A., et al. 2018, Astronomy and Astrophysics, 1, 1

Cutri, R., Skrutski, M., van Dy, S., et al. 2003, 2MASS All Sky Catalog of point sources (NASA/IPAC Infrared Science Archive)

Cutri, R. M., & et al. 2012, VizieR Online Data Catalog: WISE All-Sky Data Release (Cutri+ 2012), VizieR On-line Data Catalog: II/311. Originally published in: 2012wise.rept....1C

Czekaj, M. A., Robin, A. C., Figueras, F., Luri, X., & Haywood, M. 2014, Astronomy and Astrophysics, 564, doi: 10.1051/0004-6361/201322139

Davenport, J. R., Becker, A. C., Kowalski, A. F., et al. 2012, Astrophysical Journal, 748, doi: 10.1088/0004-637X/748/1/58

Davenport, J. R. A. 2016, The Astrophysical Journal, 829, 23, doi: 10.3847/0004-637x/829/1/23

—. 2017, Research Notes of the AAS, 1, 2, doi: 10.3847/2515-5172/aa95c3

Davenport, J. R. A., Covey, K. R., Clarke, R. W., et al. 2019, The Astrophysical Journal, 871, 241, doi: 10.3847/1538-4357/aafb76

Davenport, J. R. A., Mendoza, G. T., & Hawley, S. L. 2020, The Astronomical Journal, 160, 36, doi: 10.3847/1538-3881/AB9536

Davenport, J. R. A., Hawley, S. L., Hebb, L., et al. 2014, The Astrophysical Journal, 797, 11, doi: 10.1088/0004-637X/797/2/122

Delrez, L., Gillon, M., Triaud, A. H. M. J., et al. 2018, Monthly Notices of the Royal Astronomical Society, 475, 3577, doi: 10.1093/mnras/sty051

Deming, D. 2005, Journal of the Royal Astronomical Society of Canada, 434, 740, doi: 10.1038/nature03473.1.

Deming, D., Seager, S., Winn, J., et al. 2009, Publications of the Astronomical Society of the Pacific, 121, 952, doi: 10.1086/605913

Donati, J. F., & Landstreet, J. D. 2009, Annual Review of Astronomy and Astrophysics, 47, 333, doi: 10.1146/annurev-astro-082708-101833

Doyle, J., van den Oord, G., Butler, C., & Kiang, T. 1990, Astronomy & Astrophysics, 232, 83

Dressing, C. D., & Charbonneau, D. 2013, The Astrophysical Journal, 767, 95, doi: 10.1088/0004-637X/767/1/95

Ducrot, E., Gillon, M., Delrez, L., et al. 2020, Astronomy and Astrophysics, 640, doi: 10.1051/0004-6361/201937392

Dumusque, X., Santos, N. C., Udry, S., Lovis, C., & Bonfils, X. 2011, A&A, 527, 82, doi: 10.1051/0004-6361/201015877

Durney B, Young D, R. I. 1993, Solar Physics, 145, 207

Eddy, J. 1974, A&A, 34, 235

Fazio, G. G., Hora, J. L., Allen, L. E., et al. 2004, The Astrophysical Journal Supplement Series, 154, 10, doi: 10.1086/422843

Feinstein, A. D., Montet, B. T., Ansdell, M., et al. 2020, The Astronomical Journal, 160, doi: 10.3847/1538-3881/abac0a

Feinstein, A. D., Seligman, D. Z., France, K., Gagné, J., & Kowalski, A. 2024, eprint arXiv:2405.00850. http://arxiv.org/abs/2405.00850

Filippazzo, J. C., Rice, E. L., Faherty, J., et al. 2015, Astrophysical Journal, 810, 158, doi: 10.1088/0004-637X/810/2/158

Foreman-Mackey, D. 2016, Journal of Open Source Software, 1, 24, doi: 10.21105/JOSS.00024

—. 2018, Research Notes of the AAS, 2, 1, doi: 10.3847/2515-5172/aaaf6c

Foreman-Mackey, D., Hogg, D. W., Lang, D., & Goodman, J. 2013, Publications of the Astronomical Society of the Pacific, 125, 306, doi: 10.1086/670067

Fowler A.M, G. I. 1990, Astrophysical Journal Letters, 353, L33

France, K., Duvvuri, G., Egan, H., et al. 2020, The Astronomical Journal, 160, doi: 10.3847/1538-3881/abb465

Galilei, G., Welser, M., & de Filiis, A. 1613, Istoria E dimostrazioni intorno alle macchie solari E loro accidenti comprese in tre lettere scritte all'illvstrissimo signor Marco Velseri ... (In Roma, Appresso Giacomo Mascardi, MDCXIII)

Gershberg, R. E. 1972, Astrophysics and Space Science, 19, 75, doi: 10.1007/BF00643168

Gilbert, E. A., Barclay, T., Kruse, E., Quintana, E. V., & Walkowicz, L. M. 2021, Frontiers in Astronomy and Space Sciences, 8, doi: 10.3389/fspas.2021.769371

Gilbert, E. A., Barclay, T., Quintana, E. V., et al. 2022, The Astronomical Journal, 163, 147, doi: 10.3847/1538-3881/ac23ca

Gillon, M., Triaud, A. H., Demory, B. O., et al. 2017a, Nature, 542, 456, doi: 10.1038/nature21360

Gillon, M., Triaud, A. H. M. J., Demory, B.-O., et al. 2017b, Nature, 542, doi: 10.1038/nature21360

Giovanna Tinetti, Carole Haswell, Jérémy Leconte, et al. 2020, arXiv e-prints

Gonzales, E. C., Faherty, J. K., Gagné, J., et al. 2019, The Astrophysical Journal, 886, 131, doi: 10.3847/1538-4357/ab48fc

Gopalswamy, N. 2016, Geoscience Letters, 3, doi: 10.1186/s40562-016-0039-2

Gordon, T. A., Agol, E., & Foreman-Mackey, D. 2020, The Astronomical Journal, 160, doi: 10.3847/1538-3881/abbc16

Gould, A. 2003, eprint arXiv:astro-ph/0310577, 1, doi: 10.48550/arXiv.astro-ph/0310577

Gould, A., Huber, D., Penny, M., et al. 2015, Journal of The Korean Astronomical Society, 48, 93, doi: 10.5303/JKAS.2015.48.2.93

Greene, T. P., Bell, T. J., Ducrot, E., et al. 2023, Nature, 618, 39, doi: 10.1038/s41586-023-05951-7

Grimm, S. L., Demory, B.-o., Gillon, M., et al. 2018, A&A, 613, doi: https://doi.org/10.1051/0004-6361/201732233

Gryciuk, M., Siarkowski, M., Sylwester, J., et al. 2017, Solar Physics, 292, doi: 10.1007/s11207-017-1101-8

Gully-Santiago, M. A., Herczeg, G. J., Czekala, I., et al. 2017, The Astrophysical Journal, 836, doi: 10.3847/1538-4357/836/2/200

Günther, M. N., & Daylan, T. 2021, The Astrophysical Journal Supplement Series, 254, 13, doi: 10.3847/1538-4365/abe70e

Günther, M. N., Zhan, Z., Seager, S., et al. 2020, The Astronomical Journal, 159, doi: 10.3847/1538-3881/ab5d3a

Harris, C. R., Millman, K. J., van der Walt, S. J., et al. 2020, Nature, 585, 357, doi: 10.1038/s41586-020-2649-2

Hathaway, D. H. 2015, Living Rev. Solar Phys, 12, 4, doi: 10.1007/lrsp-2015-4

Hawley, S. L., Davenport, J. R., Kowalski, A. F., et al. 2014, Astrophysical Journal, 797, doi: 10.1088/0004-637X/797/2/121

Haywood, R. D., Cameron, . C., Queloz, D., et al. 2014, MNRAS, 443, 2517, doi: 10.1093/mnras/stu1320

Henry, T., Jao, W., Subasavage, J., et al. 2006, The Astronomical Journal, 132, 2360, doi: 10.1086/508233

Hilton, E. J. 2011, PhD thesis, University of Washington, doi: 10.48550/arXiv.1012.0577

Hippke, M., David, T. J., Mulders, G. D., & Heller, R. 2019, The Astronomical Journal, 158, 143, doi: 10.3847/1538-3881/ab3984

Hodgkin, S. T., Harrison, D. L., Breedt, E., et al. 2021, Astronomy and Astrophysics, 652, 1, doi: 10.1051/0004-6361/202140735

Holman, M. J., Fabrycky, D. C., Ragozzine, D., et al. 2010, Science, 330, 51, doi: 10.1126/science.1195778

Howard, W. S. 2022, Monthly Notices of the Royal Astronomical Society: Letters, 512, L60, doi: 10.1093/mnrasl/slac024

Howard, W. S., & MacGregor, M. A. 2021, The Astrophysical Journal, 926, doi: 10.3847/1538-4357/ac426e

Howard, W. S., Corbett, H., Law, N. M., et al. 2020, arXiv, doi: 10.3847/1538-4357/abb5b4

Howard, W. S., Kowalski, A. F., Flagg, L., et al. 2023, The Astrophysical Journal, 959, 64, doi: 10.3847/1538-4357/acfe75

Howell, S. B., Sobeck, C., Haas, M., et al. 2014, Publications of the Astronomical Society of the Pacific, 126, 398, doi: 10.1086/676406

Hunt-Walker, N. M., Hilton, E. J., Kowalski, A. F., Hawley, S. L., & Matthews, J. M. 2012, Publications of the Astronomical Society of the Pacific, 124, 545, doi: 10.1086/666495

Hunter, J. D. 2007, Computing in Science and Engineering, 9, 90, doi: 10.1109/MCSE.2007.55

Ilin, E., Schmidt, S. J., Poppenhäger, K., et al. 2021a, A&A, 645, 25

Ilin, E., Poppenhaeger, K., Schmidt, S. J., et al. 2021b, Monthly Notices of the Royal Astronomical Society, 507, 1723, doi: 10.1093/MNRAS/STAB2159

Indahl, B., & Wilson, D. 2022, MANTIS: Monitoring Activity from Nearby sTars with uv Imaging and Spectroscopy, NASA Prop. ID 22-APRA22-121

Irwin, J., Berta, Z. K., Burke, C. J., et al. 2011, The Astrophysical Journal, 727, 56, doi: 10.1088/0004-637X/727/1/56

Ivezić, , Kahn, S. M., Tyson, J. A., et al. 2019, The Astrophysical Journal, 873, 111, doi: 10.3847/1538-4357/ab042c

Jackman, J. 2020, PhD thesis, University of Warwick. http://wrap.warwick.ac.uk/147858

Jackman, J. A., Wheatley, P. J., Pugh, C. E., et al. 2019, Monthly Notices of the Royal Astronomical Society, 482, 5553, doi: 10.1093/MNRAS/STY3036

Jackman, J. A. G. 2022, Monthly Notices of the Royal Astronomical Society, 517, 1, doi: 10.1093/mnras/stac2886

Jackman, J. A. G., Shkolnik, E., Million, C., et al. 2022, Monthly Notices of the Royal Astronomical Society, 21, 1

Jackman, J. A. G., Wheatley, P. J., Pugh, C. E., et al. 2018, Monthly Notices of the Royal Astronomical Society, 477, doi: 10.1093/mnras/sty897

Johnson, L. J., Norris, C. M., Unruh, Y. C., et al. 2021, MNRAS, 504, 1, doi: 10.1093/mnras/stab1190

Kaltenegger, L., & Traub, W. A. 2009, Astrophysical Journal, 698, 519, doi: 10.1088/0004-637X/698/1/519

Kempton, E. M., Bean, J. L., Louie, D. R., et al. 2018, Publications of the Astronomical Society of the Pacific, 130, doi: 10.1088/1538-3873/aadf6f

Kipping, D. M. 2012, Mon. Not. R. Astron. Soc, 427, 2487, doi: 10.1111/j.1365-2966.2012.22124.x

Kochukhov, O. 2021, The Astronomy and Astrophysics Review, 29, doi: 10.1007/s00159-020-00130-3

Kopparapu, R. K. 2013, Astrophysical Journal Letters, 767, 5, doi: 10.1088/2041-8205/767/1/L8

Kowalski, A. F. 2024, Living Reviews in Solar Physics, 21, doi: 10.1007/s41116-024-00039-4

Kowalski, A. F., Hawley, S. L., Holtzman, J. A., Wisniewski, J. P., & Hilton, E. J. 2010, The Astrophysical Journal Letters, 714, 98, doi: 10.1088/2041-8205/714/1/L98

Kowalski, A. F., Hawley, S. L., Wisniewski, J. P., et al. 2013, Astrophysical Journal, Supplement Series, 207, doi: 10.1088/0067-0049/207/1/15

Kowalski, A. F., Mathioudakis, M., Hawley, S. L., et al. 2016a, The Astrophysical Journal, 820, 000000, doi: 10.3847/0004-637X/820/2/95

—. 2016b, The Astrophysical Journal, 820, 95, doi: 10.3847/0004-637x/820/2/95

Lacy, C. H., Moffett, T. J., & Evans, D. S. 1976, The Astrophysical Journal Supplement Series, 30, 85

Lammer, H., Lichtenegger, H. I., Kulikov, Y. N., et al. 2007, Astrobiology, 7, 185, doi: 10.1089/ast.2006.0128

Lightkurve Collaboration, Cardoso, J. V. d. M., Hedges, C., et al. 2018, Lightkurve: Kepler and TESS time series analysis in Python

Lim, O., Benneke, B., Doyon, R., et al. 2023, The Astrophysical Journal Letters, 955, doi: 10.3847/2041-8213/acf7c4

Liu, K., Wang, Y., Zhang, J., et al. 2015, The Astrophysical Journal, 802, doi: 10.1088/0004-637X/802/1/35

Low, B. 1990, Annual Review of Astronomy and Astrophysics, 28, 491

Loyd, R. O. P., & France, K. 2014, The Astrophysical Journal Supplement Series, 211, 9, doi: 10.1088/0067-0049/211/1/9

Luger, R., Barnes, R., Lopez, E., et al. 2015, Astrobiology, 15, 57, doi: 10.1089/ast.2014.1215

Luger, R., Lustig-Yaeger, J., Fleming, D. P., et al. 2017a, The Astrophysical Journal, 837, 63, doi: 10.3847/1538-4357/aa6040

Luger, R., Sestovic, M., Kruse, E., et al. 2017b, Nature Astronomy, 1, doi: 10.1038/s41550-017-0129

Maas, A. J., Ilin, E., Oshagh, M., et al. 2022, A&A, 668, 1, doi: https://doi.org/10.1051/0004-6361/202243869

Macgregor, M. A., Weinberger, A. J., Loyd, R. O. P., et al. 2021, The Astrophysical Journal Letters, 911, L25, doi: 10.3847/2041-8213/abf14c

Maehara, H., Shibayama, T., Notsu, Y., et al. 2015, Earth, Planets and Space, 67, doi: 10.1186/s40623-015-0217-z

Maehara, H., Notsu, Y., Namekata, K., et al. 2021, Publications of the Astronomical Society of Japan, 73, 44, doi: 10.1093/pasj/psaa098

Mandt, K., Luspay-Kuti, A., Lustig-Yaeger, J., Felton, R., & Domagal-Goldman, S. 2022, The Astrophysical Journal, 930, 73, doi: 10.3847/1538-4357/ac59bb

Martens, P.C.H;Kuin, N. 1989, Solar Physics, 122, 263. http://link.springer.com/10.1007/978-3-319-59379-1%0Ahttp://dx.doi.org/10.1016/B978-0-12-420070-8.00002-7%0Ahttp://dx.doi.org/10.1016/j.ab.2015.03.024%0Ahttps://doi.org/10.1080/07352689.2018.1441103%0Ahttp://www.chile.bmw-motorrad.cl/sync/showroom/lam/es/

Martínez, R. R., Lopez, L. A., Shappee, B. J., et al. 2019, The Astrophysical Journal, 892, doi: 10.3847/1538-4357/ab793a

Mayor, Michel; Queloz, D. 1995, Nature, 378, 355

McCullough, P. R., Crouzet, N., Deming, D., & Madhusudhan, N. 2014, Astrophysical Journal, 791, doi: 10.1088/0004-637X/791/1/55

McQuillan, A., Mazeh, T., & Aigrain, S. 2014, Astrophysical Journal, Supplement Series, 211, doi: 10.1088/0067-0049/211/2/24

Moitinho, A., Krone-Martins, A., Savietto, H., et al. 2017, Astronomy and Astrophysics, 605, doi: 10.1051/0004-6361/201731059

Montegriffo, P., De Angel, F., Andrae, R., et al. 2022, Astronomy & Astrophysics, 1, doi: 10.1051/0004-6361/202243880

Montet, B., Tovar, G., & Foreman-Mackey, D. 2017a, Astrophysical Journal, 851, 15, doi: 10.3847/1538-4357/aa9e00

Montet, B. T., Yee, J. C., & Penny, M. T. 2017b, Publications of the Astronomical Society of the Pacific, 129, 1, doi: 10.1088/1538-3873/aa57fb

Moorhead, A. V., Ford, E. B., Morehead, R. C., et al. 2011, The Astrophysical Journal Supplement, 197, doi: 10.1088/0067-0049/197/1/1

Moran, S. E., Stevenson, K. B., Sing, D. K., et al. 2023, The Astrophysical Journal Letters, 948, L11, doi: 10.3847/2041-8213/accb9c

Morgan, William Wilson; Keenan, P. 1973, Annual Review of Astronomy and Astrophysics, 11, 29, doi: 10.1146/annurev.aa.11.090173.000333

Morris, B. M., Agol, E., Davenport, J. R. A., & Hawley, S. L. 2018, The Astrophysical Journal, 857, 39, doi: 10.3847/1538-4357/aab6a5

Namekata, K., Maehara, H., Notsu, Y., et al. 2019, The Astrophysical Journal, 871, 187, doi: 10.3847/1538-4357/aaf471

Namekata, K., Maehara, H., Honda, S., et al. 2022, Nature Astronomy, 6, 241, doi: 10.1038/s41550-021-01532-8

NASA Exoplanet Archive. 2016, Kepler Stellar Properties Table, doi: 10.26133/NEA6

Notsu, Y., Shibayama, T., Maehara, H., et al. 2013, Astrophysical Journal, 771, doi: 10.1088/0004-637X/771/2/127

Odert, P., Leitzinger, M., Hanslmeier, A., & Lammer, H. 2017, Monthly Notices of the Royal Astronomical Society, 472, 876, doi: 10.1093/MNRAS/STX1969

Okamoto, S., Notsu, Y., Maehara, H., et al. 2021, The Astrophysical Journal, 906, doi: 10.3847/1538-4357/abc8f5

Osten, R. A., & Brown, A. 1999, THE ASTROPHYSICAL JOURNAL, 515, 746, doi: 10.1086/307034

Osten, R. A., Hawley, S. L., Allred, J. C., Johns-Krull, C. M., & Roark, C. 2005, The Astrophysical Journal, 621, 398, doi: 10.1086/427275

Osten, R. A., Kowalski, A., Sahu, K., & Hawley, S. L. 2012, Astrophysical Journal, 754, doi: 10.1088/0004-637X/754/1/4

Osten, R. A., & Wolk, S. J. 2015, Astrophysical Journal, 809, 79, doi: 10.1088/0004-637X/809/1/79

Padovani, P., & Cirasuolo, M. 2023, Contemporary Physics, 64, 47, doi: 10.1080/00107514.2023.2266921

Panagi, P., & Andrews, A. 1995, Monthly Notices of the Royal Astronomical Society, 277, 423, doi: 10.1093/mnras/277.2.423

Papadogiannakis, S., Goobar, A., Amanullah, R., et al. 2019, MNRAS, 483, 5045, doi: 10.1093/mnras/sty3301

Parker, E. N. 1955, Astrophysical Journal, 122

Parnell, C. E., & Jupp, P. E. 2000, The Astrophysical Journal, 529, 554, doi: 10.1086/308271

Paudel, R. R., Barclay, T., Schlieder, J. E., et al. 2021, The Astrophysical Journal, 922, 31, doi: 10.3847/1538-4357/ac1946

Paudel, R. R., Barclay, T., Youngblood, A., et al. 2024, arXiv e-prints. http://arxiv.org/abs/2404.12310

Pazzani, V., & Rodono, M. 1981, Astronomy & Astrophysics, 77, 347

Pearce, G., & Harrison, R. 1990, Astronomy & Astrophysics, 513

Pérez, F., & Granger, B. E. 2007, Computing in Science and Engineering, 9, 21, doi: 10.1109/MCSE.2007.53

Pettersen, B. R. 1989, International Astronomical Union Colloquium, 104, 299, doi: 10.1017/S025292110003195X

Plavchan, P., Barclay, T., Gagné, J., et al. 2020, Nature, 582, 497, doi: 10.1038/s41586-020-2400-z

Prusti, T., De Bruijne, J. H., Brown, A. G., et al. 2016, Astronomy and Astrophysics, 595, doi: 10.1051/0004-6361/201629272

Pugh, C. E., Armstrong, D. J., Nakariakov, V. M., & Broomhall, A.-M. 2016, MNRAS, 459, 3659, doi: 10.1093/mnras/stw850

Pugh, C. E., Nakariakov, V. M., & Broomhall, A.-M. 2015, The Astrophysical Journal Letters, 813, L5, doi: 10.1088/2041-8205/813/1/L5

Quintana, E. V., Colón, K. D., Mosby, G., et al. 2021, arXiv e-prints. http://arxiv.org/abs/2108.06438

Rackham, B. V., Apai, D., & Giampapa, M. S. 2018, The Astrophysical Journal, 853, 122, doi: 10.3847/1538-4357/AAA08C

Rackham, B. V., & de Wit, J. 2023, eprint arXiv:2303.15418, doi: 10.48550/arXiv.2303.15418

Ranjan, S., Wordsworth, R., & Sasselov, D. D. 2017, The Astrophysical Journal, 843, 110, doi: 10.3847/1538-4357/aa773e

Rasmussen, C. E., & Williams, C. K. I. 2006, J. Mach. Learn. Res, 11. www.GaussianProcess.org/gpml

Reback, J., McKinney, W., jbrockmendel, et al. 2024, pandas-dev/pandas: Pandas 1.2.3, doi: 10.5281/ZENODO.4572994

Reid, I. N., Hawley, S. L., Gizis, J. E., et al. 1995, AJ, 110, 1838, doi: 10.1086/117655

Reiners, A., & Basri, G. 2007, The Astrophysical Journal, 656, 1121, doi: 10.1086/510304

Reinhold, T., Bell, K. J., Kuszlewicz, J., Hekker, S., & Shapiro, A. I. 2019a, Astronomy and Astrophysics, 621, 1, doi: 10.1051/0004-6361/201833754

Reinhold, T., & Gizon, L. 2015, Astronomy and Astrophysics, 583, 1, doi: 10.1051/0004-6361/201526216

Reinhold, T., Shapiro, A., Solanki, S., et al. 2019b, Science

Ricker, G. R., Winn, J. N., Vanderspek, R., et al. 2014, Space Telescopes and Instrumentation 2014: Optical, Infrared, and Millimeter Wave, 9143, 914320, doi: 10.1117/12.2063489

Rimmer, P. B., Xu, J., Thompson, S. J., et al. 2018, Science Advances, 4, doi: 10.1126/sciadv.aar3302

Robin, A. C., Marshall, D. J., Schultheis, M., & Reylé, C. 2012, Astronomy and Astrophysics, 538, 1, doi: 10.1051/0004-6361/201116512

Robin, A. C., Reylé, C., Derrière, S., & Picaud, S. 2003, Astronomy and Astrophysics, 409, 523, doi: 10.1051/0004-6361:20031117

Robitaille, T. P., Tollerud, E. J., Greenfield, P., et al. 2013, Astronomy & Astrophysics, 558, A33, doi: 10.1051/0004-6361/201322068

Roettenbacher, R. M., & Kane, S. R. 2017, The Astrophysical Journal, 851, 77, doi: 10.3847/1538-4357/aa991e

Savanov, I. S., & Dmitrienko, E. S. 2011, Astronomy Reports, 55, 890, doi: 10.1134/S1063772911100088

Schmidt, S. J., Shappee, B. J., van Saders, J. L., et al. 2019, The Astrophysical Journal, 876, 115, doi: 10.3847/1538-4357/ab148d

Schneider, A. C., Shkolnik, E. L., Allers, K. N., et al. 2019, arXiv, 157, 234, doi: 10.3847/1538-3881/ab1a26

Scoggins, M. T., Davenport, J. R. A., & Covey, K. R. 2019, Research Notes of the AAS, 3, 137, doi: 10.3847/2515-5172/AB45A0

Scowen, P. A., Shkolnik, E., Ardila, D., et al. 2018, Proceedings of the SPIE, 10699, 14, doi: 10.1117/12.2315543

Seager, S., & Sasselov, D. D. 2000, The Astrophysical Journal, 537, 916, doi: 10.1086/309088

Segura, A., Walkowicz, L. M., Meadows, V., Kasting, J., & Hawley, S. 2010, astrobiology, 10, doi: 10.1089/ast.2009.0376

Shibata, Kazunari;Yokoyama, T. 2002, astrophysical journal, 577, 422

Shibayama, T., Maehara, H., Notsu, S., et al. 2013, The Astrophysical Journal Supplement Series, 209, 5, doi: 10.1088/0067-0049/209/1/5

Shields, A. L., Ballard, S., & Johnson, J. A. 2016, The habitability of planets orbiting M-dwarf stars, doi: 10.1016/j.physrep.2016.10.003

Shkolnik, E. L. 2018, Nature Astronomy, 2, 374, doi: 10.1038/s41550-018-0438-8

Silverberg, S. M., Kowalski, A. F., Davenport, J. R. A., et al. 2016, The Astrophysical Journal, 829, doi: 10.3847/0004-637X/829/2/129

Sing, D. K., Pont, F., Aigrain, S., et al. 2011, Monthly Notices of the Royal Astronomical Society, 416, 1443, doi: 10.1111/j.1365-2966.2011.19142.x

Sing, D. K., Fortney, J. J., Nikolov, N., et al. 2016, Nature, 529, 59, doi: 10.1038/nature16068

Skumanich, A. 1972, Astrophysical Journal, 171, 565

Smith, J. C., Stumpe, M. C., Van Cleve, J. E., et al. 2012, Publications of the Astronomical Society of the Pacific, 124, doi: 10.1086/667697

Soderblom, D. R. 2010, Annual Review of Astronomy and Astrophysics, 48, 581, doi: 10.1146/annurev-astro-081309-130806

Solanki, S. K. 2003, Astronomy and Astrophysics Review, 11, 153, doi: 10.1007/s00159-003-0018-4

Spergel, D., Gehrels, N., Baltay, C., et al. 2015, eprint arXiv:1503.03757. http://arxiv.org/abs/1503.03757

Stotesbury, I., Edwards, B., Lavigne, J.-f., et al. 2022, Proceedings of the SPIE, 12180, 1, doi: 10.1117/12.2641373

Terry, S. K., Barry, R. K., Bennett, D. P., et al. 2020, The Astrophysical Journal, 889, 126, doi: 10.3847/1538-4357/ab629b

Tilley, M. A., Segura, A., Meadows, V., Hawley, S., & Davenport, J. 2019, Astrobiology, 19, 64, doi: 10.1089/ast.2017.1794

Tofflemire, B. M., Wisniewski, J. P., Kowalski, A. F., et al. 2012, The Astronomical Journal, 143, 12, doi: 10.1088/0004-6256/143/1/12

Tovar Mendoza, G. 2022, Llamaradas-Estelares, Zenodo, doi: 10.5281/zenodo.6519192

Tovar Mendoza, G., Davenport, J. R. A., Agol, E., Jackman, J. A. G., & Hawley, S. L. 2022, The Astronomical Journal, 164, 17, doi: 10.3847/1538-3881/ac6fe6

Vallenari, A., Brown, A., & Prusti, T. 2022, Astronomy & Astrophysics, 1, doi: 10.1051/0004-6361/202243940

Venot, O., Rocchetto, M., Carl, S., Hashim, A. R., & Decin, L. 2016, The Astrophysical Journal, 830, 77, doi: 10.3847/0004-637x/830/2/77

Veronig, A. M., Odert, P., Leitzinger, M., et al. 2021, Nature Astronomy, 5, 697, doi: 10.1038/s41550-021-01345-9

Vida, K., Kővári, Z., Pál, A., Oláh, K., & Kriskovics, L. 2017, The Astrophysical Journal, 841, doi: 10.3847/1538-4357/aa6f05

Vida, K., Kriskovics, L., Oláh, K., et al. 2016, Astronomy and Astrophysics, 590, doi: 10.1051/0004-6361/201527925

Virtanen, P., Gommers, R., Oliphant, T. E., et al. 2020, Nature Methods, 17, 261, doi: 10.1038/s41592-019-0686-2

Walkowicz, L. M., Basri, G., Batalha, N., et al. 2011a, Astronomical Journal, 141, doi: 10.1088/0004-6256/141/2/50

—. 2011b, Astronomical Journal, 141, doi: 10.1088/0004-6256/141/2/50

Webb, D. F., & Howard, T. A. 2012, Living Reviews in Solar Physics, 9, doi: 10.12942/lrsp-2012-3

Werner, M. W. 2005, Advances in Space Research, 36, 1048, doi: 10.1016/j.asr.2005.04.012

Wilson, D. J., Froning, C. S., Duvvuri, G. M., et al. 2021, The Astrophysical Journal, 911, 18, doi: 10.3847/1538-4357/abe771

Wilson, R. F., Barclay, T., Powell, B. P., et al. 2023, The Astrophysical Journal Supplement Series, 269, doi: 10.3847/1538-4365/acf3df

Wright, N. J., Drake, J. J., Mamajek, E. E., & Henry, G. W. 2011, Astrophysical Journal, 743, doi: 10.1088/0004-637X/743/1/48

Zieba, S., Kreidberg, L., Ducrot, E., et al. 2023, Nature, 620, 746, doi: 10.1038/s41586-023-06232-z

Software and Facilities Used:

Python, IPython (Pérez & Granger, 2007), NumPy (Harris et al., 2020), Matplotlib (Hunter, 2007), SciPy (Virtanen et al., 2020), Pandas (Reback et al., 2024), Astropy (Robitaille et al., 2013), Lightkurve (Lightkurve Collaboration et al., 2018), celerite (Foreman-Mackey, 2018), `EMCEE` (Foreman-Mackey et al., 2013), `stella` (Feinstein et al., 2020), Llamaradas Estelares (Tovar Mendoza, 2022) wotan (Hippke et al., 2019)

Appendix A

VITA

Guadalupe Tovar Mendoza was born in Toppenish, WA in 1995. She is the proud daughter of Blanca Tovar Mendoza and Jaime Tovar Díaz. She graduated from Southridge High School in 2013. She also completed her Associate's degree from Colombia Basin College in 2013. Guadalupe earned a Bachelor's of Science degree in Astronomy with a minor in Physics from the University of Washington (UW) in 2017. Then in 2019, she went on to earn her Master's of Science degree in Astronomy at the UW. She completed her dual-title PhD in Astronomy and Astrobiology in 2024. Guadalupe will be starting a National Science Foundation Mathematical and Physical Sciences Ascend (NSF MPS-Ascend) Postdoctoral Fellowship at Johns Hopkins University.